

Performance Characterisation of Metal Additives in Paraffin Wax Hybrid Rocket Fuel Grains

Chikhar S Maharaj

Submitted in fulfilment of the academic requirements for the degree of Master of Science in
Mechanical Engineering, College of Agriculture, Engineering and Science, University of KwaZulu-
Natal.

Durban, South Africa
August 2018

Supervisors: Ms. Kirsty Veale
Co-Supervisor: Mr. Jean-Francois Pitot de la Beaujardiere
Co-Supervisor: Dr. Clinton Bemont

Declaration 1: Plagiarism

I, Chikhar S Maharaj, declare that,

- i. The research reported in this dissertation/thesis, except where otherwise indicated, is my original work.
- ii. This dissertation/thesis has not been submitted for any degree or examination at any other university.
- iii. This dissertation/thesis does not contain other persons' data, pictures, graphs or other information, unless specifically acknowledged as being sourced from other persons.
- iv. This dissertation/thesis does not contain other persons' writing, unless specifically acknowledged as being sourced from other researchers. Where other written sources have been quoted, then:
 - a. Their words have been re-written but the general information attributed to them has been referenced;
 - b. Where their exact words have been used, their writing has been placed inside quotation marks, and referenced.
- v. Where I have reproduced a publication of which I am an author, co-author or editor, I have indicated in detail which part of the publication was actually written by myself alone and have fully referenced such publications.
- vi. This dissertation/thesis does not contain text, graphics or tables copied and pasted from the Internet, unless specifically acknowledged, and the source being detailed in the dissertation/thesis and in the References sections.

Signed:..... Date:.....

Mr Chikhar S Maharaj

Declaration 2: Publications

Maharaj C.S.*, Veale K.†, Pitot de la Beaujardiere J.P.†, Bemont CP.†, “Design of a 75 mm Hybrid Rocket Motor to Test Metal Additives”, 52nd AIAA/ASME/SAE/ASEE Joint Propulsion Conference and Exhibit, Salt Lake City, Utah, July 2016.

*Primary author

†Co-author

Signed:..... Date:.....

Mr Chikhar S Maharaj

As the candidate’s supervisor I agree/do not agree to the submission of this thesis.

Signed:..... Date:.....

Ms. K Veale

As the candidate’s co-supervisor I agree/do not agree to the submission of this thesis.

Signed:..... Date:.....

Mr. Jean-Francois Pitot de la Beaujardiere

As the candidate’s co-supervisor I agree/do not agree to the submission of this thesis.

Signed:..... Date:.....

Dr. Clinton Bemont

Acknowledgements

My sincere thanks and appreciation to the following parties:

- My supervisors, Ms Kirsty Veale, Mr Jean Pitot and Dr Clinton Bemont for their guidance and support throughout this project.
- The mechanical engineering staff and students for their tolerance of the noise created during hot fire testing.
- Mr Jean Pitot for making the igniters and assisting with small scale igniter testing.
- Mr Timothy Velthuysen, Mr Udil Balmogim and Ms Raisa Theba, for their assistance with the assembly of the propellant feed lines as well as preparations for cold flow and hot fire testing.
- Students at the Aerospace Systems Research Group (ASReG) for acting as safety marshals during hot fire testing.
- The workshop staff at UKZN Mechanical Engineering for their assistance during the entire project.
- The Council for Scientific and Industrial Research (CSIR) and the Department of Science and Technology (DST) for providing personal financial support for the duration of the degree.
- The National Research Foundation (NRF) Thuthuka grant for funding this endeavour.

Finally, a thank you to my parents, Mr. Jay Maharaj and Mrs. Niri Maharaj for their support, patience and understanding for the duration of this degree.

Abstract

The Aerospace Systems Research Group (ASReG) at the University of KwaZulu Natal is actively developing sounding rockets in the Phoenix Hybrid Sounding Rocket Programme, for use by the South African scientific community. These sub-orbital launch vehicles use nitrous oxide and paraffin wax as propellants.

While paraffin wax offers large performance gains over typical polymeric fuels, due to its high regression rate, further performance gains can be achieved via the use of metal additives such as aluminium powder. The main advantage of using additives such as aluminium is the ability to create a smaller, more compact launch vehicle. This is due to a decrease in the optimal oxidiser-to-fuel ratio brought about by metallisation, which increases overall propellant density. Theoretically, an added advantage is the higher heat of combustion as a result of aluminium combustion. This added heat further increases the regression rate of the solid fuel grain. In order to realise these performance gains, various challenges need to be overcome. Some of these include delayed combustion due to the alumina layer that naturally coats the aluminium particles, slag formation and nozzle erosion.

In this study, a laboratory scale hybrid rocket motor was developed to test aluminised paraffin wax fuel grains via a series of hot fire tests. A nitrous oxide feed system was developed, as well as a computer program and associated electronics to control the system remotely and capture data from an array of sensor equipment.

Due to time constraints placed on the project, only pure paraffin wax and fuel grains comprising 40 % aluminium by mass were tested. Using specific impulse and characteristic velocity as performance metrics, preliminary data shows little to no gain in performance with aluminised fuel grains due to incomplete combustion of the aluminium. Substantial erosion of the copper nozzles that were used in the aluminium grain tests, due to localised melting, was also noted. Large amounts of aluminium and alumina slag was also found on the nozzles converging face.

In order to seek maximum performance gains from aluminium as an additive, it was recommended that the particle size be reduced and stripped of its oxide layer before addition into the solid fuel grain. This will ensure more complete and rapid combustion of the particles before being ejected from the combustion chamber.

Table of Contents

Declaration 1: Plagiarism.....	i
Declaration 2: Publications	ii
Acknowledgements	iii
Abstract.....	iv
Table of Contents.....	v
List of Figures	viii
List of Tables	xiii
Nomenclature.....	xv
1. Literature review	1
1.1. Introduction – fundamentals of hybrid rocket propulsion.....	1
1.2. Development of paraffin wax-based propellant.....	2
1.3. Regression rate theory.....	3
1.4. Regression of polymeric fuels.....	4
1.5. Regression of paraffin wax-based fuels	5
1.6. Energetic additives.....	6
1.6.1. Aluminium (Al).....	7
1.6.2. Magnesium (Mg).....	11
1.6.3. LiAlH_4 (Lithium aluminium hydride).....	12
1.7. Mixed flow theory.....	14
1.8. Stability theory.....	15
1.9. Injector design and theory.....	20
1.10. Summary of literature review	22
2. Combustion chamber assembly	24
2.1. Fore end modification	25
2.2. Nozzle	27
2.3. Fuel grain cartridge	27
2.4. Thermal liner.....	28

2.5.	Fuel grain casting.....	30
3.	Oxidiser feed system.....	35
3.1.	Pipe sizing.....	36
3.2.	Oxidiser flow control valve	37
3.3.	Supercharge system	42
3.4.	Purge system.....	43
3.5.	Propellant dump system.....	45
3.6.	Safety implementations.....	46
4.	Control and data acquisition system	48
4.1.	National Instruments cDAQ.....	48
4.1.1.	Relay outputs (NI 9474).....	49
4.1.2.	Pressure measurements (NI 9203)	50
4.1.3.	Thermocouple measurements (NI 9211).....	51
4.1.4.	Load cell measurements (NI 9237).....	51
4.2.	Arduino platform	53
4.3.	Termination system.....	54
4.4.	LabVIEW development	55
4.4.1.	Control structure	56
4.4.2.	Graphical code	58
4.4.3.	Graphical user interface (GUI).....	65
5.	Theoretical motor performance.....	69
6.	Igniter development	72
6.1.	Steel wool – Iron combustion	72
6.2.	Match heads – Phosphorus trisulphide, potassium chlorate.....	75
6.3.	Pyrotechnic made igniter- Sucrose, potassium nitrate	77
7.	Cold flow testing.....	78
7.1.	Injection line losses.....	78
7.2.	Injector characterisation.....	81
8.	Hot fire testing	83

8.1.	LH-001, pure paraffin wax fuel grain	84
8.2.	LH-003, pure paraffin wax fuel grain	89
8.3.	LH-007, pure paraffin wax fuel grain	92
8.4.	LH-005, 40% aluminised fuel grain.....	96
8.5.	LH-006, 40% aluminised fuel grain.....	101
8.6.	LH-008, 40% aluminised fuel grain.....	106
8.7.	Summary of hot fire testing	111
8.8.	Discussion of hot fire testing	112
9.	Conclusion	118
9.1.	Future recommendations.....	120
	References.....	121
	Appendix A: Manufacturing drawings	124
	Appendix B: NASA CEA input script	133
	Appendix C: Termination system C code	134
	Appendix D: Hot fire testing videos	136

List of Figures

Chapter 1

Figure 1.1: Hybrid Rocket Motor (Cantwell, 2014)	1
Figure 1.2: Boundary Layer Combustion (Cantwell, 2014)	2
Figure 1.3: Regression of Classical Fuels (Boronowsky, 2011)	5
Figure 1.4: Paraffin wax regression (Space Propulsion Group, no date)	5
Figure 1.5: c^* of aluminised paraffin vs. O/F ratio from the CEA code (McCormick <i>et al.</i> , 2005).....	8
Figure 1.6: Density of aluminium particles after oxidation at varying temperatures (Rai <i>et al.</i> , 2006).	9
Figure 1.7 O/F vs Isp for LiAlH_4 (Larson <i>et al.</i> , 2015).....	12
Figure 1.8: Frequency vs Normalised pressure - static testing (De Zilwa <i>et al.</i> , 2003).....	16
Figure 1.9: Exhaust plume oscillation (De Zilwa <i>et al.</i> , 2003)	17
Figure 1.10: Pressure-Time history for test 1, 2, and 3 respectively (Waxman <i>et al.</i> , 2013).....	19
Figure 1.11: Mass flow rate-Time history for test 1, 2, and 3 respectively (Waxman <i>et al.</i> , 2013)	19

Chapter 2

Figure 2.1: Combustion chamber cross-section	24
Figure 2.2: Old combustion chamber assembly	25
Figure 2.3: New injector bulkhead.....	26
Figure 2.4: Nozzle cross-section	27
Figure 2.5: Fuel grain cartridge assembly.....	28
Figure 2.6: Thermal liner mould	29
Figure 2.7: Machined thermal liner.....	29
Figure 2.8: Particle settling investigation	30
Figure 2.9: Grain casting tooling	32
Figure 2.10: Grain casting step 1	33
Figure 2.11: Grain casting step 2	33
Figure 2.12: Fuel grain cartridge before insertion of the pre-combustion chamber insert.....	34

Chapter 3

Figure 3.1: Oxidiser feed system	35
Figure 3.2: Electrically actuated ball valve.....	37

Figure 3.3: Custom-developed valve (Design 1)	38
Figure 3.4: 1/2" ball valve with reduced port	39
Figure 3.5: Two piece ball valve stem assembly	39
Figure 3.6: Custom-developed valve (Design 2) – rendered	40
Figure 3.7: Custom-developed valve (Design 2) - mounted on stand.....	41
Figure 3.8: Supercharge process	43
Figure 3.9: Purge mode schematic	44
Figure 3.10: Dump mode	45
Figure 3.11: Run tank before cleaning (left) and after cleaning (right)	46
Figure 3.12: Relief valve.....	47

Chapter 4

Figure 4.1: cDAQ chassis and module.....	48
Figure 4.2: NI 9474 wiring diagram	50
Figure 4.3: Pressure transducer current loop	51
Figure 4.4: Oxidiser tank mass measurement	52
Figure 4.5: Arduino UNO R3 servo valve control board.....	53
Figure 4.6: Termination system	55
Figure 4.7: Auto-sequence control structure.....	57
Figure 4.8: DAQ assistant window	58
Figure 4.9: Auto-sequence code.....	59
Figure 4.10: LabVIEW – Notifications.....	60
Figure 4.11: LabVIEW-Normal mode	61
Figure 4.12: LabVIEW- Purge mode	62
Figure 4.13: LabVIEW - Dump mode	62
Figure 4.14: Message box handling	63
Figure 4.15: Propellant tank mass, signal conditioning	64
Figure 4.16: Filter configuration.....	64
Figure 4.17 Virtual instrument panel	65
Figure 4.18: Manual control.....	66
Figure 4.19: Auto-sequence	67
Figure 4.20: Operating mode selector.....	67
Figure 4.21: Real time charting	68

Chapter 5

Figure 5.1: Aluminium powder under magnification	69
Figure 5.2: Characteristic velocity vs. O/F ratio	70
Figure 5.3: Regression rate simulation – Pure and aluminised paraffin wax.....	71

Chapter 6

Figure 6.1: Steel wool test 1	73
Figure 6.2: Steel wool test 2	73
Figure 6.3: Steel wool test 3	74
Figure 6.4: Steel wool test 4	75
Figure 6.5: Match heads proof of concept	76
Figure 6.6: Pyrotechnic igniter.....	77

Chapter 7

Figure 7.1: Pressures P3 and P4 during cold flow testing.....	80
Figure 7.2: Pressures P2 and P4 during cold flow testing.....	81
Figure 7.3: Discharge coefficients (numeric-GmbH, 2015)	82

Chapter 8

Figure 8.1: LH-001 nozzle plume	84
Figure 8.2: Key pressure histories of the LH-001 test	85
Figure 8.3: Thrust history of the LH-001 test	85
Figure 8.4: Fast Fourier transform of the LH-001 test chamber pressure history.....	86
Figure 8.5: Recirculation zone stability (Sutton and Biblarz, 2001a).....	87
Figure 8.6: Fluid mechanic uncertainty in the pre-combustion chamber.....	87
Figure 8.7: LH-001 fuel grain cross-section	88
Figure 8.8: LH-003 nozzle plume	89
Figure 8.9: Key pressure histories of the LH-003 test	90
Figure 8.10: Thrust history of the LH-003 test	90
Figure 8.11: LH-003 fuel grain cross-section	91

Figure 8.12: LH-007 nozzle plume	92
Figure 8.13: LH-007 key system pressures.....	93
Figure 8.14: LH-007 thrust plot.....	93
Figure 8.15: Chamber pressure FFT – LH-007.....	94
Figure 8.16: Copper nozzle after LH-007.....	95
Figure 8.17: LH-007 fuel grain cross-section	95
Figure 8.18: LH-005 exhaust plume	96
Figure 8.19: LH-005 key system pressures.....	97
Figure 8.20: LH-005 thrust plot.....	97
Figure 8.21: Burning aluminium ejected during hot fire testing.....	98
Figure 8.22: Aluminium collected from fencing.....	98
Figure 8.23: Slag formation on the nozzle during test LH-005	99
Figure 8.24: Nozzle with removed accumulation	100
Figure 8.25: LH-005 fuel cross-section	100
Figure 8.26: LH-006 nozzle plume	101
Figure 8.27: LH-006 key system pressures.....	102
Figure 8.28: LH-006 thrust plot.....	102
Figure 8.29: Aft end molten aluminium.....	103
Figure 8.30: Damaged nozzle	104
Figure 8.31: Nozzle diverging end.....	104
Figure 8.32: Injector flange after LH-006.....	105
Figure 8.33: LH-006 fuel cross-section	105
Figure 8.34: LH-008 nozzle plume	106
Figure 8.35: LH-008 key system pressures.....	107
Figure 8.36: LH-008 thrust plot.....	107
Figure 8.37: Chamber pressure FFT – LH-008.....	108
Figure 8.38: Chamber pressure FFT	109
Figure 8.39: Nozzle accumulation	109
Figure 8.40 : Melted throat area.....	110
Figure 8.41: LH-008 fuel cross-section	110
Figure 8.42: Fore-end regression rate data.....	112
Figure 8.43: Density specific impulse data.....	113
Figure 8.44: Comparison of experimental and theoretical characteristic velocities for a 40% aluminised fuel grain	114
Figure 8.45: Comparison of experimental and theoretical characteristic velocities for pure paraffin wax hot fire testing	115
Figure 8.46: Combustion efficiencies for pure and aluminised fuel grains	115

Figure 8.47: Total impulse data - comparison 117

List of Tables

Chapter 1

Table 1.1: Additives and their properties (Chiaverini and Kuo, 2006).....	7
Table 1.2: Effect of weight percentage of metal additive on regression rate (Chiaverini and Kuo, 2006)	10
Table 1.3: Effect of metal additives on regression. Adapted from (Chiaverini and Kuo, 2006)	11
Table 1.4: Results of LiALH ₄ experimentation. (Desain <i>et al.</i> , 2008).....	13
Table 1.5: Properties of nitrous oxide and carbon dioxide. Adapted from (Waxman <i>et al.</i> , 2013).....	21

Chapter 2

Table 2.1: Combustion chamber materials	24
Table 2.2: Sasol Wax 0907 physical properties (Sasol GmbH, 2013).....	31

Chapter 3

Table 3.1: Flow properties for 1/4" and 1/2" tubing	36
Table 3.2: Custom-developed valve specifications.....	41

Chapter 7

Table 7.1: Pressure drop calculation data	79
Table 7.2: Initial injector design data.....	82

Chapter 8

Table 8.1 : Hot fire testing summary	83
Table 8.2: LH-001 data summary	84
Table 8.3: Tabulated fuel grain measurements and regression rate	88
Table 8.4: LH-003 data summary	89

Table 8.5: Tabulated fuel grain measurements and regression rate	91
Table 8.6: LH-007 data summary	92
Table 8.7: Tabulated fuel grain measurements and regression data	95
Table 8.8: LH-005 data summary	96
Table 8.9: Tabulated fuel grain measurements and regression rate	100
Table 8.10: LH-006 data summary	101
Table 8.11: Tabulated fuel grain measurements and regression data	106
Table 8.12: LH-008 data summary	107
Table 8.13: Tabulated fuel grain measurements and regression data	111
Table 8.14: Summary of key parameters from hot fire testing	111

Nomenclature

Symbol	Description	Units
a	Regression coefficient	$\text{mm}^{2n+1}/\text{kg}^n \text{s}^{1-n}$
\hat{a}	Dynamic pressure exponent	-
A	Area	m^2
b	Boundary layer delay coefficient	-
B	Blowing coefficient	-
c	Speed of sound	m/s
C	Specific heat capacity	kJ/kg
c^*	Characteristic velocity	m/s
C_d	Coefficient of discharge	-
D	Diameter	m
f	Frequency	Hz
G	Mass flux	$\text{kg/m}^2 \cdot \text{s}$
h	Enthalpy	kJ
I	Impulse	$\text{N} \cdot \text{s}$
l	Effective nozzle throat length	mm
L	Combustion chamber length	m
\acute{L}	Fuel grain length	m
M	Acoustic wave multiple	-
\dot{m}	Mass flow rate	kg/s
n	Mass flux exponent	-
O/F	Oxidiser to fuel ratio	-
P	Pressure	bar

\dot{r}	Solid fuel regression rate	mm/s
R	Molar gas constant	$\text{J}\cdot\text{mol}^{-1}\cdot\text{K}^{-1}$
SG	Specific Gravity	-
t	Time	s
T	Temperature	$^{\circ}\text{C}$
V	Volume	m^3
x	Axial position	m

Subscripts

Symbol	Description
1	State point upstream of injector
2	State point downstream of injector
<i>ac</i>	Acoustic
<i>ave</i>	Average
<i>b</i>	Duration of burn time
<i>c</i>	Combustion chamber
<i>cor</i>	Corrected constant of exhaust
<i>crit</i>	Critical point
<i>ent</i>	Entrainment
<i>f</i>	Final
<i>fp</i>	Fuel production
\bar{F}	Average thrust
<i>g</i>	Gas
<i>HEM</i>	Homogeneous equilibrium model

<i>hm</i>	Helmholtz
<i>i</i>	Initial
<i>inj</i>	Injector
<i>ox</i>	Oxidiser
<i>p</i>	Port
<i>pg</i>	Gas mixture in exhaust
<i>s</i>	Solid
<i>sp</i>	Specific
<i>SPI</i>	Single phase incompressible
<i>t</i>	Throat
<i>v</i>	Constant volume
<i>vap</i>	Vaporisation

Greek Symbols

Symbol	Description
β	Mass fraction of condensed matter
$\hat{\beta}$	Dynamic thickness exponent
γ	Ratio of specific heats
Δ	Change-in
η	Efficiency
μ	Combustion gas velocity
ρ	Density

1. Literature review

1.1. Introduction – fundamentals of hybrid rocket propulsion

Conventionally, a hybrid rocket motor uses a liquid or gaseous oxidiser and a fuel that is in solid form. The hybrid rocket motor configuration is less susceptible to chemical explosion as the fuel and oxidiser are in different states and are only mixed when intended. In liquid bi-propellant rocket engines, a leak or rupture in either of the vessels that hold the oxidiser or fuel can result in mixing of propellants and a subsequent explosion. In the case of solid propellant rocket motors, the fuel and oxidiser are premixed, increasing the risk of a chemical explosion. Hybrid rocket motors are therefore safer to operate when compared with the above mentioned bi-propellant and solid rocket motors. Figure 1.1 is a schematic of a typical hybrid rocket motor.

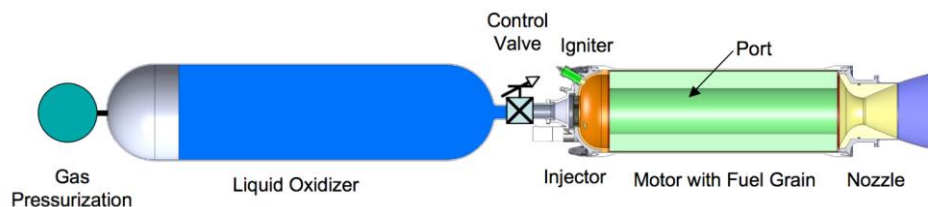


Figure 1.1: Hybrid Rocket Motor (Cantwell, 2014)

The fuel grain, which is contained within the combustion chamber, is perforated along its axis by a flow channel or port. Upon ignition of the motor, the oxidiser flows through the port and produces a diffusion flame along its entire length. Combustion is sustained via the heat transfer between the flame and the surface of the fuel grain, which causes continuous fuel vaporisation.

Hybrid rocket motors using classical, vaporising fuels operate by means of boundary layer combustion which involves diffusive mixing of fuel vaporised at the surface of the fuel grain and the oxidizer flowing through the port (Cantwell, 2014).

This classical combustion mechanism is illustrated in Figure 1.2. The x-axis is the axis of the port, and \dot{r} represents the fuel regression in the radial direction. As can be seen in Figure 1.2 the diffusion flame is located within the boundary layer.

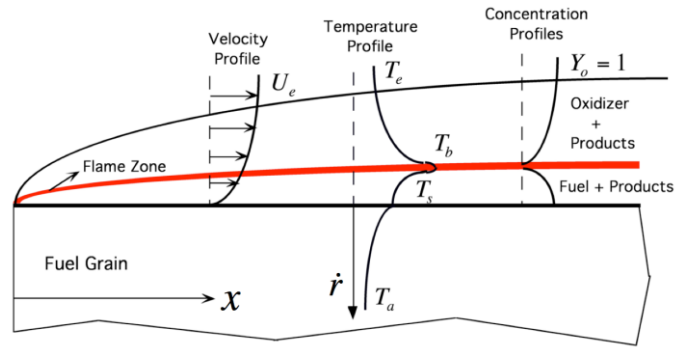


Figure 1.2: Boundary Layer Combustion (Cantwell, 2014)

Although hybrid rocket motor designs have various safety advantages over conventional designs, they have historically not been employed successfully for large scale commercial applications. This is due to the low regression rates associated with the classical vaporising fuels that have been used in the past. The fuel mass flow and hence thrust, are increased by using complex multiport designs that increase the burning surface area (Cantwell, 2014).

1.2. Development of paraffin wax-based propellant

Despite the safety and cost advantages that hybrid rocket motors have over liquid and solid propellant-based motors, they suffer from low regression rates which degrades the overall performance of the system. The use of multi-port designs have several disadvantages such as, low volumetric loading of the fuel, structural integrity issues and increased cost and complexity.

Over the years, several techniques have been proposed to overcome this shortcoming. These include adding flow devices to increase the turbulence level within the port and adding swirl to the oxidiser flow. Both methods lead to increased design complexity (Karabeyoglu *et al.*, 2001).

In classical hybrid rockets that utilise solid, liquefying fuels, a liquid layer forms on their burning surface. This layer is hydrodynamically unstable and leads to droplet entrainment into the gas stream. This shear-driven instability is increased as the viscosity and surface tension of the liquefied fuel is lowered.

Laboratory-scale tests conducted at Stanford University have shown that paraffin wax fuels regress three to four times faster than vaporising fuels such as hydroxyl-terminated polybutadiene (HTPB), due to physical characteristics of the liquid layer that is formed (Karabeyoglu *et al.*, 2001).

It was determined that the viscosity and surface tension of the melt layer plays an important role in defining the entrainment characteristics of a fuel. Fuels which have higher viscosity and surface tension, such as high-density polyethylene (HDPE), do not exhibit high regression rates. Even though HDPE forms a liquid layer, the viscosity of the liquid layer is in the region of four orders of magnitude higher than fuels such as paraffin wax. This explains the slow burning rate of typical polymeric fuels that exhibit liquefaction.

The laboratory-scale tests performed at Stanford confirmed that paraffin wax fuels exhibit higher regression rates when compared to polymeric fuels.

1.3. Regression rate theory

Regression rate in the context of hybrid rocket motors refers to the rate at which the solid fuel regresses normal to the surface of the grain and is governed by physical phenomena of heat and mass transfer from the flame zone to the fuel surface (Karabeyoglu *et al.*, 2001). Regression rate is one of the central parameters used to help characterise the performance of a hybrid rocket motor and is a vital parameter in the design process.

This section discusses regression rate and the physical characteristics of paraffin wax-based fuels that allow for high regression rates. Methods of further increasing regression rate via control of the melt layer viscosity and surface tension will also be discussed as per the work of (Nakagawa and Nikone, 2011). The regression of classical polymeric fuels are also briefly discussed for comparison.

Using classical regression theory, an equation for the rate of diffusion-based regression of classical fuels can be derived to yield the following expression (Boronowsky, 2011).

$$\dot{r} = 0.036 \frac{G^{0.8}}{\rho_s} \left(\frac{\mu}{x} \right)^{0.2} B^{0.23} \quad (1.1)$$

Here, μ is the combustion gas viscosity, x is the axial position in the port, ρ_s is the density of the solid fuel, G is the oxidiser mass flux and B is the blowing coefficient. It should be noted that the Eq. 1.1 is only valid in fuels that are not blackened or doped with metal additives. The addition of metal additives and blackening compounds increases the radiative heat transfer to the solid fuel grain.

To determine regression rate experimentally rather than analytically, the following equation is used and fitted to experimentally obtained data (Marxman and Gilbert, 1963):

$$\dot{r} = aG_{ox}^n \quad (1.2)$$

Taking the logarithm of both sides of the equation yields:

$$\log(\dot{r}) = \log(a) + n\log(G_{ox}) \quad (1.3)$$

In Equation 1.2 and 1.3, \dot{r} is the regression rate of the solid fuel, a is the regression coefficient, G_{ox} is the oxidiser mass flux and n is the mass flux exponent.

Equation 1.3 is in linear form, and if plotted, the ballistic coefficients ‘a’ and ‘n’ are simply determined by the Y – intercept and the gradient of the straight line, respectively.

The coefficients ‘a’ and ‘n’ are obtained from experimental data specifically associated with a given propellant. G_{ox} is the oxidiser mass flux and is defined as:

$$G_{ox} = \frac{\dot{m}_{ox}}{\pi \frac{D_p^2}{4}} \quad (1.4)$$

Where, \dot{m}_{ox} is the mass flow rate of the oxidiser and D_p is the diameter of the port. In contrast to solid rocket motors, hybrid rocket motor regression rate is largely insensitive to chamber pressure within a given oxidiser flux range. With a high oxidiser flux, the effects of chemical kinetics become more important. At low fluxes, radiation becomes the dominating force in terms of the fuel regression rate. It is also worth noting that for solid rocket motors, the flame is normally much closer to the solid grain surface, resulting in a regression rate that is one order of magnitude larger (Cantwell *et al.*, 2009).

1.4. Regression of polymeric fuels

Polymeric fuels such as HDPE do not burn as fast as saturated hydrocarbon based fuels such as pentane or wax. Even though thermoplastic polymers form a melt layer, the viscosity of the melt layer is around four orders of magnitude greater than paraffin wax-based fuels. Due to this, particle droplet entrainment is not achieved (Karabeyoglu *et al.*, 2001). As such, the regression of polymeric fuels is diffusion-based (vaporisation) rather than a combination of fuel vaporisation and droplet entrainment. Figure 1.3 shows the diffusion-based combustion mechanism that is seen with classical polymeric fuels.

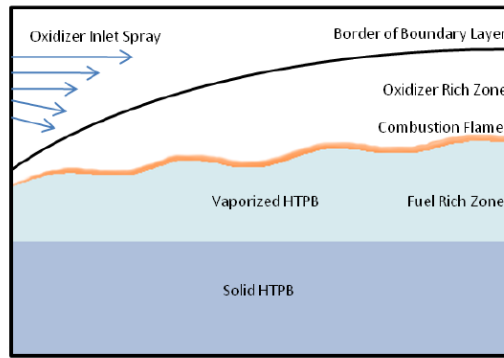


Figure 1.3: Regression of Classical Fuels (Boronowsky, 2011)

1.5. Regression of paraffin wax-based fuels

As heat is transferred to the surface of the solid fuel grain, a melt layer of kinematic viscosity μ is produced. Some of the melted fuel is vaporised from the melt layer and the remainder is entrained into the gas stream as droplets, or travels to the downstream end of the motor via shear forces within the port (Nakagawa and Nikone, 2011).

This explains the high regression rate seen with paraffin wax-based fuels that is not present in polymeric fuels. This process is illustrated in Figure 1.4.

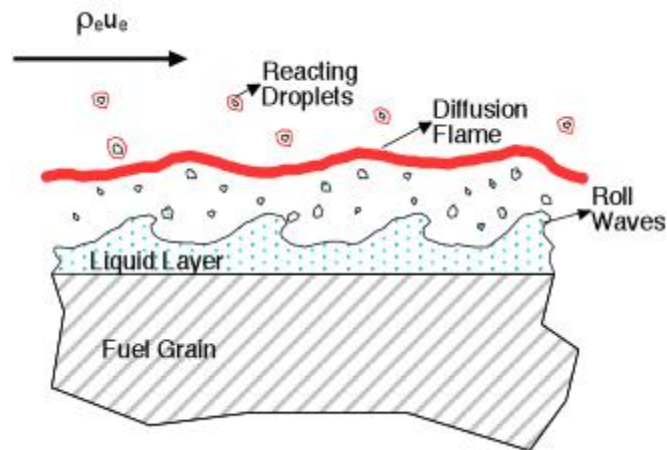


Figure 1.4: Paraffin wax regression (Space Propulsion Group, no date)

Since the fuel regression mechanism of paraffin wax-based fuels fundamentally differs from the processes described in the classical diffusion model, modifications to the model are required to account for the fuel mass transfer via droplet entrainment.

Heat is transferred to the solid fuel grain via convective and radiative processes, and the heat transferred to the fuel is sufficient to create a liquid melt layer on the surface of the grain. The turbulent, high velocity gas flow through the port causes the liquid layer to become unstable. The shearing forces imparted by the flow causes ripples in the liquid layer and droplets are pulled up through the boundary layer by means of entrainment. The droplets then come into contact with the oxidiser rich zone and combust (Karabeyoglu *et al.*, 2001). Overall regression rate can be quantified according to two terms associated with the mass transfer via vaporisation and the mass transfer via droplet entrainment (Karabeyoglu *et al.*, 2001).

$$\dot{r} = \dot{r}_{vap} + \dot{r}_{ent} \quad (1.4)$$

In turn, the entrainment-based regression rate can be expressed as:

$$\dot{r}_{ent} = a_{ent} \frac{G^{2\hat{a}}}{r^{\hat{\beta}}} \quad (1.5)$$

Where, \dot{r} is the total regression rate as a sum of the fuel regression due to both vaporisation and droplet entrainment, \dot{r}_{vap} is the fuel regression rate due to vaporisation of the fuel, \dot{r}_{ent} is the regression rate due to droplet entrainment, a_{ent} is the entrainment parameter, G is the mass flux of the oxidiser, \hat{a} is the dynamic pressure exponent and, $\hat{\beta}$ is the dynamic thickness exponent.

In a study by (Nakagawa and Nikone, 2011), the use of Ethylene Vinyl-acetate copolymer (EVA) as an additive in mass percentages of between 0 – 20%, to modify the viscosity of the melt layer and therefore the regression rate of the paraffin wax.

It was concluded that the regression rate of the paraffin wax-based fuel increases in proportion to $\mu^{-1/6}$. The heat flux to the solid fuel grain increases as the melt layer viscosity decreases. Since higher percentage masses of EVA increased the viscosity of the melt layer, the regression rate was decreased.

Although there was a decrease in regression rate of the fuel, this study demonstrated that the viscosity of the melt layer and heat transfer to the solid fuel grain can be modified by the addition of additives.

1.6. Energetic additives

Since the mid 1950's, there has been growing interest in metal additives regarding solid and hybrid rocket motors since the addition of metal additives increases the heat transfer rate to the solid fuel and produces a higher flame temperature via their combustion.

It was found that the addition of aluminium particles substantially increased specific impulse and density specific impulse. It was also found that the combustion of these metal additives also has the effect of damping out potential pressure oscillations in the chamber due to the formation of condensed phase products (Chiaverini and Kuo, 2006).

This section reviews some of the metal additives that have previously been used to increase motor performance. The combustion mechanics are described and the influence on motor performance evaluated. The following table presents details concerning some of the metals that have previously been used or have potential use as additives.

Table 1.1: Additives and their properties (Chiaverini and Kuo, 2006)

Fuel	Virgin material properties			Gravimetric heat of oxidation kJ/gm _{fuel}	Volumetric heat of oxidation kJ/cm ³	Final Oxide	Final Oxide Properties			
	ρ	T _{melt}	T _{boil}				ρ	T _{melt}	T _{boil}	ΔH_f
	g/cm ³	°C	°C				g/cm ³	°C	°C	kJ/mol
Aluminium (Al)	2.70	660	2497.00	31.1	83.9	Al ₂ O ₃ (s)	3.97	2054.00	3800.00	-1676.00
Boron (B)	2.34	2077	2550.00	58.7	137	B ₂ O ₃ (s)	2.46	450.00	2065.00	-1273.00
Beryllium (Be)	1.85	1287	2468.00	66.5	123	BeO(s)	3.01	2530.00	3900.00	-609.00
Carbon (C)	2.25	3652	N/A	32.8	73.8	CO ₂ (g)	0.00198	-56.60	-78.50	-394.00
Iron (Fe)	7.86	1535	2750.00	7.39	58.1	Fe ₂ O ₃ (s)	5.24	1462.00	-	-826.00
Lithium (Li)	0.53	181	1342.00	43.2	23	Li ₂ O(s)	2.01	>1700	-	-598.00
Magnesium (Mg)	1.74	649	1107.00	24.7	43	MgO(s)	3.58	2832.00	3260.00	-601.00
Silicon (Si)	2.33	1412	3217.00	32.3	75.2	SiO ₂ (s)	2.20	1732.00	2590.00	-904.00
Titanium (Ti)	4.50	1663	3358.00	19.7	89.6	TiO ₂ (s)	4.26	1830 - 1850	2500 - 3000	-939.00
Tungsten (W)	19.35	3407	5660.00	4.59	88.8	WO ₃ (s)	7.16	1473.00	-	-838.00
Zirconium (Zr)	6.49	1852	4377.00	12	78.1	ZrO ₂ (s)	5.60	2677.00	-	-1098.00
HTPB	0.92	241	-	43.3	39.8	-	-	-	-	-

1.6.1. Aluminium (Al)

Aluminium has been previously used to increase regression rate and combustion temperature in hybrid rocket motors. Additionally, the O/F (Oxidiser – Fuel) ratio is lowered, allowing for a more compact rocket to be constructed as less oxidiser is required to burn an equivalent volume of an aluminised fuel grain compared to pure paraffin wax fuel grain. Tests conducted at Stanford University show that a 40% aluminised paraffin wax/nitrous oxide propellant has a regression rate 25% higher than that of pure paraffin wax (McCormick *et al.*, 2005).

The paraffin wax/nitrous oxide propellant combination has values for a and n of 0.155 and 0.5 respectively. For aluminised paraffin wax, the value of a has been shown to be 10% higher. (McCormick *et al.*, 2005) have found that an aluminium loading of 40% provides the maximum value for c^* , the characteristic velocity. The data in Figure 1.5 was produced by NASA CEA for different quantities of aluminium power and paraffin wax at a chamber pressure of 2.41 Mpa.

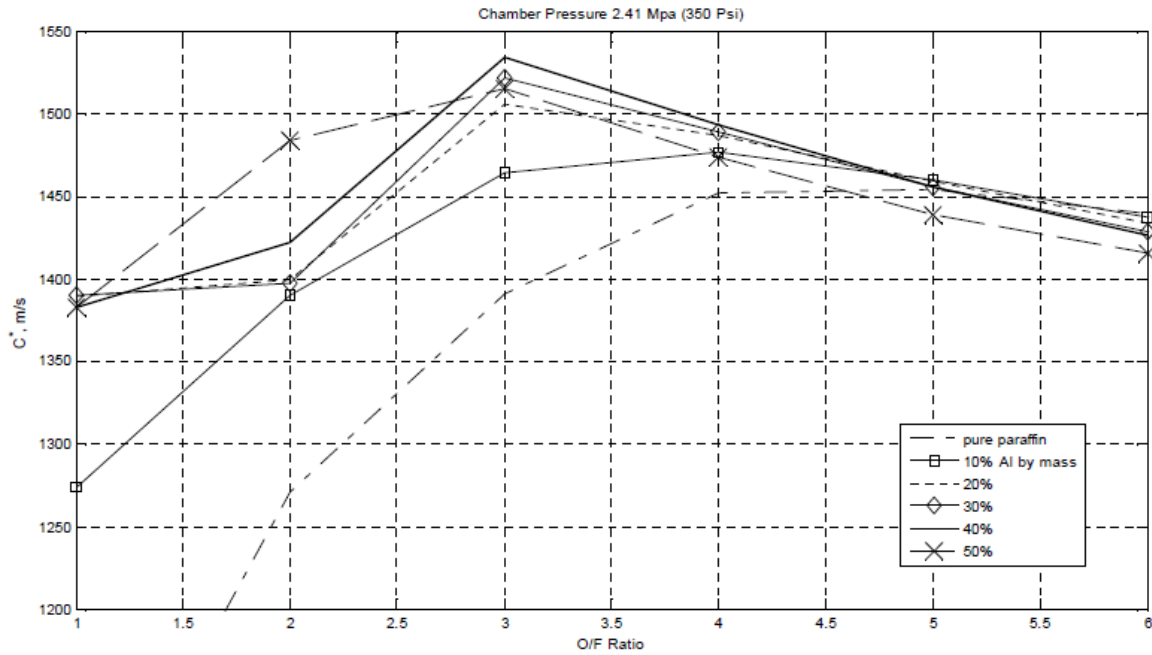


Figure 1.5: c^* of aluminised paraffin vs. O/F ratio from the CEA code (McCormick *et al.*, 2005).

An additional motivation for aluminium as an additive is its high enthalpy of formation. It is an inexpensive and widely available material compared to additives such as magnesium, therefore several research efforts have been made to understand the mechanics of aluminium oxidation.

Previous research has described the process of aluminium oxidation as a boundary layer combustion process, with a flame surrounding the aluminium particle and where combustion is supported by the diffusion of metal vapour at the particles surface.

Thermogravimetry and differential thermal analysis has shown that aluminium nanoparticle formation as a result of an electrical wire explosion can ignite at temperatures as low as 550 °C. This is lower than the ignition temperature of micron sized aluminium particles. Other studies have shown that the activation energy of aluminium nanoparticles is smaller than bulk aluminium. This information suggests a relationship between particle size and activation energy. Studies performed by (Rai *et al.*, 2006) showed that the enthalpy of combustion of bulk aluminium is -1675 KJ/mole and the combustion of an isolated aluminium atom is -2324 KJ/mole. The latter value is the most that can be theoretically achieved from the combustion of aluminium. The free surface energy for bulk aluminium is 0.8878 J/m², this is reduced by a factor of 1.04 when the particle size is 1 nm. It was concluded by the author that the increased burning rate of aluminium nanoparticles is due to the chemical kinetics of the reaction rather than the thermodynamics.

Experimentation involving oxidising nanoparticles at temperatures of 800, 900 and 1000 °C showed that the particles oxidised at above 1000 °C were hollow in nature after heating, compared to particles heated at 800 and 900 °C that were all solid spheres after heating. Figure 1.6 shows the density variation of aluminium nanoparticles as a function of the oxidation temperature.

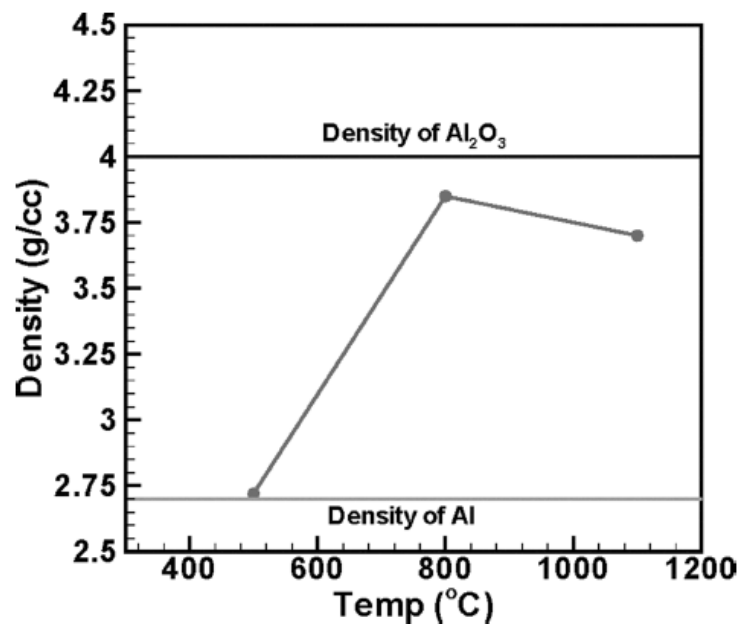


Figure 1.6: Density of aluminium particles after oxidation at varying temperatures (Rai *et al.*, 2006).

As can be seen, an increase in density occurs up to a temperature of 800 °C which corresponds to the generation of aluminium oxide (Al_2O_3). At temperatures above 800 °C, the density is shown to decrease as a result of the particles hollowing-out. This result suggests an outward diffusion of aluminium through the aluminium oxide shell.

At the melting point, particle density changes from 2.7 g/cc to 2.4 g/cc. The resulting expansion causes the aluminium oxide shell to be placed in tension since the oxide shell expands negligibly. Consequently, the aluminium core is put into compression. The presence of this pressure gradient may result in thinning or rupturing of the aluminium oxide shell, therefore increasing the reaction rate.

Oxidation of aluminium nanoparticles therefore proceeds in two distinct regimes. At temperatures below the melting point of aluminium, oxidation proceeds by the diffusion of oxygen through the oxide shell. This is a slow regime with a low reaction rate. Above the melting point of aluminium, the oxidation is far more rapid due to thinning and/or rupturing of the oxide shell and the subsequent diffusion of aluminium and oxygen.

A study conducted by (Farbar *et al.*, 2007), evaluated the performance of high-density metallised fuel grains consisting of either aluminium or magnesium in an HTPB binder, being oxidised by 90% hydrogen peroxide. The following observations were noted after a total of eight hot fire tests:

In one of the eight tests, a high nozzle erosion rate was recorded with an initial and final throat diameter of 10.5 mm and 14.2 mm respectively, using a nozzle with a moulded silica phenolic resin and graphite throat insert. This erosion rate was attributed to the surface impingement of particulate matter on the nozzle surface.

While no agglomeration was seen in the hot fire tests with pure HTPB, the 40 % aluminium and 60% HTPB hot fire tests showed molten slag accumulation on the nozzles converging face. It was found that the molten accumulation was reduced at higher chamber pressures.

In terms of the stability of the rocket motor, combustion instabilities at 4 Hz were seen with the Al/HTPB combination. This was due to a process called “chuffing”, periodic shedding of the alumina layer formation on the fuel grain exposing the virgin fuel. This was counteracted by added a turbulator upstream of the fuel grain. The addition of the turbulator also has the effect of increasing regression rate.

As reported by (Karabeyoglu and Arkun, 2014), in the 1970’s, a series of experiments was conducted by the German Research and Development Institute for Air and Space Travel. One of the experiments included testing fuel grains made from either Al, Si, B, Mg and a mixture of Mg and Al. These additives were set in a polyurethane binder and FLOX (40% Fluorine – Oxygen) was used as an oxidiser. During this experiment, aluminium with particle sizes ranging from 32 μm to 240 μm were used. Of significance, no measurable difference was seen in linear regression when all other variables were kept constant. Table 1.2 shows the aluminium-based fuel grains that were tested as well as the measured regression rate and oxidiser mass flux.

Table 1.2: Effect of weight percentage of metal additive on regression rate (Chiaverini and Kuo, 2006)

Test number	Propellant Combination		$r_{b,av}$ mm/s	G_{ox} kg/m ² S
	Fuel	Oxidiser		
1	40% Al / 60% PU	FLOX – 40	0.47	73.6
2	60% Al / 40% PU	FLOX – 40	0.64	65.1
3	60% Al / 10% C / 30% PU	FLOX – 40	0.70	65.1
4	80% Al / 20% PU	FLOX – 30	0.66	65.1

Data associated with the first and second test show that a 20% increase in aluminium increases the regression rate, even though the oxidiser mass flux was lower in the case of the 60% aluminium test. The inclusion of 10% carbon further increased the regression rate with a fixed percentage of aluminium. At 80% aluminium, a reduction in regression rate was observed.

When comparing the second and fourth propellant combinations, it can be seen that the additional 20% aluminium increases regression rate by 0.02 mm/s. These two tests provide a good comparison since the same oxidiser and mass flux is applied.

1.6.2. Magnesium (Mg)

Similar results associated with the application of magnesium as a metallisation additive by (Chiaverini and Kuo, 2006), are presented in Table 1.3.

In Table 1.3, Mg-3 refers to 3 % magnesium and Mg -50 refers to 50 % magnesium, as a fraction of the total fuel mass.

Table 1.3: Effect of metal additives on regression. Adapted from (Chiaverini and Kuo, 2006)

Propellant		r_{av}	G_{ox}
Fuel	Oxidiser	mm/s	kg/m ² .s
60 % Al - 40% PU	FLOX – 40	0.64	65.1
60% Al & Mg-3 – 40% PU	FLOX – 40	0.62	73.6
60% Al & Mg-50 – 40% PU	FLOX – 40	0.73	73.6
60% Mg – 40% PU	FLOX – 40	0.74	73.6

There is limited literature on the use of Mg as a rocket propellant due to its high cost and reduced energetic performance, limiting commercial use as a propellant.

Current research involves the use of pure magnesium and carbon dioxide (CO₂). This propellant combination has been proposed as a green alternative to the current hydrocarbon and solid propellant motors used today since magnesia (reaction by-product) is environmentally benign. Since the Martian atmosphere is 95% CO₂ and trace elements of magnesium has been found on the Martian surface, this propellant combination can one day be used to for manned missions to Mars. The propellants yield a

low specific impulse (200 s) but are still viable due to the prospect of using these propellants for Mars propulsion as well as the reduced O/F ratio (Shafirovich and Varma, 2008).

1.6.3. LiAlH₄ (Lithium aluminium hydride)

The addition of lithium aluminium hydride into paraffin wax based fuels has been studied with gaseous oxygen as an oxidiser (Gox). LiAlH₄ has the ability to ignite in the presence of strong acids such as nitric acid. The reaction between paraffin wax doped with 10% LiAlH₄ and nitric acid is hypergolic. Figure 1.7 shows the relationship between I_{sp} and O/F ratio for varying percentages of LiAlH₄.

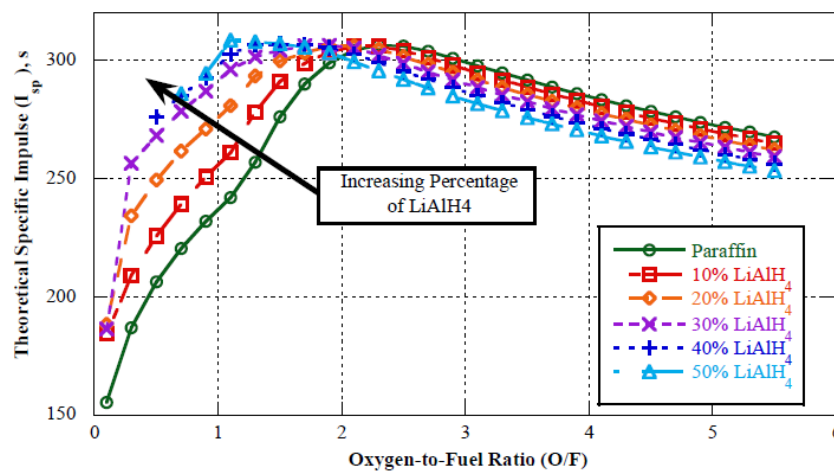
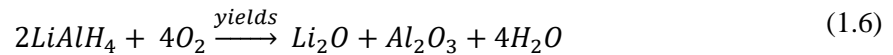


Figure 1.7 O/F vs I_{sp} for LiAlH₄ (Larson *et al.*, 2015)

As can be seen in the graph, the peak theoretical specific impulse does not substantially increase as the percentage mass of LiAlH₄ increases, although the O/F ratio is shifted to a lower value. The above results were predicted for a chamber pressure of 69 bar and a nozzle expansion ratio of 10. The 10% LiAlH₄ showed a regression rate of 2.6 mm/s that was obtained by measuring the fuel grain diameter pre and post burn after a given hot fire test.

From hot fire testing with 10% LiAlH₄ by mass in paraffin wax, deposition of unreacted fuel was found downstream of the fuel grain on the post-combustion chamber area as well as the nozzle. It was concluded that the LiAlH₄ particles may have been too large and the melting point of the wax too low resulting in the deposition that was seen. Using a wax with a higher melting point would allow for more complete combustion due to a higher flame temperature on the burning surface. It was also noted that microscopic examination of the LiAlH₄ particles after 300 hours of ball milling revealed particles with an alumina layer, which could have inhibited combustion (Larson *et al.*, 2015).

(Desain *et al.*, 2008) studied the effects of LiAlH₄ in paraffin wax with regard to regression rate by preparing candle like samples and burning them in atmosphere. Four paraffin wax/ LiAlH₄ samples were prepared consisting of 0%, 7%, 20% and 24% LiAlH₄ by mass. The wax was melted at 70 degrees in order to prevent LiAlH₄ decomposition. The LiAlH₄ was added to the melted wax in a nitrogen purge bag and then left to solidify into a cylindrical sample. It was found that the paraffin wax/ LiAlH₄ mixture was stable once solidified and exposed to the atmosphere. The oxidation of LiAlH₄ proceeds in the following manner (Desain *et al.*, 2008):



The metal oxides that are produced from this reaction are 1.73 times heavier than LiAlH₄ thus, the sum of the solid products formed after the sample has been burnt is more than the original mass of the sample. A mass balance was used to calculate the total mass loss of paraffin wax/ LiAlH₄.

It was found that the 7% LiAlH₄ sample had a burn rate close to that of pure paraffin wax. There was, however, a considerable increase in burn rate with the 20 – 24% samples, which displayed a burn rate 14 times greater than the 0 -7 % samples. The complete set of results for the experiment are presented in Table 1.4.

Table 1.4: Results of LiAlH₄ experimentation. (Desain *et al.*, 2008)

Composition (% LiAlH₄)	Calculated mass loss (g/min)	Average of 3 trials (g/min)
0	0.047	0.048
0	0.049	
0	0.047	
7	0.077	0.075
7	0.050	
7	0.097	
20	0.831	0.736
20	0.724	
20	0.652	
24	1.228	0.0959
24	0.758	
24	0.890	

As a note, the paraffin wax/ LiALH₄ mixtures were exposed to the atmosphere for a period of 5 weeks and showed no reactivity. Paraffin wax/ LiALH₄ samples were exposed directly to water and showed no self-ignition and a very low reaction rate. It was concluded that the addition of LiALH₄ does indeed increase the burn rate of paraffin wax fuels. Additionally, since the paraffin wax provides an adequate layer of protection, the mixture is safe for long term storage.

1.7. Mixed flow theory

The combustion of aluminium in a rocket motor will produce aluminium oxide that is included in the exhaust stream. If the aluminium oxide particles have a diameter of 0.005 mm or less, the particle will travel in the jet with a velocity that closely matches the velocity of the gases (Sutton and Biblarz, 2001b). In addition, the solid particles will effectively be in thermal equilibrium with the gas flow.

As the particle diameter is increased, the particles mass (and inertia) increase according to the particle diameter cubed. Drag force, however, increases according to the square of the particle diameter. As a result, larger-sized particles do not travel as fast as the exhaust gases and do not yield their heat as readily as small particles do.

Due to this, the larger particles of condensed matter possess a smaller momentum (due to their lower velocity) than an equivalent mass of small particles. The particles in the exhaust reach the nozzle exit at a higher temperature because they have yielded less thermal energy.

Based on the following assumptions, a set of equations have been formulated in order to more accurately construct analytical models in hybrid rocket motors which use additives that generate non-gaseous products (Sutton and Biblarz, 2001b). In deriving these equations, the following assumptions were made:

- Specific heats of gasses and solids stay constant throughout.
- The particles are small enough to move at the gas velocity and are in thermal equilibrium with the gas flow.
- There is no mass exchange (vaporisation or condensation)
- No chemical reactions take place.

The set of equations are:

$$h = (1 - \beta)C_{pg}T + \beta C_s T \quad (1.7)$$

$$V = V_g(1 - \beta) \quad (1.8)$$

$$P_c = \frac{R_g T}{V_g} \quad (1.9)$$

$$R_{cor} = (1 - \beta)R_g \quad (1.10)$$

$$\gamma = \frac{(1 - \beta)C_p + \beta C_s}{(1 - \beta)C_v + \beta C_s} \quad (1.11)$$

Equations 1.7 to 1.11 are a set of correction factors that allow for nozzle performance parameters to be calculated with the presence of condensed matter in the exhaust stream. The symbol h is the enthalpy of the exhaust, β is the mass fraction of condensed matter in the exhaust, C_{pg} is the specific heat capacity of the gas mixture in the exhaust, C_s is the specific heat capacity of the solid matter in the exhaust, T is the temperature of the exhaust, V is the total volume inside the combustion chamber, V_g is the gas volume inside the combustion chamber, P_c is the combustion chamber pressure, R_{cor} is the corrected molar gas constant, R_g is the corrected molar gas constant of the gas mixture in the exhaust, γ is the ratio of specific heats of the exhaust containing the condensed matter and gas mixture, C_p and C_v are the specific heat capacities of the gas mixture in the exhaust at constant pressure and volume, respectively.

1.8. Stability theory

The following section is a review of the research that has been conducted in the focus area of hybrid rocket motor stability. In the field of hybrid rocketry, it is not uncommon for the combustion chamber pressure to display oscillations. These oscillations can occur for a several reasons and vary in both amplitude and frequency. They will be discussed in the following section.

Experimental testing of a paraffin wax and gaseous oxygen hybrid rocket motor undertaken by Stanford University and the NASA Ames Research Centre, showed three distinct frequency oscillation peaks in the chamber pressure. Pressure oscillations in the combustion chamber were measured with a pressure transducer upstream of the injector and in the combustion chamber. The peaks occurred at 30 Hz, 100 Hz and 350 Hz (De Zilwa *et al.*, 2003).

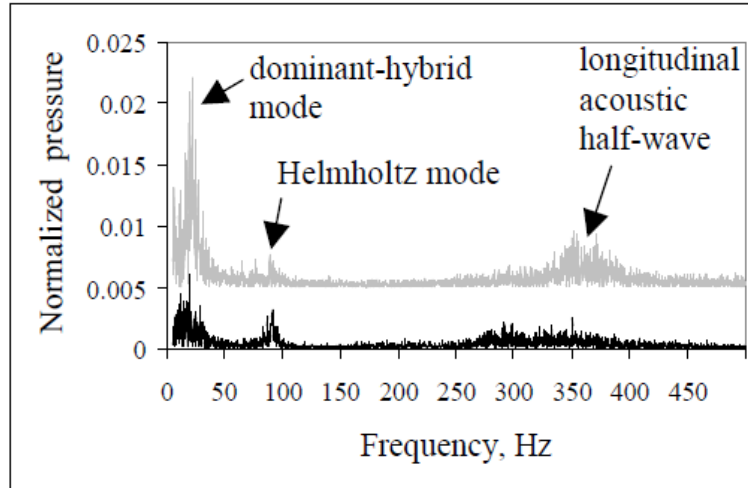


Figure 1.8: Frequency vs Normalised pressure - static testing
(De Zilwa *et al.*, 2003)

The 30 Hz pressure oscillation was characterised as the dominant hybrid oscillation, and was attributed to unstable fuel production triggered by vortex shedding in the pre-combustion chamber region. For a given hybrid rocket combustion chamber, the instability can range from 10 Hz to 50 Hz and can be estimated using the following relationship.

$$f_{fp} = \frac{0.48}{b} \left(2 + \frac{1}{O/F} \right) + \frac{G(RT)_{ave}}{\hat{L}P_c} \quad (1.12)$$

Where, f_{fp} is the frequency of the instability in terms of fuel production, b is a boundary layer delay coefficient, O/F is the oxidiser to fuel ratio of the propellants, G is the oxidiser mass flux, $(RT)_{ave}$ is the product of the average temperature and molar gas constant during the burn, \hat{L} is the length of the fuel grain, and P_c is the combustion chamber pressure.

Further evidence for the fuel production oscillation is shown by the high-speed camera footage of the exhaust plume. The images, captured in 5 ms intervals, show distinct variation in exhaust plume shape, as can be seen in Figure 1.9

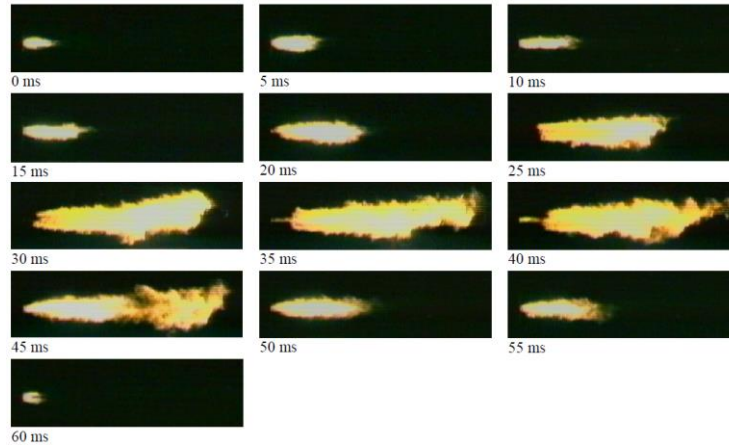


Figure 1.9: Exhaust plume oscillation (De Zilwa *et al.*, 2003)

The combustion chamber Helmholtz mode was detected at 100 Hz and it was found that pressure oscillations due to the dominant-hybrid oscillation resulted in reduced fluctuations in the Helmholtz oscillation. Amplification of these instabilities were therefore not a concern. The Helmholtz frequency can be estimated using the following equation where f_{hm} is the Helmholtz frequency, c is the speed of sound in the given medium, A_t is the cross-sectional area of the throat, V is the volume of the interior of the motor, that is, the volume of the port, pre- and post-combustion chambers and l is the effective length along the axis of the throat.

$$f_{hm} = \frac{c}{2\pi} \sqrt{\frac{A_t}{Vl}} \quad (1.13)$$

Pressure oscillations in the 350 Hz range were associated with the longitudinal half wave in the rocket motor. Analysis showed that amplification of the dominant-hybrid oscillation by the longitudinal half wave oscillation is indeed possible. The acoustic mode of the combustion chamber can be found using the following relation:

$$f_{ac} = \frac{cM}{L} \quad (1.14)$$

Where, f_{ac} is the acoustic frequency associated with the instability, c is the speed of sound in the medium in question, M is an acoustic multiple, and L is the length of the combustion chamber.

Further research in the field suggests that low frequency pressure oscillations can be predicted using the following relationship (Karabeyoglu *et al.*, 2005).

$$f = 0.2341 \left(2 + \frac{1}{O/F} \right) \frac{G_{ox} R T_{ave}}{L P_c} \quad (1.15)$$

Where, f is the frequency of the instability, O/F is the oxidiser to fuel ratio, G_{ox} is the mass flux of the oxidiser flowing through the port, R is the molar gas constant, T_{ave} is the average combustion temperature in the port, L is the length of the combustion chamber, and P_c is the combustion chamber pressure.

This universal scaling formula is in good agreement with observed instabilities in forty-three motor tests, across a range of geometries and propellant combinations, including oxidisers such as liquid oxygen, gaseous oxygen and nitrous oxide.

The authors further suggested that design of the fore end of the motor is critical in minimising combustion instabilities. The injector configuration and pre-combustion chamber geometry affect the extent of commonly-observed low frequency instabilities.

The same research also showed that the longitudinal acoustic oscillations often coexist with low frequency oscillations and concluded that it is possible that the high frequency oscillations are driven by low frequency oscillations.

There are also instabilities that are coupled to the oxidiser feed system, which usually present as regular sinusoidal pressure oscillations in the combustion chamber. The mechanisms that contribute to this coupling are (1) feed system compressibility effects, (2) an oxidiser mass flow rate that shows dependency on chamber pressure, and (3) the delay of combustion/vaporisation in the combustion chamber.

Typically, a cavitating venturi is used in the feed system to decouple the combustion chamber from the feed system. In systems that utilize nitrous oxide, vapour formation in the feed system is undesirable as this increases the risk of a decomposition event.

As will be discussed in section 1.9, the mass flow rate through the injector increases with decreasing downstream pressure. This happens until some critical point where the flow becomes choked. When this happens, the injector acts as an isolating element, effectively decoupling the combustion chamber from the feed system. Pressure and time histories corresponding to three hot fire tests are shown in Figure 1.10 and Figure 1.11. All of the tests were performed with carbon dioxide at an initial temperature of 293 K. The difference between each of the three tests was the chamber pressure (P_2). The pressure P_1 is the upstream injector pressure and P_s shows the vapour pressure of the nitrous oxide at its given temperature (Waxman *et al.*, 2013).

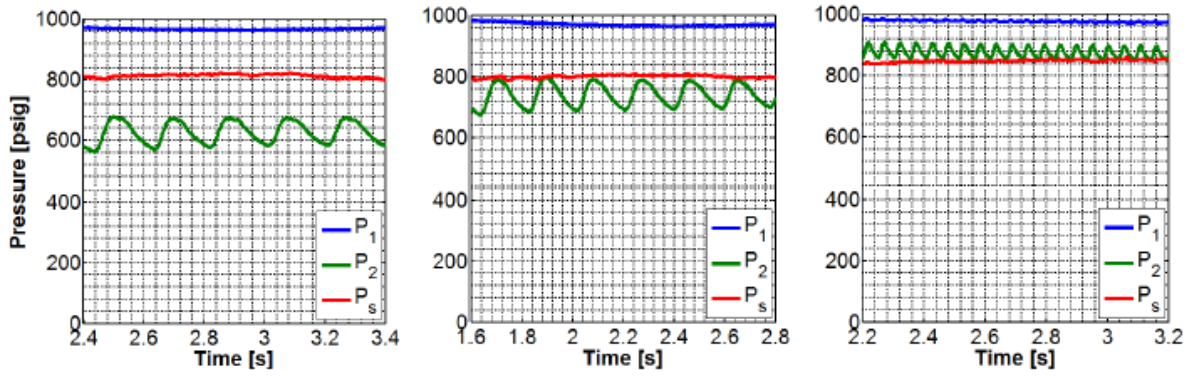


Figure 1.10: Pressure-Time history for test 1, 2, and 3 respectively (Waxman *et al.*, 2013)

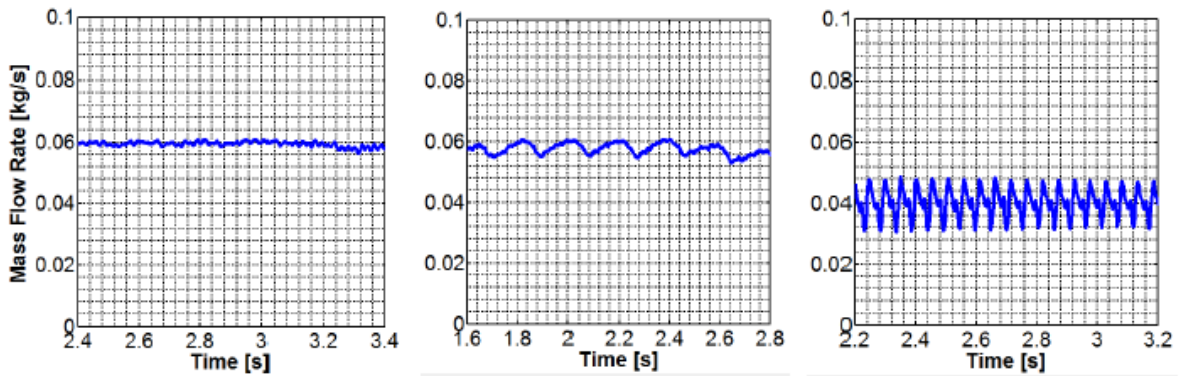


Figure 1.11: Mass flow rate-Time history for test 1, 2, and 3 respectively (Waxman *et al.*, 2013)

The results in Figure 1.10 (test 1) indicate that when the chamber pressure (seen in green) is sufficiently below the vapour pressure of the oxidiser, the mass flow rate of oxidiser (Figure 1.11 – test 1) shows little to no dependence on the chamber pressure oscillations. However, if the downstream pressure is above the saturation pressure, there is a clear interaction between the chamber pressure disturbances and the oxidiser mass flow rate. This is illustrated in the third test in Figure 1.10 and Figure 1.11 (Waxman *et al.*, 2013).

1.9. Injector design and theory

Since N_2O is a self-pressurising oxidiser, it has gained significant popularity in hybrid rocket propulsion applications. Nitrous oxide has a vapour pressure of approximately 50.3 bar at room temperature. This allows for the oxidiser to be expelled from the oxidiser tank under its own pressure without the need for complex pressurisation systems. To date, significant research has been conducted on the design of injectors and feed systems that utilise nitrous oxide. This is particularly because it has been established in the field that correct injector design is vital for safe motor operation, high combustion efficiency and the mitigation of combustion instabilities (Waxman *et al.*, 2013).

The equation to calculate mass flow rate for single-phase incompressible flow through the injector is defined as:

$$\dot{m}_{SPI} = C_d A \sqrt{2\rho\Delta P_{inj}} \quad (1.16)$$

Where, \dot{m}_{SPI} is the mass flow rate through the injector, C_d is the coefficient of discharge based on the injector orifice geometry, A is the total cross-sectional area of the injector orifice(s), ρ is the density of the oxidiser passing through the injector, and ΔP_{inj} is the pressure drop across the injector.

In the injector, the local static pressure can drop well below the vapour pressure of the fluid, leading to flash vaporisation and a loss in density. For a low vapour pressure oxidiser, as the downstream pressure decreases, the mass flow rate through the injector increases until some critical point where the flow through the injector becomes choked. To account for these phenomena, a model known as the homogenous equilibrium model (HEM) is used to calculate the mass flow rate through the injector, accounting for the two-phase flow regime. This model assumes that the two phases are in thermal equilibrium with each other and are travelling at the same velocity (Waxman *et al.*, 2013). The HEM model is defined as follows:

$$\dot{m}_{HEM} = C_d A \rho_2 \sqrt{2(h_1 - h_2)} \quad (1.17)$$

Where, \dot{m}_{HEM} is the mass flow rate through the injector in the two-phase regime, C_d is the coefficient of discharge based on the injector orifice geometry, A is the total cross-sectional area of the injector

orifice(s), ρ_2 is the density of the oxidiser downstream of the injector exit, h_1 and h_2 represent the enthalpy of the fluid before the injector and at the exit plane.

With the pressure and temperature upstream of the injector known, the mass flow rate at critical flow conditions can be calculated according to Eq. 1.18.

$$\dot{m}_{crit,HEM} = \dot{m}_{HEM} \left| \frac{\Delta \dot{m}_{HEM}}{\delta P_2} = 0 \right. \quad (1.18)$$

Where, $\dot{m}_{crit,HEM}$ is the critical mass flow rate in the two-phase regime, \dot{m}_{HEM} is the mass flow rate through the injector in the two-phase flow regime, δP_2 is the change in the downstream injector pressure (chamber pressure).

While each of these models are useful under select circumstances, data for injector discharge coefficients is limited. Experimental research by the same authors involved the fabrication of 5 injectors with a fixed length of 18.4 mm. A series of tests was then performed, which involved varying the injector orifice diameter and the orifice inlet geometry to determine the effect of C_d , the discharge coefficient on the mass flow rate through the injector, for both the single phase incompressible model and the homogeneous equilibrium model. Three of the injectors were square-edged with varying orifice diameters, one was round-edged with an orifice diameter of 1.5 mm, and the other had chamfered edges and a 1.5 mm orifice diameter. The tests used CO₂ as an analogue for N₂O. The two fluids are thermodynamically similar and therefore CO₂ is used to minimize the safety hazards posed by N₂O (Waxman *et al.*, 2013). The following table shows various thermodynamic properties for the two fluids so that the similarities can be seen.

Table 1.5: Properties of nitrous oxide and carbon dioxide. Adapted from (Waxman *et al.*, 2013)

Property	Units	Nitrous Oxide (N ₂ O)	Carbon Dioxide (CO ₂)	Difference (%)
M	amu	44.013	44.010	+0.007
P _c	Mpa	7.25	7.38	+1.80
P _{trip}	Mpa	0.088	0.518	+491
T _c	K	309.6	304.2	-1.74
T _{trip}	K	182.3	216.6	+18.8
ρ_c	kg/m ³	452.0	467.6	+3.45
Z _c		0.273	0.274	+0.366
ω		0.160	0.255	+40.6

Analysis of the results obtained via experimentation showed that for low pressure drops through the injector (0.207 to 1.38 Mpa), the single-phase incompressible model describes the flow well (Waxman *et al.*, 2013). The authors further concluded the following:

- C_d in the single-phase regime is inversely related to the injector orifice diameter.
- When the chamber pressure drops sufficiently below the vapour pressure of the oxidiser, critical mass flow occurs.
- Chamfering or rounding the inlet of the injector orifice produces an enhancement in mass flow rate, both in the single-phase and two-phase flow regimes.
- There is almost no distinction between rounding and chamfering.
- Carbon dioxide is a suitable analogue for nitrous oxide.

1.10. Summary of literature review

Studies performed at Stanford University show that regression rate can be increased by 25% with the addition of 40% aluminium to paraffin wax. Figure 1.5 shows that the optimal mass fraction to maximise the characteristic velocity is 40% aluminium by mass. The work done by (Chiaverini and Kuo, 2006) suggests that further increases in regression rate can be achieved by increasing the percentage aluminium to 80% with PU as a binder/fuel and FLOX – 40 as the oxidiser. Whether this is the case for paraffin wax and nitrous oxide appears to remain undetermined.

With reference to aluminium, many of the publications that have been reviewed report high nozzle erosion rates and slag formation in the converging face of the nozzle and/or the combustion chamber. Experimentation shows that the slag accumulation in the combustion chamber can be mitigated by higher chamber pressures as reported by (Farbar *et al.*, 2007).

Table 1.1 shows various energy concentrations of metal additives used in hybrid and solid rocket motors. Aluminium has the highest volumetric and gravimetric heat of oxidation as well as the highest enthalpy of formation and density. With that being said, the literature shows that in certain studies, the use of magnesium as an additive results in a similar regression rate. The gravimetric and volumetric heats of oxidation and enthalpies of formation cannot explain this alone. Instead, this can be attributed to the differences between aluminium and magnesium from a chemical kinetics point of view.

It has been demonstrated that the use of metal additives creates a pressure dependence with respect to the regression rate. This creates an additional variable when choosing a propellant combination for a given use. Another factor to consider is particle size. Smaller-sized particles show decreased ignition

temperatures and enhanced chemical kinetics. The impact of particle size on regression rate requires further study.

Literature also shows that the condensed-phase products generated by aluminium combustion can potentially damp pressure oscillations in the combustion chamber. On the contrary, the process known as “chuffing”, the periodic shedding of the oxide layer, may lead to combustion instabilities in the order of approximately 4 Hz. This particular frequency was observed by (Farbar *et al.*, 2007). The reason for these conflicting observations has not been established.

At higher aluminium mass percentages, higher flame temperatures are produced. If this flame temperature exceeds the melting point of aluminium oxide, the formation of condensed alumina is prevented. Since the flame temperature is in excess of alumina’s melting point, the shearing effects will periodically shed the oxide layer and expose virgin fuel which will then oxidise and form a new layer. In this manner, the “chuffing” effect manifests. Additionally, pressure oscillations may become more distinct due to the lack of condensed alumina. The effect this will have on nozzle erosion and slag accumulation will need to be investigated.

Lithium aluminium hydride has also been researched as an additive in hybrid rockets utilising paraffin wax as a fuel. It has been noted that a stable mixture of LiAlH_4 and paraffin wax can be prepared and stored. While the concentration of LiAlH_4 does not appreciably affect theoretical peak specific impulse, the O/F ratio is significantly reduced from 2 to 1 with 50% LiAlH_4 and Gox as an oxidiser.

Since LiAlH_4 is reactive in water, it is imperative that handling is carried out in an inert nitrogen environment. This escalates complexity and cost of fuel grain manufacture. Furthermore, the storage of LiAlH_4 is an important consideration, as the substance forms a layer of alumina by reacting with even trace amounts of oxygen, making ignition more difficult. Exposure to humid conditions poses a significant risk as LiAlH_4 reacts violently with water.

2. Combustion chamber assembly

The combustion chamber assembly employed in this study was derived from a 2014 Discipline of Mechanical Engineering undergraduate project (Maharaj and Chetty, 2014). All assembly components were retained, apart from the injector bulkhead, which was modified for technical reasons. After a discussion of the modification that was made to the injector bulkhead, the nozzle that was also adopted from the 2014 undergraduate project, is briefly described. The design and fabrication of the fuel grain cartridge is then discussed. The fuel grain cartridge is the entire consumable assembly that is inserted into the combustion chamber.

Table 2.1 and Figure 2.1 describe the components and their materials in the assembly.

Table 2.1: Combustion chamber materials

Component	Description	Material
1	Combustion chamber	Vanadium steel
2	Combustion chamber flange	Mild steel
3	Injector bulkhead flange	Mild steel
4	Nozzle retaining flange	Mild steel
5	Manifold support	Mild steel
6	Manifold	304 Stainless steel
7	Injector	Brass
8	Nozzle	Copper
9	Capillary tube mounting point	Mild steel

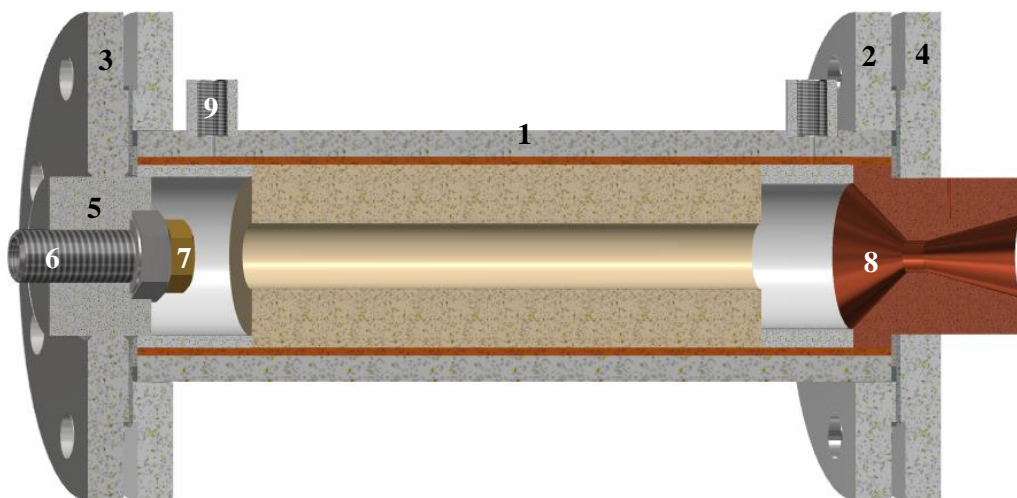


Figure 2.1: Combustion chamber cross-section

The fore-end of the assembly used grade 12.9, mild steel fasteners to couple the combustion chamber flange to the injector bulkhead flange. The aft end of the assembly used grade 4.8, mild steel fasteners to fasten the chamber flange to the nozzle retaining flange. The design mode of failure was the stripping of the threads on the aft end, grade 4.8 bolts. The intended failure was to depressurise the combustion chamber while keeping the injector end intact, allowing for the oxidiser to be expelled from the nozzle-end of the assembly.

2.1. Fore end modification

As part of the undergraduate project, a combustion chamber assembly was designed to test the use of pure metals as a fuel in hybrid rocket propulsion systems. The chamber wall was machined from vanadium steel, while the flanges, which mate the injector and nozzle bulkhead, were laser cut from mild carbon steel. Figure 2.1 shows a cross-section of the original chamber assembly before any modifications were made for this project.

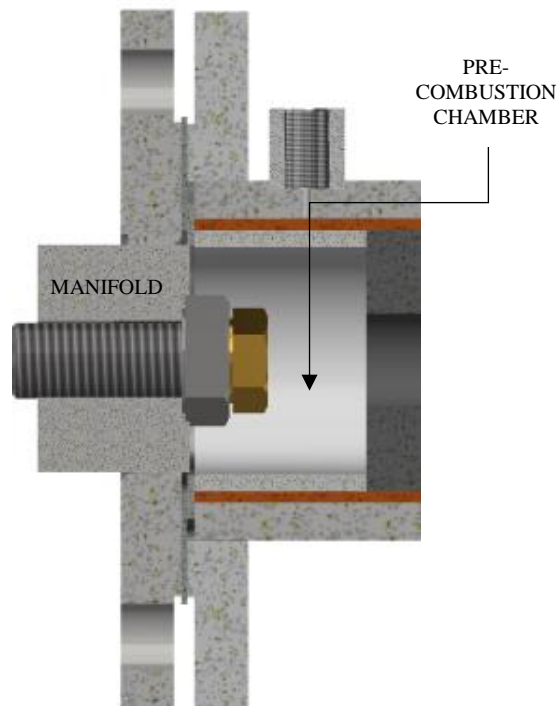


Figure 2.2: Old combustion chamber assembly

During the first hot fire test (discussed in Chapter 8), a high amplitude combustion instability was observed. This prompted the design of a new injector and injector bulkhead in order to mitigate the

pressure oscillations. In the original design, the injector screwed into a manifold which then screwed into the bulkhead. This configuration resulted in the injector protruding out of the bulkhead. Consequently, the transit time of the oxidiser droplets before reaching the fuel grain was reduced, and the recirculation zone that is normally formed in the pre-combustion chamber was disturbed.

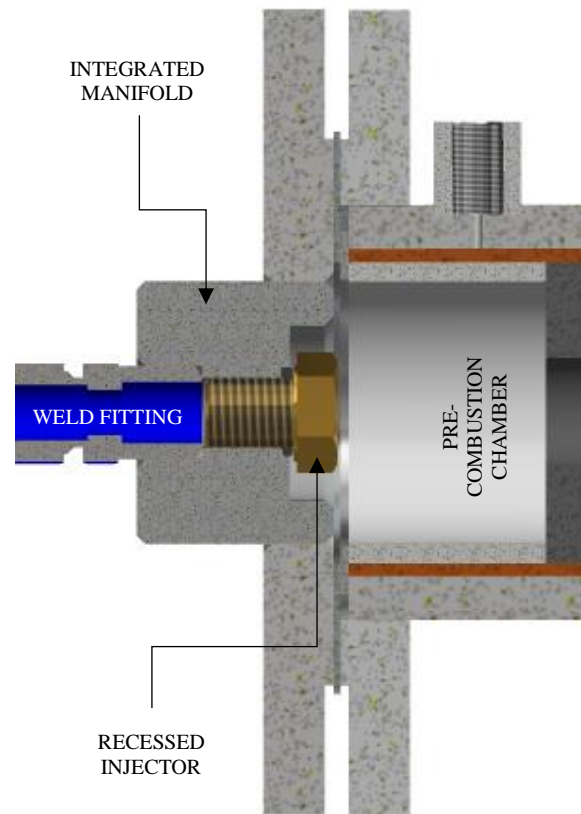


Figure 2.3: New injector bulkhead

With the injector recessed into the bulkhead, the effective length of the pre-combustion chamber was increased. This permitted a longer droplet transit time and promoted the formation of a recirculation zone in the pre-combustion chamber. The design revision successfully mitigated the combustion instability and allowed for a series of six further hot fire tests to be carried out.

To make the modification in Figure 2.3, a 60 mm hole was machined through the centre of the flange. A 60 mm diameter bar of 316 stainless steel, to be used as the injector manifold, was then welded to the 60 mm bore in the flange. A hole was drilled and tapped into the injector bulkhead for the injector to fasten on to and a groove was machined to accommodate a Viton O-ring used to seal the injector against the manifold. At the opposite end of the manifold, a 21.4 mm hole allowed for a 1/2" Swagelok weld fitting to be inserted and welded to the manifold. The use of a weld fitting permitted a high-pressure, robust seal between manifold and feed line.

To test the modified design after fabrication, a blank injector was inserted, the chamber was filled with water and then pressurised to 100 bar and held for 20 minutes. This confirmed the structural capacity of the assembly and the new injector bulkhead was subsequently put into service.

2.2. Nozzle

The nozzle design also followed on from the undergraduate project. It employed a simple conical design with a 45° converging angle, a 15° diverging angle, and a 12 mm diameter throat. A cross-section of the nozzle is shown in Figure 2.3.

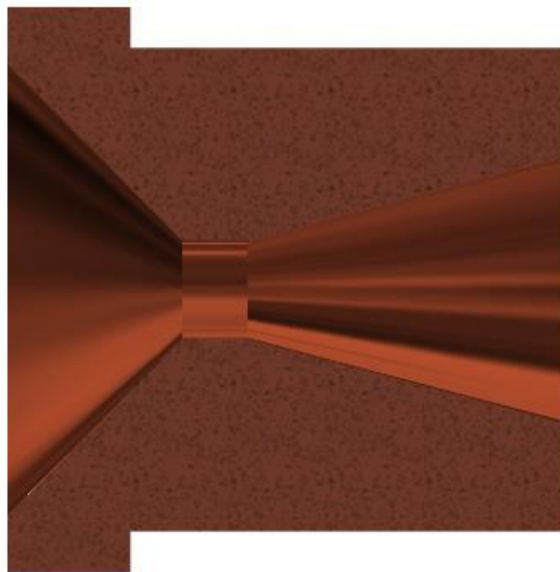


Figure 2.4: Nozzle cross-section

2.3. Fuel grain cartridge

The fuel cartridge was comprised of the fuel grain, the pre and post combustion chambers, and the thermal liner. The entire assembly was expendable and was changed after each hot fire test of the rocket motor. A cross-section of the fuel grain cartridge assembly is shown in Figure 2.5.

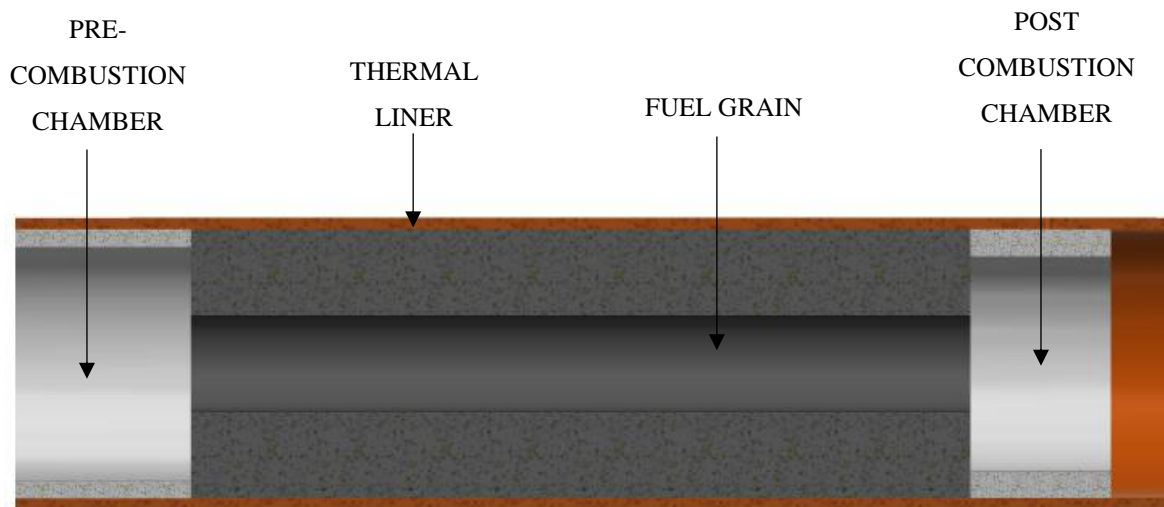


Figure 2.5: Fuel grain cartridge assembly

The pre-combustion chamber was required to generate a hot recirculation zone that pre-heats and decomposes the oxidiser, nitrous oxide. The post combustion chamber enables adequate mixing of the combustion products to promote full oxidisation before exiting through the nozzle. The thermal liner provides an ablative layer that protects the steel combustion chamber from being overheated. The inner diameter of the combustion chamber is 75 mm, which governs the outer diameter of the fuel grain cartridge. Using ratios derived from the laboratory-scale motor testing by (Lohner *et al.*, 2006), the lengths of the fuel grain, pre and post combustion chambers could be established, after adjustments were made for the protrusion of the old injector assembly.

2.4. Thermal liner

The thermal liner is a composite material made from phenolic formaldehyde resin, cotton, and glass fibre. Since the thermal liner was used for its ablative and insulating properties, rather than for mechanical strength, special attention was not paid to the orientation of the fibre material during fabrication.

The thermal liner was made on a two-piece mould that was machined from high density polyethylene (HDPE). At the time, this material was chosen due to ease of machining and availability. Figure 2.6 shows the mould with the two halves parts separated for illustrative purposes.

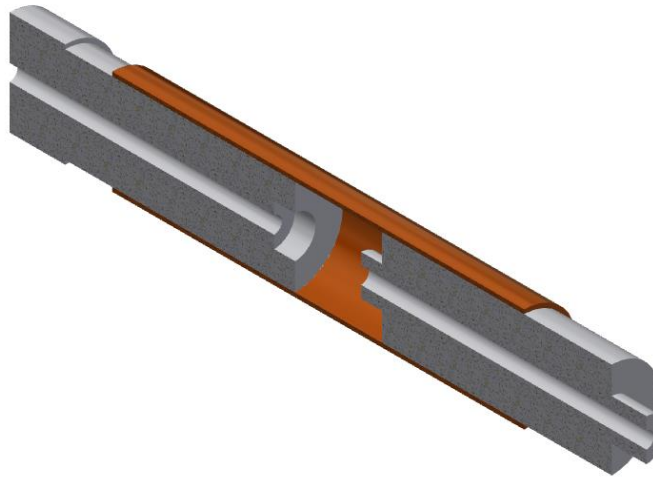


Figure 2.6: Thermal liner mould

The mould was made in two parts to allow for easier removal after laying-up the thermal liner. A 12 mm hole was drilled through the axis of the mould for a section of threaded bar to be inserted. This allows the mould to be rotated during the layup process. The mould has an outer diameter of 69 mm, which results in a 3 mm thick thermal liner.

To produce a thermal liner, the outer diameter of the mould was first coated by hand with a layer of PVA release agent followed by a single layer of wax paper. These two layers were found to ease the release process. The thermal liner was then made by laying-up layers of glass fibre and cotton with a brush and composite roller. The process was stopped once the liner exceeds 75 mm in diameter. The thermal liner was then left at room temperature for 12 hours followed by an 8-hour post-curing at 80 °C. Once this curing process was complete and the liner had been left to cool back down to room temperature, the entire mould and liner were put into a freezer for 2 hours, at which point the thermal liner simply slid off the mould.

The liner was layed-up to approximate dimensions and subsequently needed to be machined down to its final dimensions. Figure 2.7 shows a completed thermal liner, post machining.



Figure 2.7: Machined thermal liner

Since the combustion chamber was made from extruded steel, there were variations in the inner diameter along the length of the chamber. These variations were found to be ± 1.5 mm. Because of this, each liner was machined to a precise, tight fit in the combustion chamber.

2.5. Fuel grain casting

In the past, only pure paraffin wax fuel grains were produced, thus a short investigation into the casting of aluminium powder was required. A large concern at the time was being able to produce a fuel grain that was a homogeneous mixture. Four samples of 60 g of paraffin wax were prepared in beakers and heated to 125 degrees C. Aluminium powder was then added to the wax to bring the mass up to 100 g. While in a molten state, stirring of the mixture was stopped at 120, 110, 100 and 90°C and the four samples were left to cool down to room temperature. The samples were then removed and cut in half to reveal the extent to the particle settling, as shown in Figure 2.8.

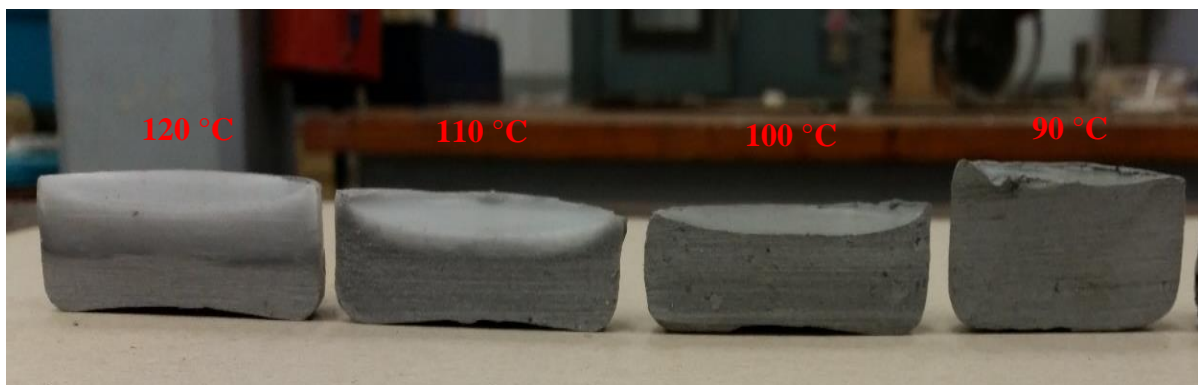


Figure 2.8: Particle settling investigation

As indicated, the amount of settling was reduced for mixtures that were mixed for a longer period, at a cooler temperature. Considerable settling was seen in the 120 and 110 °C samples while no observable settling was seen in the 100 and 90 °C samples. The temperature of 90 °C was in the range of the solidification point of the wax. The paraffin wax that was utilised for this project was Sasol Wax 0907 (Sasol GmbH, 2013). A summary of its physical properties is provided in Table 2.2.

Table 2.2: Sasol Wax 0907 physical properties (Sasol GmbH, 2013)

Solidification point (°C)	Oil content (%)	Viscosity at 100°C (mm²/s)
83 – 94	0.0 – 2.0	8.5 – 12.5

Typically, ASReG has cast paraffin wax fuel grains by pouring molten wax into a steel mould and compressing it with a piston to compensate for shrinkage during solidification. Previously, several grains had been cast using this approach for both laboratory-scale rocket motors and large sounding rocket motors. The primary problem with this casting method was that the grain was difficult to remove after it had cooled. Common practice had been to use a hydraulic press to remove the grain from the mould. Another problem was that the wax cooled down rapidly due to the conductivity of the steel mould, resulting in structural defects such as cracking. This was particularly evident in the winter months, where the ambient temperature of the laboratory was lower compared to the rest of the year.

For this project, it was proposed that the fuel grain be cast directly into the thermal liner. By doing this, the need for a separate mould was completely removed, and the grain would not be stressed by removing it from a separate mould. In addition, the thermal liner acts as an insulator, slowing the cooling rate when compared to steel. This method of casting the fuel grain directly into the thermal liner solves both problems that were previously encountered by the research group.

The assembly that was developed to enable in-liner casting is shown in Figure 2.9, in cross-section.

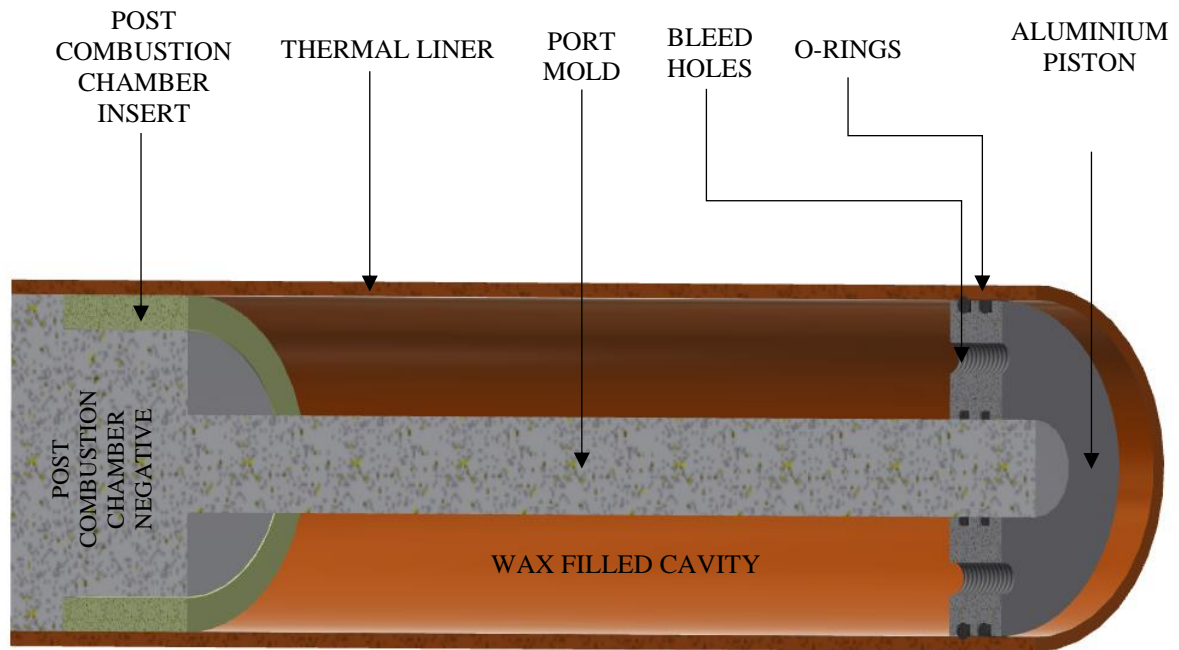


Figure 2.9: Grain casting tooling

The casting process for a pure wax grain was started by inserting a post combustion chamber insert on the post combustion chamber negative that is seen in Figure 2.9. The interface between the insert and the negative was then sealed with room temperature vulcanisation (RTV) silicone to prevent wax from penetrating the gap and preventing the negative from sliding out after casting. The port mold was then inserted into a hole drilled into the negative. The port mold was an aluminium pipe that was filled with hot water to release from the wax surrounding it upon removal. Figure 2.10 shows the assembly after these steps have been completed.



Figure 2.10: Grain casting step 1

RTV was then applied along the circumference of the post combustion chamber insert to seal it against the thermal liner. The port mould, negative, and post combustion chamber insert were then installed into the thermal liner and left overnight to allow the RTV to cure.

After curing, 2 kg of wax pellets were melted in a metal container in a temperature-controlled kiln at 120°C. The thermal liner was then inserted into a support container with insulation material around the thermal liner to slow the cooling rate. The metal support around the liner was used to ensure that the fuel grain cartridge remained vertical after a spring applied force to the piston for compression.



Figure 2.11: Grain casting step 2

The melted wax was then mixed with 2% carbon powder, by mass, to darken the fuel grain and limit the sub-surface penetration of radiation from the burning port surface area. It was then poured into the thermal liner to a level 15 mm beneath the top edge in order to permit the full penetration of the piston. The piston was then inserted into the thermal liner. O-rings around the inner and outer diameters of the piston created a seal, while the bleed holes vented air from under the piston. Once the air had been removed, the bleed holes were sealed with screws and the piston was pushed down by a spring. The use of a spring allowed the piston to travel while still applying a compressive force. During cooling of the wax, the piston travelled approximately 30 mm, corresponding to a shrinkage of 13% over the length of the fuel.

After leaving the grain to cool for 12 hours, the compression piston and port mould were removed by pouring boiling water over the surface of the piston and into the aluminium port mould, respectively. The fore-end surface of the fuel grain was then visually inspected for cavities and other imperfections. If the grain level was found to be too high, the fuel was machined down using a lathe. For illustration, a fuel grain cartridge in this stage of the fabrication process is shown in Figure 2.12, viewed from the fore-end.



Figure 2.12: Fuel grain cartridge before insertion of the pre-combustion chamber insert

Finally, the pre-combustion chamber insert was glued to the thermal liner with RTV, and once the RTV had cured, the fuel grain was ready to be installed into the combustion chamber.

3.1. Pipe sizing

To start the design process, a nitrous oxide flow rate of 0.5 kg/s was selected as the absolute maximum value that would be encountered in the injection line during normal operation. Using this fixed mass flow rate, a flow velocity and pressure drop were calculated for different pipe diameters. Since the existing components that were available were in imperial sizes, the entire oxidiser feed system was designed according to imperial units.

In general, it is desirable to minimise pressure drops along the nitrous oxide fluid paths to ensure that a large mass fraction of liquid oxidiser enters the injector orifice. This ensures that the injector produces the correct pressure drop to achieve the desired chamber pressure, assuming the injector was designed for single-phase flow. As a matter of safety, gaseous nitrous oxide, produced by cavitation inside the injection line, can potentially decompose in the presence of a contaminant and an ignition source, such as an electrostatic discharge (ESD), for example. Table 3.1 shows the injection line pressure drop that can be expected for different pipe diameters. For the calculations, a Darcy friction factor of 0.0289 was used (Nayyar *et al.*, 2000), in addition to a nitrous oxide fluid density of 743.9 kg/m³ and a duct length of 1.5 m.

Table 3.1: Flow properties for ¼” and ½” tubing

Nominal pipe size (inch)	Hydraulic diameter (mm)	Reynolds number	Flow velocity (m/s)	Pressure drop (bar)
¼	4.75	2.58E+06	37.9	48.6
½	10.9	1.12E+06	7.2	0.768

As can be seen in Table 3.1, for the given flow parameters, the use ¼” tubing results in an unacceptable pressure drop. All nitrous oxide flow paths were therefore designed to be ½” in diameter. All valves and tubing conveying nitrogen was sized as ¼”. This decision was based on the use of existing components and a tolerance for pressure drops.

3.2. Oxidiser flow control valve

Arguably one of the most important components in the oxidiser feed system was the valve responsible for controlling the flow of oxidiser to the combustion chamber. In designing and constructing the feed systems, it was required that an oxidiser valve be experimentally developed for implementation on the next sounding rocket designed by the ASReG research group. This custom-developed valve is marked “Servo System SBV1” in Figure 3.1.

The valve to the left of SBV1 is marked “Swagelok Valve ABV3”, a commercially available ½” ball valve that is electrically actuated. In operation, it takes approximately four seconds to open or close fully and uses a geared DC motor with limits at the opened and closed positions. A magnified view of the valve is provided in Figure 3.2.



Figure 3.2: Electrically actuated ball valve

While acceptable for use in a laboratory-scale configuration, the valve is unsuitable for flight use due to its size, mass and power requirements (24 VDC).

For redundancy, the oxidiser flow control valve in Figure 3.2 and the custom-developed valve were used in series with the custom-developed valve acting as the primary oxidiser valve and the Swagelok valve (ABV3) acting as a secondary backup.

Before development of the custom-developed servo valve, the following were set as design requirements:

- A quick-acting actuation system that opens in under two seconds
- A small and lightweight system that can be easily integrated into a sounding rocket

- Low power requirements such that it can be powered by a battery of reasonable size (i.e. fits within a 150 mm diameter)
- Can be produced with in-house equipment, quickly and inexpensively

With these design requirements in mind, a hobby servo motor that is commonly used in the radio-controlled industry was selected for use with the following attributes:

- High torque-to-weight ratio
- Small and lightweight
- Contains embedded electronics, making for simple actuation
- Operates on a nominal 6 VDC, allowing for it to be powered by a battery pack

The servo motor chosen was a FITEC FS6530M that operates between 4.8 and 6 VDC. The motor weighs 190 g and contains an internal metal gearing system that produces 2.95 Nm of torque. Actuation can be achieved via a pulse width signal that can be easily produced by a microcontroller such as those found on the Arduino platform. The motor coupled to the oxidiser control valve via a mounting system can be seen in Figure 3.3.

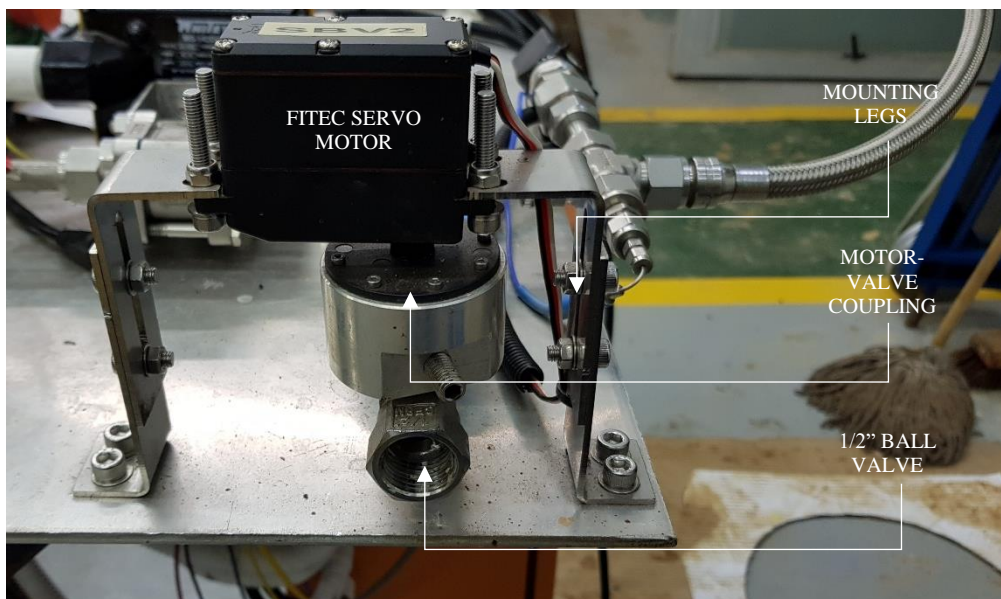


Figure 3.3: Custom-developed valve (Design 1)

Table 3.3 contains the specifications for the custom-developed valve that is seen in Figure 3.3

During cold flow testing of the valve, it was observed that the contraction in the flow path down to 8 mm from the pipe diameter of 10.9 mm caused vaporisation of the nitrous oxide and rapid cooling of the valve. In turn, the cooling increased the torque requirements of the valve past the 2.95 Nm capability

of the servo. This was despite the fact that previous testing showed that the valve operated normally at room temperature. Figure 3.4 shows the reduced port of the ball valve with the hydraulic diameter of the flow represented by the blue circle and the constriction represented by the red circle.

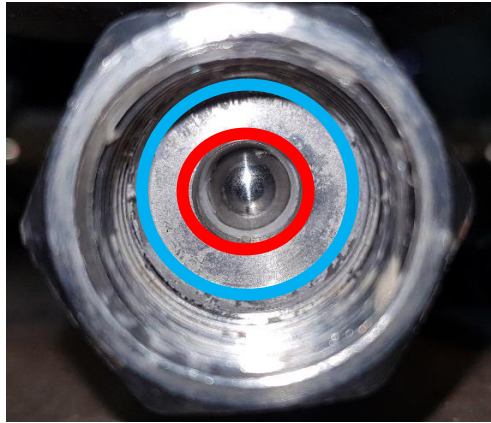


Figure 3.4: 1/2" ball valve with reduced port

The cold flow testing also showed non-repeatability at positions between 0 and 90 °. That is to say, when the valve stem is rotated back from 90° to some angle less than 90°, the valve does not move back to the same position each time which was found to be caused by the construction of the ball valve. The ball valve has a two-piece stem and ball; that is, that the ball and stem are two separate components and are mated to each other via a groove that was machined into the ball. This is illustrated in Figure 3.5.

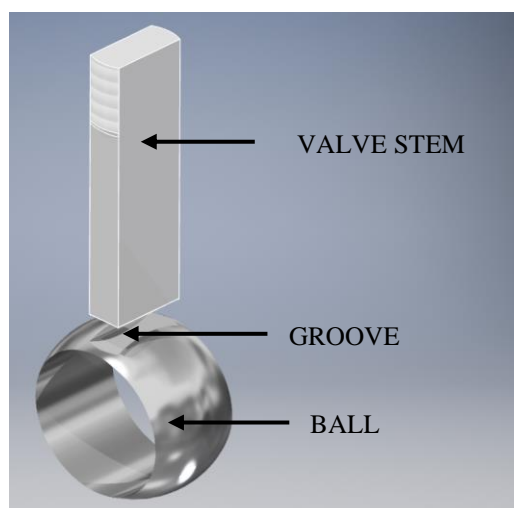


Figure 3.5: Two piece ball valve stem assembly

As can be seen, the valve stem was made to be slightly smaller than the groove that had been machined in the ball, the stem was allowed independent rotation before turning the ball. Since the custom-developed valve used a servo motor which used angular position feedback, the rotation of the motor's output shaft did not necessarily match the rotation of the ball.

Consequently, the oxidiser flow control valve needed to be changed. The new design used a Swagelok ½" single piece ball valve coupled to two Savox, high torque servo motors. The single piece instrumentation valve ensured that there was no relative rotation between the stem and ball. A disadvantage was that the torque requirements were much larger due to the internal friction inside the valve. The torque requirements were experimentally found to be approximately 9 Nm.

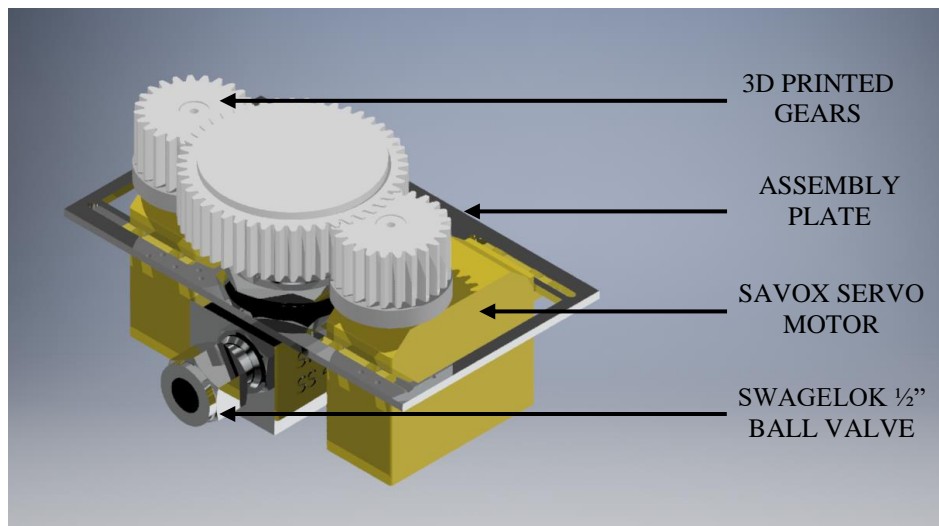


Figure 3.6: Custom-developed valve (Design 2) – rendered



Figure 3.7: Custom-developed valve (Design 2) – mounted on stand

Figures 3.6 and 3.7 show the revised servo ball valve that was used during hot fire and cold flow testing. The revised configuration uses a set of spur gears that were 3D printed from ABS plastic to achieve a gearing ratio of 2:1. The valve itself is a full bore valve. This means that there is no internal contraction in the valve body such as the contraction seen in Figure 3.4. The valve uses Swagelok tube fittings on either end which eliminates the use of adapters as in the case of the previous design. The motors are actuated by an Arduino board that receives communication from the LabVIEW-based control system that was developed (see Chapter 4). Cold flow testing verified that the valve performs normally under static and full flow conditions. Table 3.2 summarises the specifications of the first and second design versions of the custom-developed valve system. Green shading shows which system is superior in terms of the given parameter of interest.

Table 3.2: Custom-developed valve specifications

Parameter	Design 1	Design 2
Input voltage (VDC)	6	7.4
Gearing ratio	1	2
Maximum torque delivered to valve stem (Nm)	2.95	15.69
Zero load speed (sec/90 degrees)	0.3	0.255
Hydraulic flow diameter (mm)	8	10.7
Actuation speed at load (sec)	2.6	1.5
Minimum pulse width (μ s)	544	800
Maximum pulse width (μ s)	2400	1400
Refresh interval (μ s)	20000	20000

As can be seen, the second design iteration of the custom-developed valve rectifies the issues that were observed with the first design iteration by allowing for more torques to be delivered to the valve stem and using a full bore (no constriction) design. Design 2 was used to complete all the hot fire testing.

3.3. Supercharge system

Nitrous oxide is an oxidiser that is particularly hazardous in gaseous form. If the gas comes into contact with a catalytic contaminant in the feed line, an exothermic decomposition can occur. Another danger is the case where the nitrous oxide vapour comes into contact with a fuel contaminant. In this case, all that is required to initiate an explosive reaction is an ignition source, such as a static discharge.

These hazards can be mitigated to an extent by means of supercharging the nitrous oxide contained in the oxidiser tank, where an inert gas is used to pressurise the nitrous oxide in excess of its vapour pressure. For this work, nitrogen at 65 bar was used for supercharging purposes. Decomposition risk was lowered as a consequence of two effects. Firstly, the gaseous layer above the nitrous oxide liquid in the tank was desensitised by the dilution of the nitrogen gas. Secondly, a high-pressure differential between the injector inlet and combustion chamber was produced during motor start-up. This is desirable as hybrid rocket motors produce a high peak pressure during ignition and have a tendency to hard-start if the igniter is not energetic enough or timed badly. The schematic shown in Figure 3.8 illustrates the pressurisation of the nitrous oxide tank with nitrogen. Green valves are opened and red valves are closed.

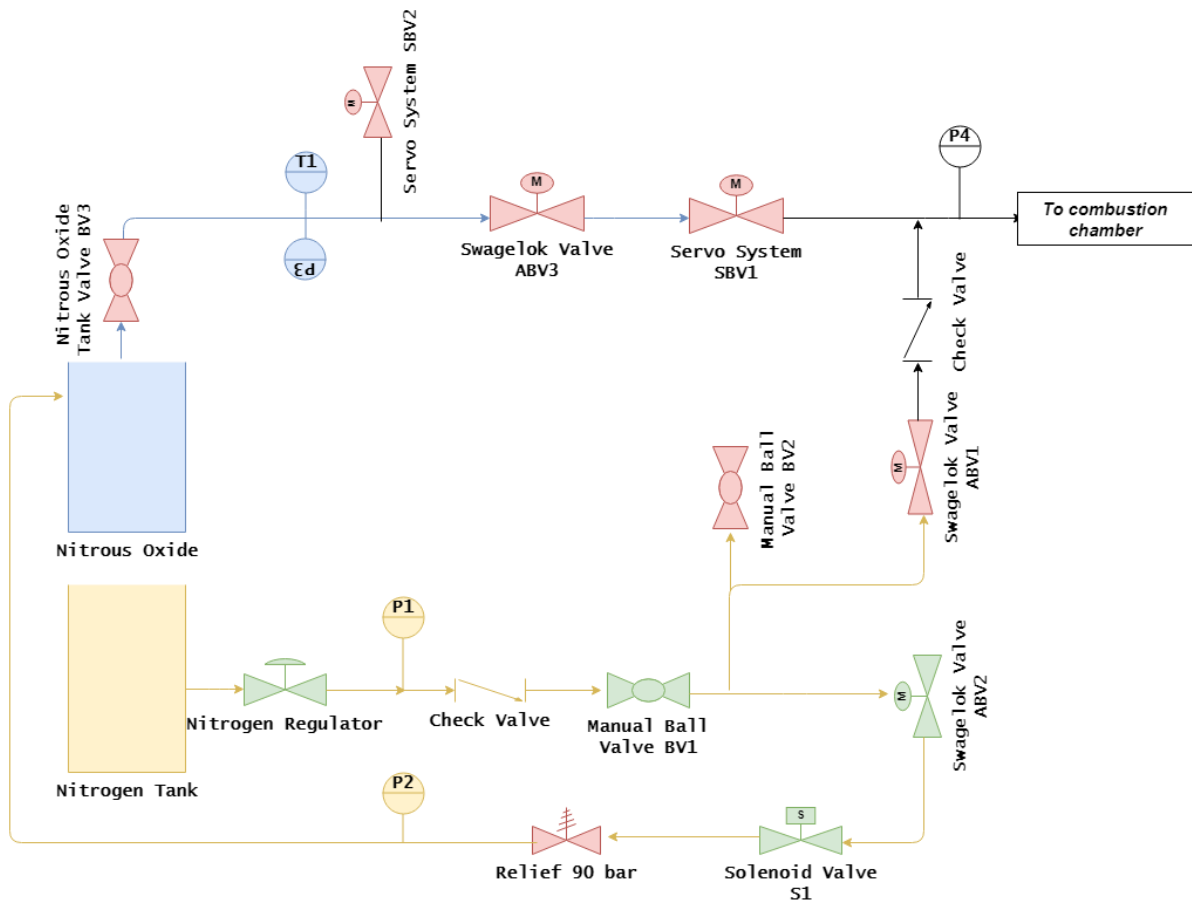


Figure 3.8: Supercharge process

After the nitrogen regulator was set to 65 bar, the LabVIEW front panel was used to verify that the pressure that was manually set was correct. Via the LabVIEW front panel, the valve ABV2 was opened. This allowed nitrogen flow to the solenoid valve which was then used to incrementally increase the nitrous oxide tank pressure to 65 bar. The 90 bar relief valve remained closed during normal operation and would only open in the event of an over-pressure in the propellant tank. The relief valve is spring-based and is reusable.

3.4. Purge system

Immediately after a hot fire test, the piping after the main oxidiser valve as well as the combustion chamber need to be purged with an inert gas. Purging removes hazardous nitrous oxide vapour that will be present in the system and rapidly cools the fuel grain so that it can be analysed later. Purging was done with the same gas that was used to supercharge the nitrous oxide tank. In this case, nitrogen.

In the LabVIEW system that was developed, the hot fire auto-sequence automatically purges the system directly after the oxidiser valves have been closed. The purge process can also be carried out manually via a radio button on the GUI front panel. In either case, the system will automatically close or open the necessary valves in order to route the flow of nitrogen to the main oxidiser feed line and combustion chamber. Figure 3.9 shows the configuration of the feed system while operating in purge mode. Again, green valves are valves that are in the open position and valves that are red are closed. The yellow lines indicate the presence of nitrogen gas, while the blue lines show the presence of nitrous oxide.

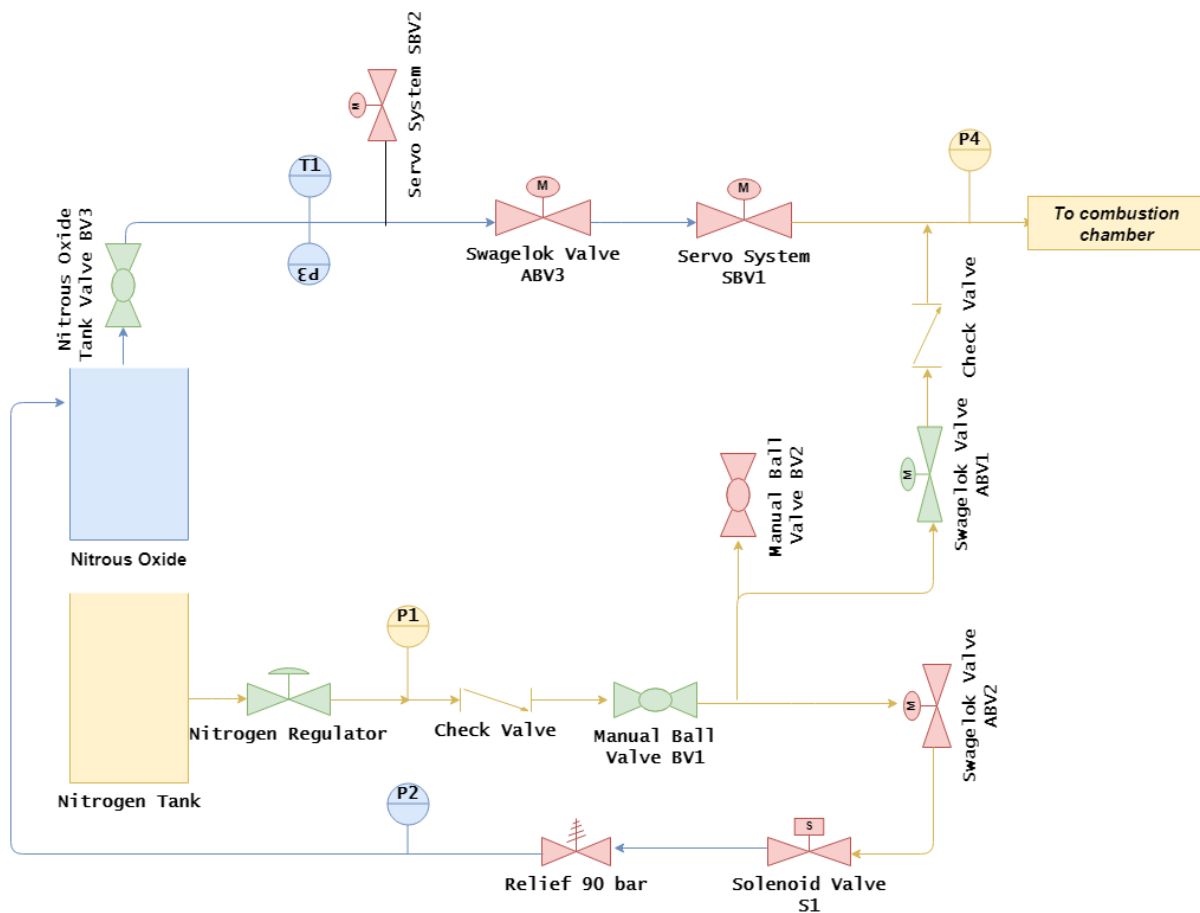


Figure 3.9: Purge mode schematic

Once the nitrogen leaves the nitrogen regulator, it passes through valves BV1 and ABV1 before being vented out through the combustion chamber.

and not an injection line, pressure drop is not a concern. Precise angular positioning is not a design requirement either, in this case.

3.6. Safety implementations

Due to the safety concerns around the use of nitrous oxide, various safety systems have been implemented at a mechanical and software level. This was to ensure that the systems performs repeatability without damaging any of the equipment, and that no persons are injured during any of the operations involving the feed system.

Firstly, the system was operated remotely at a safe distance. Where possible, automation was used to allow for remote operations. Secondly, all the equipment used on the feed system was cleaned in accordance with best-practice in cleaning liquid oxygen systems. All the instrumentation was cleaned in a three-step process starting with a dichloromethane rinse. This is an industrial solvent that is used for degreasing purposes. Next, propanol was used to rinse off the dichloromethane before being flushed with deionised water. Finally, the components were all dried with a purge of compressed nitrogen before installation. An image of the inside of the run tank is shown before and after the cleaning, for example, in Figure 3.11.

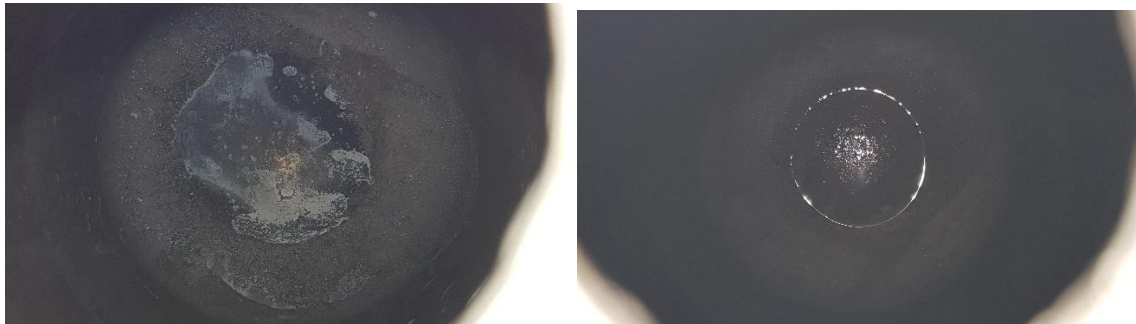


Figure 3.11: Run tank before cleaning (left) and after cleaning (right)

At a mechanical level, a relief valve has been integrated into the feed line. This valve will open when the propellant tank exceeds 90 bar and will reseal at 80 bar. There is also a relief integrated into the nitrous oxide tank valve itself. This was set by the manufacturer and will open at 2000 psi (137.9 bar). The relief valve on the feed line is shown in Figure 3.12



Figure 3.12: Relief valve

At a software level, Waterfall, the LabVIEW program that is discussed in section 4.4, constantly monitors parameters such as the pressures in the main feed and supercharge lines as well as the temperature of the liquid oxidiser via the thermocouple T1 as seen in Figure 3.1. If any of these parameters exceed a pre-defined value, the system will act based on what has been programmed. This will be discussed in further detail in Chapter 4.

4. Control and data acquisition system

The control and data acquisition system of the testing platform was primarily based on the National Instruments cDAQ platform. All the data acquisition as well as the actuation of the commercial ball valves and solenoid was implemented via the cDAQ system. The control of the servo ball valve and dump valve was achieved via an Arduino board. This approach was taken because the cDAQ chassis that was used is only capable of housing four modules. With all the slots occupied, there was no room for a fifth module to solely handle the servo ball valves. The cDAQ module that was needed was also expensive and more complex to program. The Arduino board was thus used as a cost-effective alternative and very simply interfaced with a hobby-type servo motor.

The two electronic sub-assemblies were unified with a LabVIEW program. The two platforms are controlled from the same user interface and appear to be one system from the point of view of the user.

4.1. National Instruments cDAQ

The cDAQ system was used as all the necessary modules and auxiliary hardware were already available for use. Figure 4.1 shows the unwired cDAQ chassis that was used, with all modules attached.

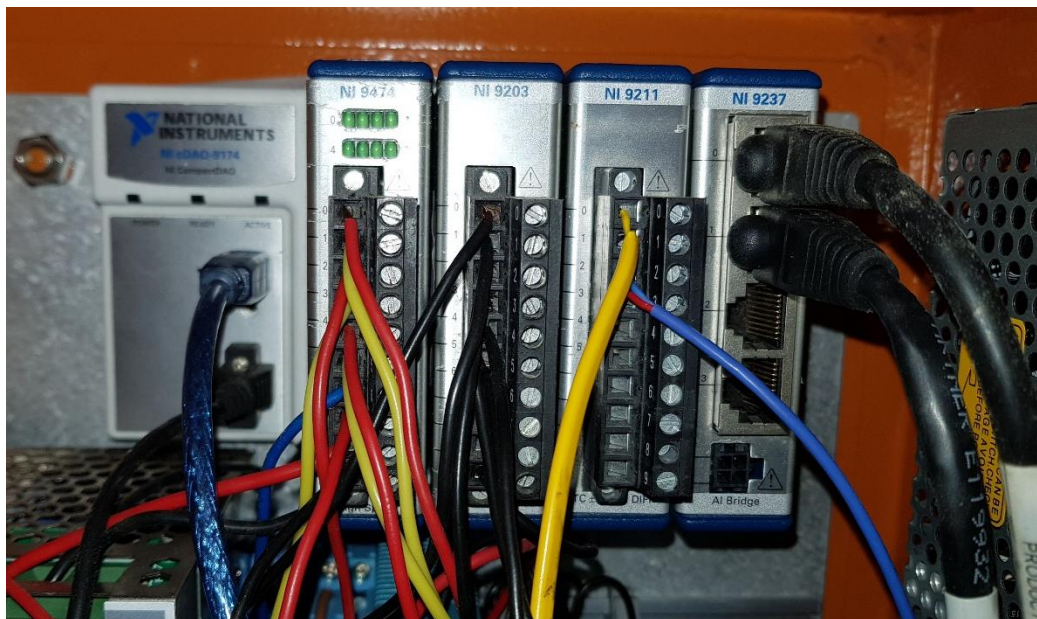


Figure 4.1: cDAQ chassis and module

The chassis that was used is the NI cDAQ 9174. It is a four-port chassis that communicates with the host computer via a USB 2.0 connection. As can be seen in Figure 4.1, the chassis was mounted onto a base plate which was the inserted into a DIN rail enclosure that protects it from liquids and dust.

4.1.1. Relay outputs (NI 9474)

In Figure 4.1, the first module on the left is the NI 9474 module. This module is designed for relay-based control and was used to control all the Swagelok ball valves, the solenoid valve, and the igniter. Referring to Figure 3.1, these include valves ABV1, ABV2, ABV3 and S1. The NI 9474 module has built in LED's which can be seen above the ports on the first module. These LED's are used for testing and troubleshooting of the programming without any equipment connected to the module.

The Swagelok valves each use two output channels on the NI 9474 module; one was used to open the valve, while the other was used to close it. The seventh channel was used for the solenoid valve which operates on 220 VAC. The solenoid channel was connected to a 24 V relay which places the solenoid in either an on or off state. The last channel on the module was used for the igniter. The channel connects to a 24 V relay which was placed in a series loop with a 12 V battery and the nichrome element that is used to initiate the igniter. Since the element had a relatively low resistance and thus a high current demand, it was powered by a battery instead of a 12 VDC power supply.

A wiring diagram of the electrical components described above connected to the 9474 module is shown in Figure 4.2.

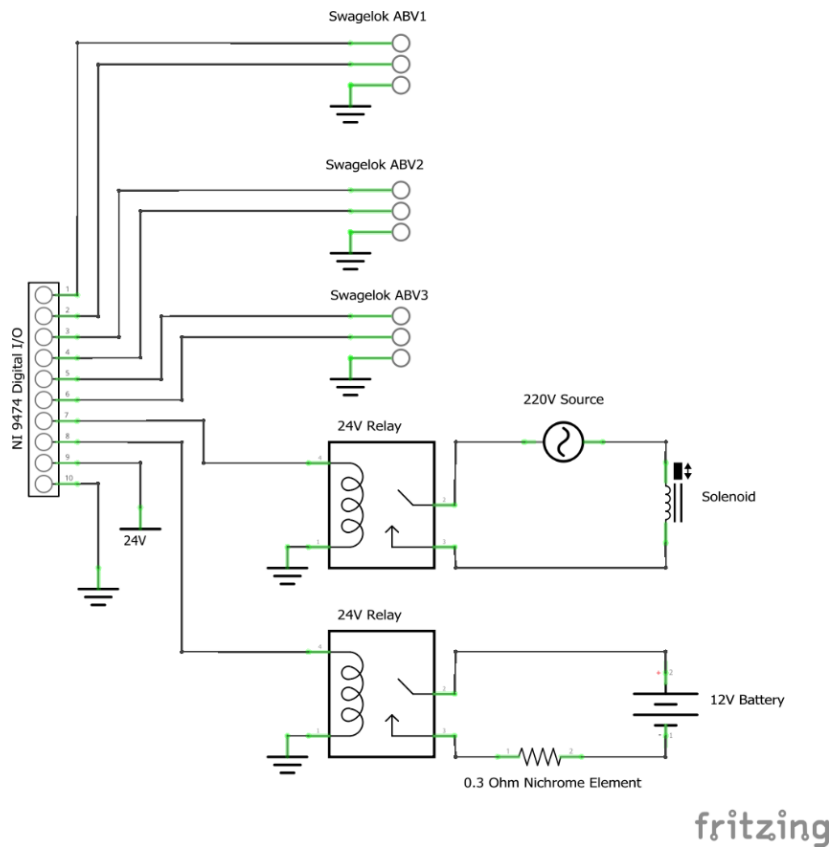


Figure 4.2: NI 9474 wiring diagram

4.1.2. Pressure measurements (NI 9203)

The second module is the NI 9203 which is a current loop receiver module. The module operates on the 4-20 mA instrumentation standard used by all six pressure transducers on the feed system. Four transducers are on the feed line measuring pressures at various points, and the other two are fixed to capillary tubes to monitor combustion chamber pressures. WIKA A10 pressure transducers were used in all instances. The transducers have a measuring range of 0-100 bar and linearly map this pressure input to a 4-20 mA signal, which is then captured by the NI 9203 module. The wiring for one such transducer is shown in the schematic contained in Figure 4.3 .

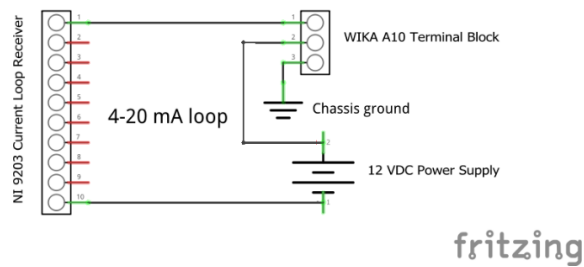


Figure 4.3: Pressure transducer current loop

4.1.3. Thermocouple measurements (NI 9211)

The third module is the NI 9211 which is used exclusively for thermocouples. Although three channels are available to be used, only two channels were used. One of the thermocouples, marked as T1, is a T-type thermocouple and measures the temperature of the liquid N₂O in the injection line. The second is a K-type sheathed thermocouple, and was inserted into the nozzle, above the throat region, to measure the nozzle temperature during hot firing.

Since the module was solely for thermocouples, the positive and negative leads of the thermocouple are simply connected to the corresponding screw terminals on the module.

4.1.4. Load cell measurements (NI 9237)

The last module shown on the right in Figure 4.1 is the NI 9237 module. This module is used for measurements made by strain gauges such as those used in load cells. The module allows for four channels in total, only two were used. On the testing platform, there are two load cells. One is a 250 kg cantilever-type load cell and was used to measure thrust. The other is a 50 kg S-type load cell that was used to measure the nitrous oxide mass flow rate via a continuous time derivative in LabVIEW and measurement of the mass of the tank that was housed in a custom-made scale seen in Figure 4.4. In this configuration, the load cell was operating in tension, and thus the signal leads were configured accordingly. This set-up in the testing area is shown in Figure 4.4.



Figure 4.4: Oxidiser tank mass measurement

A previous system based on the same concept was initially used, where the load cell from a commercial electronic scale was interfaced directly to the NI 9237 module. The problem that was encountered in this arrangement was that since the load cell was not shielded, the signal noise that was produced resulted in a measurement uncertainty of approximately 30 g/s.

The new system that is seen in Figure 4.4 resulted in an uncertainty in the region of 10 g/s, due to the use of a shield on the load cell cable as well as the load cell's built-in remote sense feature. The system in Figure 4.4 was the final implementation.

The NI 9237 module was connected to the load cells via an RJ50 cable that joined the module to a screw terminal block. This terminal block was in turn joined to the cables from the load cell. The module and terminal block had terminals for load cells that incorporate a shield and remote sense.

Since the NI 9237 module was used only for strain gauge measurement, the wiring was “plug and play” after the load cell cables were attached to the terminal block.

4.2. Arduino platform

As discussed at the start of chapter 4, an Arduino board was used to operate the servo valves on the injection line and dump line. The specific board that was used, was the Arduino UNO R3. The board was housed in the same DIN rail enclosure that houses the cDAQ hardware described in Section 4.1. The wiring of the Arduino board to the two servo motors on the custom-developed valve, and to the servo motor on the dump line, is shown in Figure 4.5.

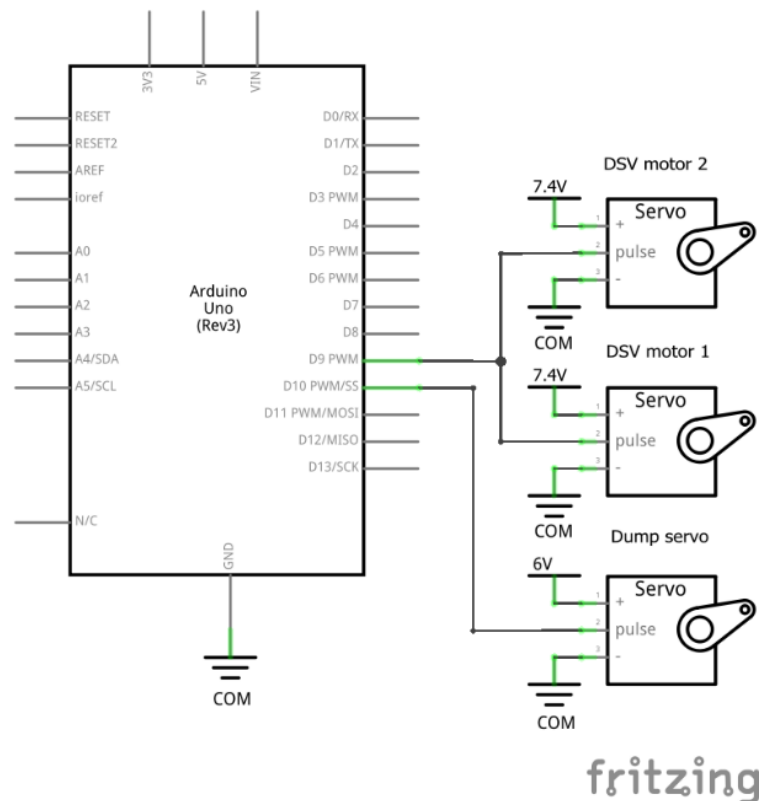


Figure 4.5: Arduino UNO R3 servo valve control board

Motors 1 and 2 on the custom-developed valve were connected to the same digital output pin (D9-PWM) on the Arduino board to ensure that the same signal was sent to both motors. In the LabVIEW program, a single signal was sent to pin 9 of the board. The servo motor for the dump line was connected to pin 10, which is also a pin that supports PWM.

The pair of motors for the custom-developed valve were powered by a 7.4 VDC power supply. This was recommended by the manufacturer to ensure that motors peak torque was produced. A 6 VDC power supply was used to power the servo for the dump line for the same reason. Both DC power

supplies, all three motors and the board were connected to a common ground for the system to operate at the same voltage reference.

4.3. Termination system

A termination system was developed to operate completely independently from the hardware described in Sections 4.1 and 4.2, and the LabVIEW program. The termination system was to be used in the event that the LabVIEW program or host computer became unresponsive for any reason, or in the event of a power failure.

At the centre of the system is an Arduino Nano microcontroller that was hardcoded. A program written in C on the Arduino IDE (integrated development environment) was uploaded to the on-board flash memory. This script was run independently and continuously. The microcontroller did not receive commands from the host computer as in the case of the Arduino UNO described in Section 4.2.

Once the termination button is pressed, control of the Swagelok ball valves and servo ball valves would be handed over to the hardcoded Arduino Nano board. The controller would then close off the oxidiser supply valves as well as any other valves that might be opened. The current system can also be configured, if need be, to close the oxidiser supply and vent out the contents of the run tank.

The wiring diagram of the termination system is shown in Figure 4.6.

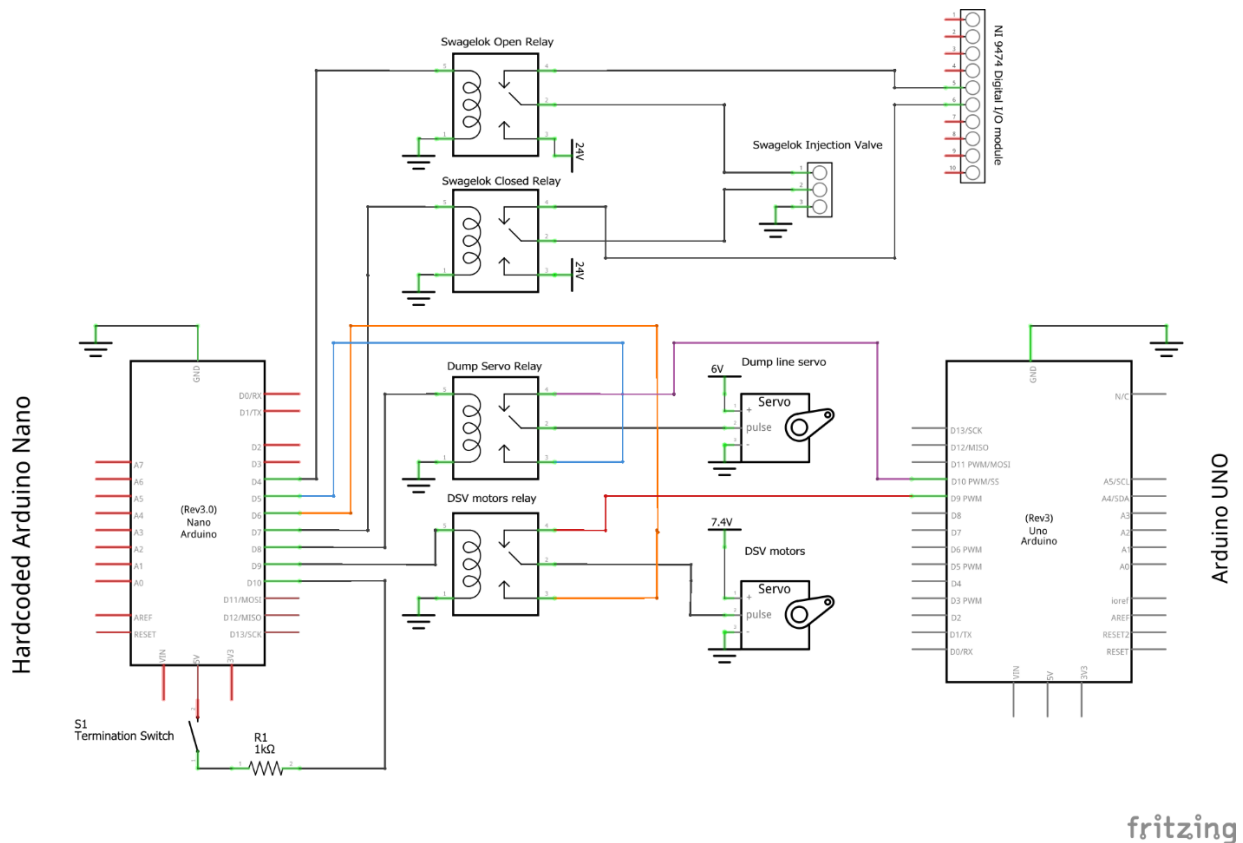


Figure 4.6: Termination system

While the termination button is pressed, commands relayed to the valves via the cDAQ system and LabVIEW would be ignored, as these are inputs that are connected to the valves via the NC (normally closed) terminal of the SPDT (single pole, double throw) relay. Pressing the termination button would switch all of the relays to accept commands from the NO (normally opened) terminal of the relay.

By connecting all of the DC power supplies to a UPS (uninterruptable power supply), the termination system would be able to function in case of a power failure, allowing the system to be safely shut down and secured.

4.4. LabVIEW development

To control all the hardware on the testing platform and acquire data from the testing procedures, a program was developed in the National Instruments LabVIEW development environment. The program, code-named Waterfall, was used to control both the NI cDAQ hardware and the Arduino system.

4.4.1. Control structure

It was required that the system's hardware be controlled in an auto-sequence during hot fire testing. In this auto-sequence, the user inputs parameters such as burn time, igniter timing, etc. By clicking a single button on the front panel, the code should be capable of sequentially starting up, running and shutting down the rocket motor.

Initially, the program needs to establish communication with both the cDAQ system and the Arduino board. Once the user has checked that the system temperatures and pressures are in order, the hot fire test parameters are set. By clicking on an auto-sequence button, the program starts the process by checking the actual propellant tank pressure and P1, the targeted supercharge pressure. The solenoid valve (S1) then opens and closes as required in order for the propellant tank to reach the target pressure, at which point, the supercharge process ends.

Once system temperatures are checked again, oxidiser flow is enabled by opening the valve ABV3. If all parameters are in their correct ranges, the igniter is activated, followed by a user-defined delay to allow for a small amount of paraffin wax to melt and vaporise. The SBV1 valve then opens to allow oxidiser to flow into the combustion chamber. The system then permits combustion within the motor for the specified burn time, while monitoring pressures and temperatures, following which the SBV1 and ABV3 oxidiser valves are closed. The purge valve ABV1 is then opened for a user-defined period of time in order to extinguish residual combustion within the combustion chamber. The auto-sequence is then complete. For planning purposes, this central control structure was developed in a flow chart, shown in Figure 4.7, which served as a skeleton to begin development of the LabVIEW program.

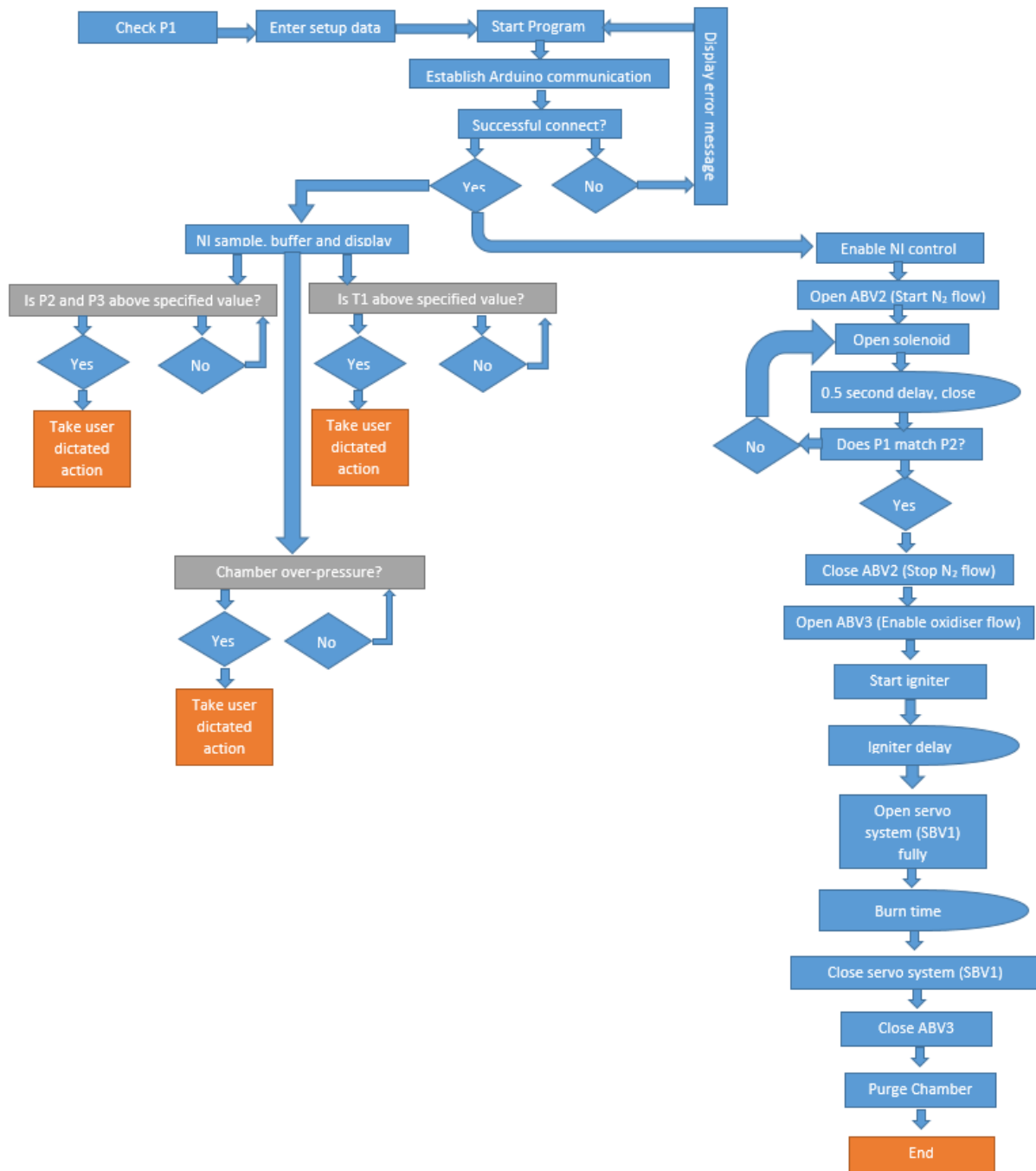


Figure 4.7: Auto-sequence control structure

There was however an initial step before the development of the core code, the configuration of a LabVIEW function block called DAQ assistant. This is where all the sensor hardware and equipment can be defined and configured. For the sensors, the type of measurement, signal output, output range and sensor mapping are all defined so that the correct reading can be displayed. For the control hardware (valves etc.), the NI 9474 modules channels can be configured to output a specific signal. Figure 4.8 shows a portion of the DAQ assistant window associated with the thrust-measuring load cell.

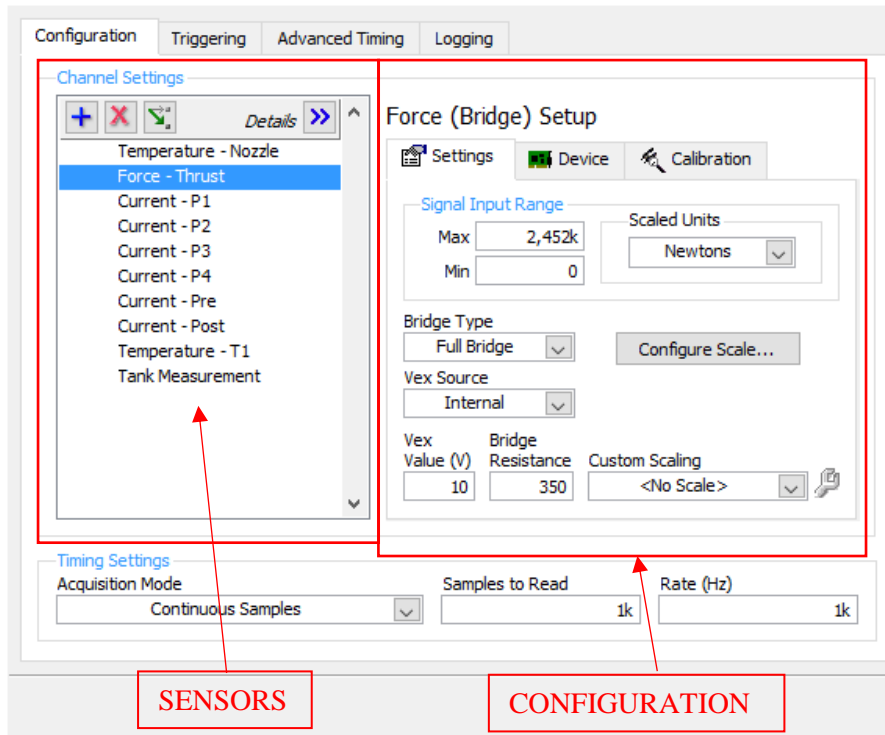


Figure 4.8: DAQ assistant window

The window in Figure 4.8 was used for the configuration of the sensor hardware. All of the output signals were derived from this function block.

Another DAQ assistant window was used for all the control hardware. The control function block receives inputs from the core code that dictates the operation of the hardware. This contrasts with the configuration window for the DAQ assistant function block in Figure 4.8 that is responsible for acquisition of signals from the sensor hardware.

4.4.2. Graphical code

Coding of the system began with the control structure in the above section. For safety reasons, it was decided that the auto-sequence be programmed to control the entire hot fire test, from the initiation of the igniter until the purging of the combustion chamber.

In Figure 4.9, the first four steps of the auto-sequence code are shown. The case structure was indexed starting from 0. The first frame (top, left) is for the countdown timer to begin the hot fire test auto-sequence. The second frame (index 1-top right) starts the igniter and turns on an igniter LED on the front panel before waiting for the required time. The wait is to allow for the igniter to burn and vaporise small amounts of paraffin wax before admitting oxidiser flow to the combustion chamber. Index 2

opens the servo oxidiser control valve to the fully opened position and turns on a “firing” LED on the front panel. The case then waits for the pre-determined burn time before moving to index 3. Index 3 closes the oxidiser valves and turns off the LED’s on the front panel that were previously switched on. The two cases that follow purge the combustion chamber and turn on an “auto-sequence complete” LED.

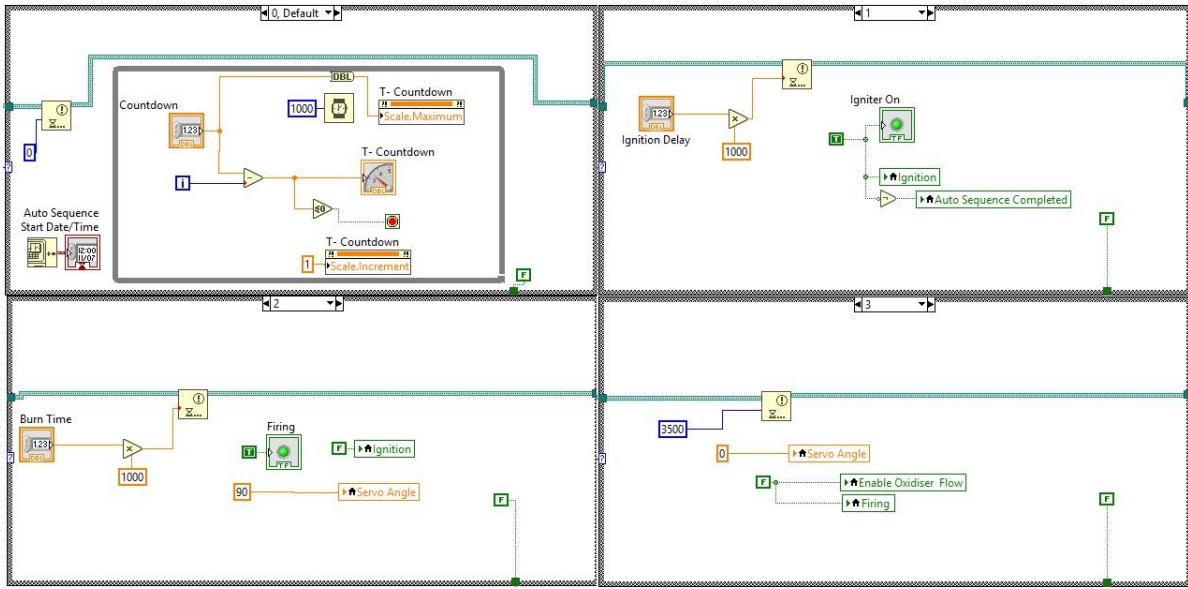


Figure 4.9: Auto-sequence code

While the auto-sequence is running, pressing the “TERMINATE” button on the front panel immediately stops the execution of code and returns the system to normal mode with all the valves in the closed position and the igniter relay disabled. While simple in principle, issuing a terminate command to stop the while-loop that runs all the cases in Figure 4.9, will not stop the auto-sequence immediately. Instead, such a command will only end the while-loop after all the cases in the case structure have been executed. To have the auto-sequence terminate immediately, a notification system in LabVIEW was used. The code for this is shown in Figure 4.10.

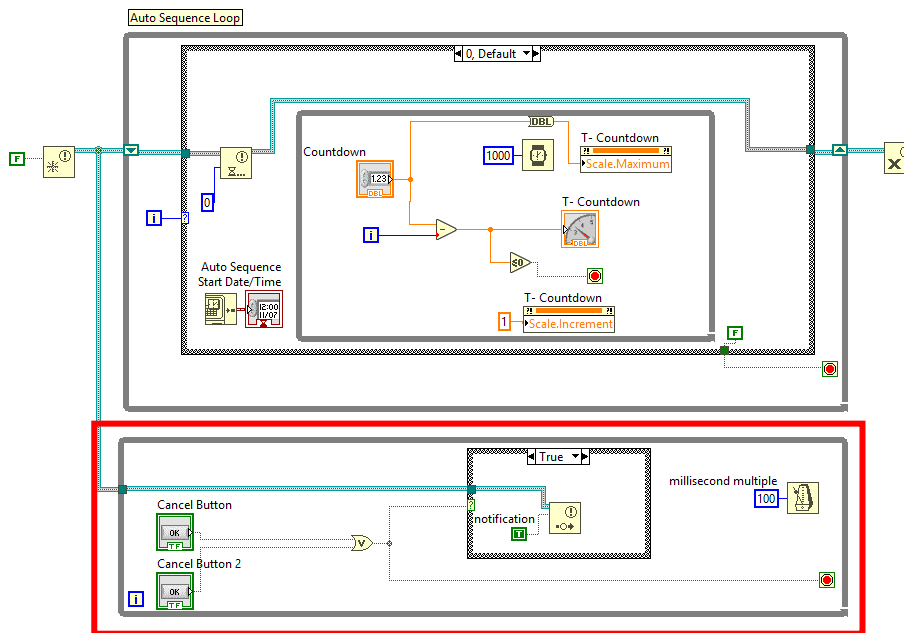


Figure 4.10: LabVIEW – Notifications

The notification loop (highlighted in red) runs in 100 milliseconds multiples and polls the state of the termination buttons on the front panel. If any of the termination buttons become true, the Boolean case structure in the bottom while-loop also becomes true and a notification is sent. The notification is indicated by the thick cyan line running from the while-loop at the bottom to the while-loop at the top. Once the loop at the top, which has the running auto-sequence, receives the notification, the auto-sequence loop terminates. Note that there are multiple termination buttons in the user interface. When using a monitor with a resolution of less than 1080p, it is not possible to display all the UI at the same time. The user will either be monitoring the real time data (Figure 4.17) or controlling the hardware (Figure 4.18). In either case, a termination button is available to allow the user to respond as fast as possible.

In Chapter 3, the various modes of operation were discussed in terms of the feed system instrumentation. The three operating modes, normal, purge and dump, are controlled by the Waterfall code. The operating modes were coded using a case structure that contains three structures. Figure 4.11 shows the LabVIEW code for the normal mode.

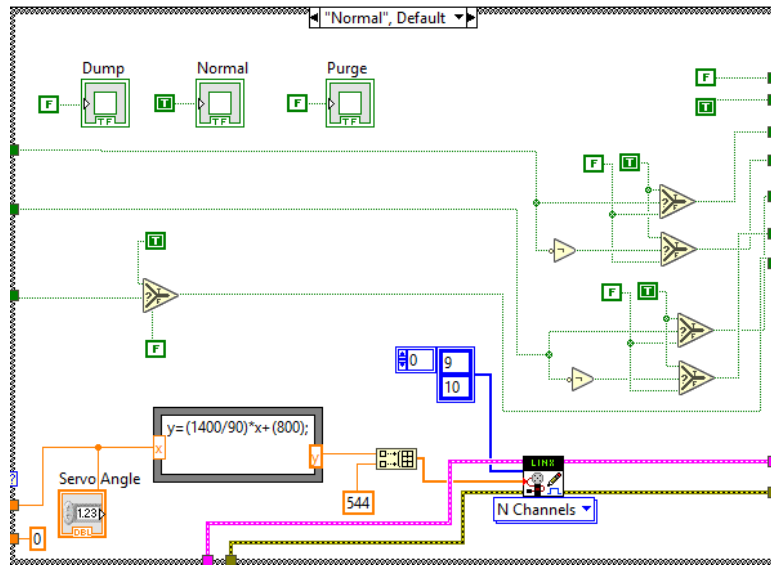


Figure 4.11: LabVIEW-Normal mode

In normal mode, the instructions to open and close valves are taken from switches on the front panel. These inputs enter the case structure shown on the left as loop tunnels (green squares). The loop tunnels leave the specific case on the right and are compiled into a Boolean array. The array of data is then passed to the DAQ assistant function for the control hardware. All the data paths shown by green lines are for controlling the Swagelok ball valves on the system. The orange lines in the bottom left are for controlling the Swagelok ball valves on the system. The function $y(x)$ in the bottom right of the case structure is to map an angle, $0-90^\circ$, to a pulse width which is sent to the Arduino board to move the respective motor to a prescribed angle. In normal mode, the servo motor for the dump line is closed and cannot be opened, for safety.

Purge mode allows the user of Waterfall to purge the combustion chamber by opening and closing the required valves as per Figure 3.9. For safety reasons, the user cannot use the manual buttons on the front panel to open and close valves while the system is in purge mode. The code for the purge case is shown in Figure 4.12.

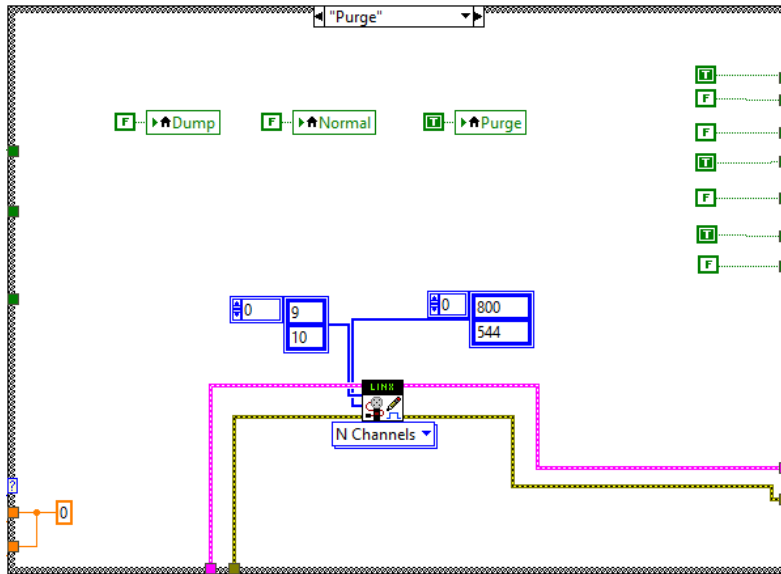


Figure 4.12: LabVIEW- Purge mode

The loop tunnels on the left of the image are still present but are unwired in the case structure itself. This is how the commands from the manual control buttons are ignored. Both servo motors are closed in purge mode. This is seen in the bottom right of the case structure in orange blocks. On the right hand side, the Boolean constants that are defined and sent to the Build Array function block (not shown) cannot change, irrespective of the state of the manual switches on the front panel. Note that the “800” and “544” in the blue blocks are pulse widths in microseconds that are sent to the Arduino board.

The last mode of operation is the dump mode, which empties the run tank by opening the dump valve and keeping all other valves closed. The code for dump mode is presented in Figure 4.13.

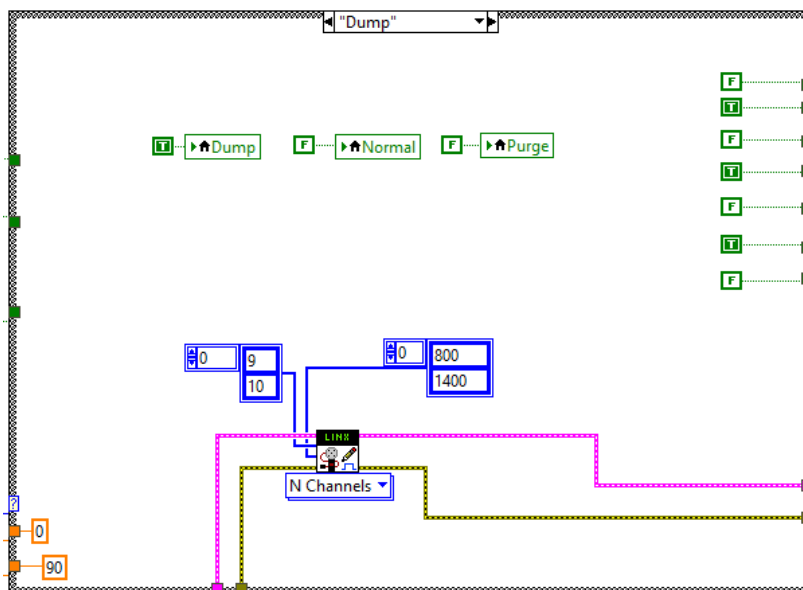


Figure 4.13: LabVIEW – Dump mode

As in the case with purge mode, commands from the front panel with the manual control buttons are ignored. The states of all the valves in the system are defined as constants. In terms of the servo motors, the custom-developed valve is closed (0 degrees) and the dump valve is opened fully (90 degrees).

In a separate while-loop, the system monitors the feed line temperature, T1, the nitrous oxide inlet pressure, P2, and the combustion chamber pressure every 50 ms. In the front panel, the user defines a safety threshold for each of these values. Typical values that were applied during testing are 40°C for the feed line temperature safety, 80 bar for P2, and 90 bar for the combustion chamber pressure. If any of the thresholds are exceeded, the system will display a message box to the user and take action that can be pre-programmed. For illustration purposes, two of these message box event handlers are shown in Figure 4.14.

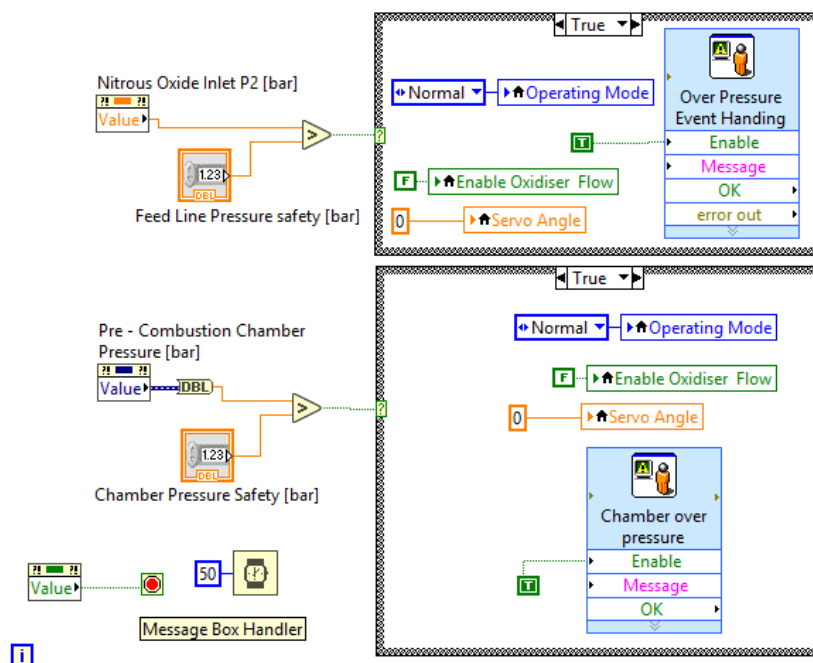


Figure 4.14: Message box handling

There is also a message box handler that notifies the user if an attempt is made to enable the oxidiser flow and activate an auto-sequence without the data logging being active. When the message box is displayed, pressing “Cancel” clears the notification and results in no action being taken. Pressing “OK” clears the message and enables data logging for the sensor and control systems.

As shown in Figure 4.4, the oxidiser tank mass is measured by an S-type load cell. This data is acquired by the DAQ assistant function block and is then sent to a signal conditioning function block to attenuate noise. The signal is then passed to a calculus function block that performs a continuous time derivative. In this way, the mass flow rate of the oxidiser is determined. Figure 4.15 shows this section of code.

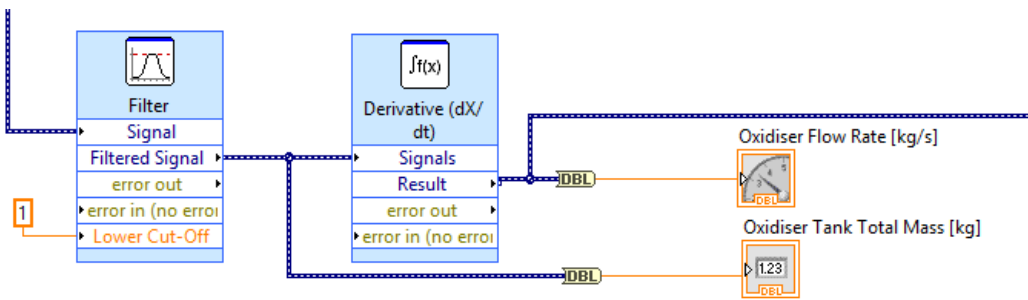


Figure 4.15: Propellant tank mass, signal conditioning

The blue line entering from the left in this image is from the DAQ assistant, while the blue line leaving on the right goes to a data logging function that records all of the data. The following figure shows the configuration of the filter function block, which was set as a low pass filter.

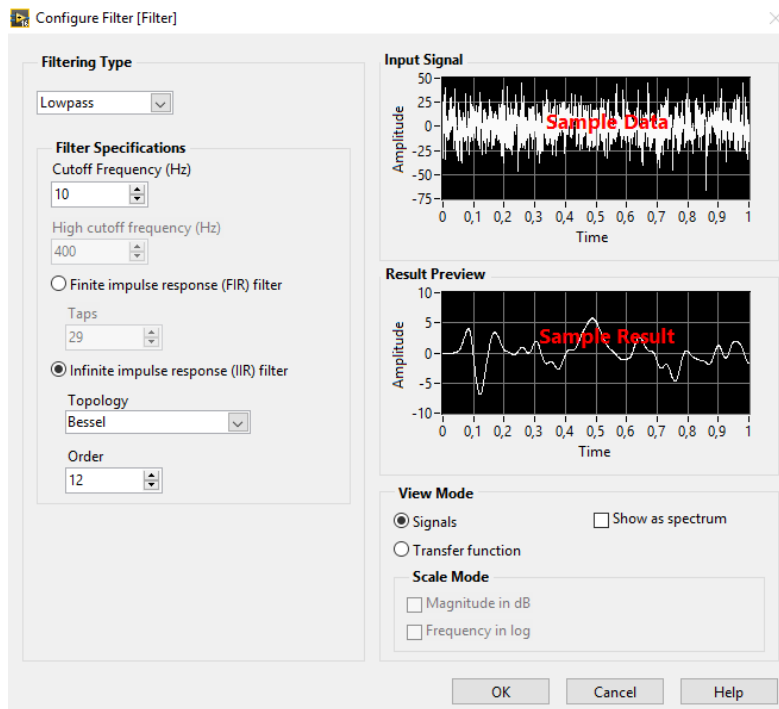


Figure 4.16: Filter configuration

A short LabVIEW program was written for setting parameters such as the cut-off frequency and polynomial order as variables that can be adjusted with knobs. A suitable polynomial order and cut-off

frequency where then determined experimentally by assuming values based on a fast Fourier transform of the unfiltered signal and making the necessary adjustments with the knobs on the front panel.

4.4.3. Graphical user interface (GUI)

The front panel for all of the graphical code in the section above was created in a tabbed configuration due to the amount of data that is presented or required as an input. The first tab is a setup tab in which the user specifies the COM port to which the Arduino board discussed in Section 4.2 was designated by Windows. The set-up tab also requests the safety thresholds that are required by the safety monitoring while loop shown in Figure 4.14.

The second tab is the main tab, where all of the virtual instrumentation and control is placed. It is divided into two sections, the instrumentation on the left and the control on the right. A screenshot of the instrumentation panel is displayed in Figure 4.17.

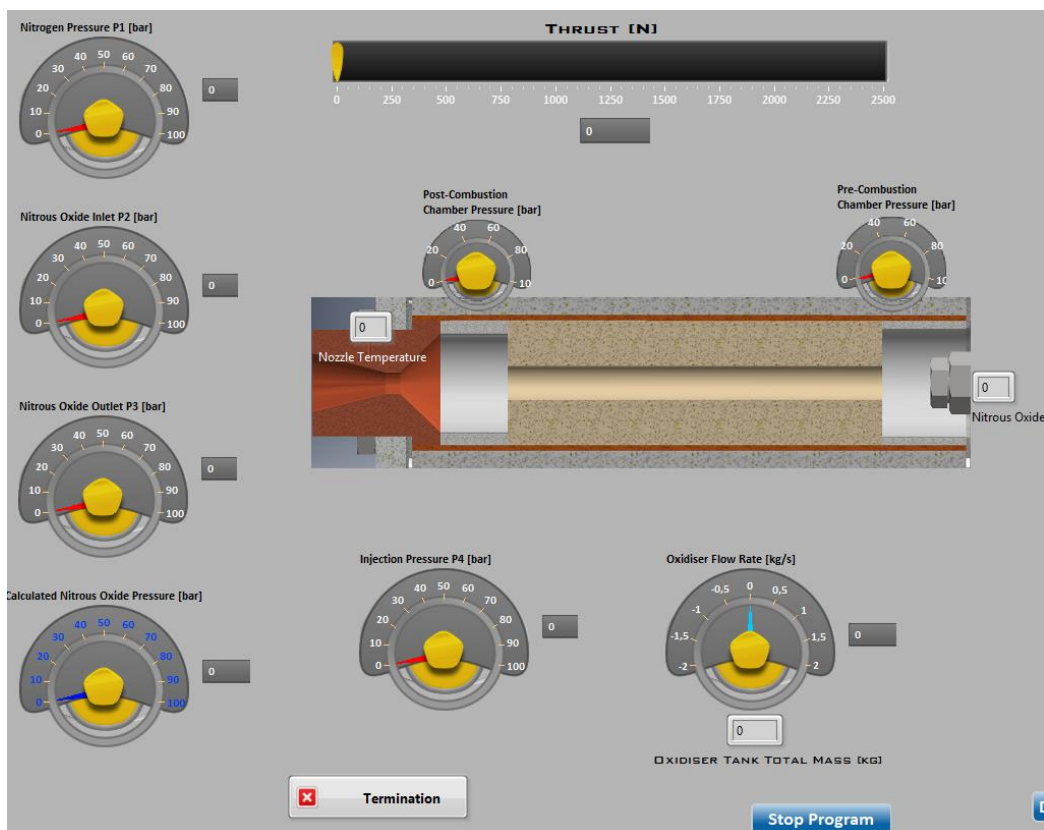


Figure 4.17 Virtual instrument panel

System pressures in the feed line are shown on the left, and pressure upstream of the injector is shown as P4, below the graphic of the nozzle. The pressures in the pre- and post-combustion chambers are indicated by smaller pressure gauges above the chambers. Motor thrust is indicated by a bar indicator above the gauges. To the right of the graphic of the injector, the thermocouple T1 shows the nitrous oxide temperature in the feed line. The nozzle temperature measurement is shown by the digital at the top of the nozzle graphic. The oxidiser flow rate gauge shows the filtered output of the time derivative from the load cell measuring the run tank mass.

The control panel is further divided into manual control, auto-sequence control, and operating mode. The manual control section is shown in Figure 4.18.

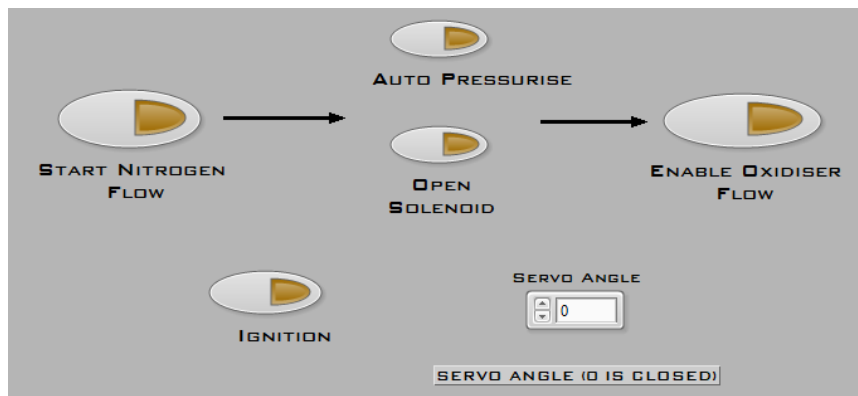


Figure 4.18: Manual control

The manual control section is provided for troubleshooting purposes, as well as for the testing of all the valves and relays before a hot fire or cold flow test. “Start Nitrogen Flow” opens valve ABV2, “Open Solenoid” opens valve S1. The “Auto Pressurise” button automatically supercharges the run tank and maintains the set point pressure that was inputted into the configuration tab. “Enable oxidiser flow” opens the ball valve ABV3. Every hot fire test begins when the “Start Nitrogen Flow” valve is opened. Once no leaks are confirmed, the propellant tank is pressurised by using either the “Open Solenoid” button or the “Auto-Pressurise” button. After pressurisation, oxidiser flow to the combustion chamber is enabled by pressing “Enable Oxidiser Flow”. It is only after these three steps that the auto-sequence is used.

The auto-sequence is the third section of the user interface in the second tab. An image this portion of the front panel is displayed in Figure 4.19.

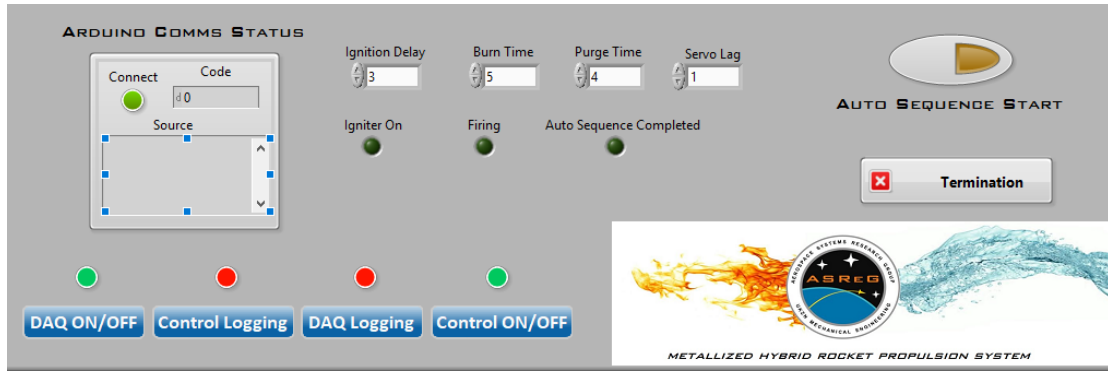


Figure 4.19: Auto-sequence

The four numeric control boxes enable the entry of auto-sequence parameters. Once the “Enable Oxidiser Flow” valve has been opened and the parameters are verified. Clicking on “Auto-Sequence Start” will run the hot fire test from the initiation of the igniter to the end of the combustion chamber purge. The “Termination” button will call the notification loop in Figure 4.10. The “Arduino Comms Status” section shows the status of communication with the Arduino system via an LED, while a source box shows errors in the communication, if any. The “DAQ ON/OFF” and “Control ON/OFF” buttons stay in the ON position by default but can be switched off in the event that the user wants to isolate either of the systems for troubleshooting. The “Control Logging” and “DAQ Logging” buttons are normally switched on before enabling oxidiser flow. If not, a message box will appear and prompt the user to turn the data logging on before proceeding to the auto-sequence. The three LED’s below the auto-sequence parameter fields show the progress of the hot fire test.

The operating mode box is the final section in the second tab of the user interface and can be seen in Figure 4.20.

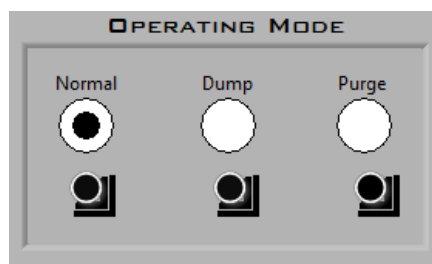


Figure 4.20: Operating mode selector

In an emergency scenario, modes such as those for dumping the liquid propellant or purging the chamber are too complex to select immediately by closing and opening a series of valves. The operating

mode selector ensures that there is no delay in reacting to an emergency that is not monitored by LabVIEW and that requires the user's intervention. Pressing one of these radio buttons moves the feed system to a pre-programmed state by simultaneously opening and closing associated valves.

The final tab in the LabVIEW front panel is the charting tab. In this tab, all of the data in Figure 4.17 is charted in real time. A screenshot of the tab is shown in Figure 4.21.

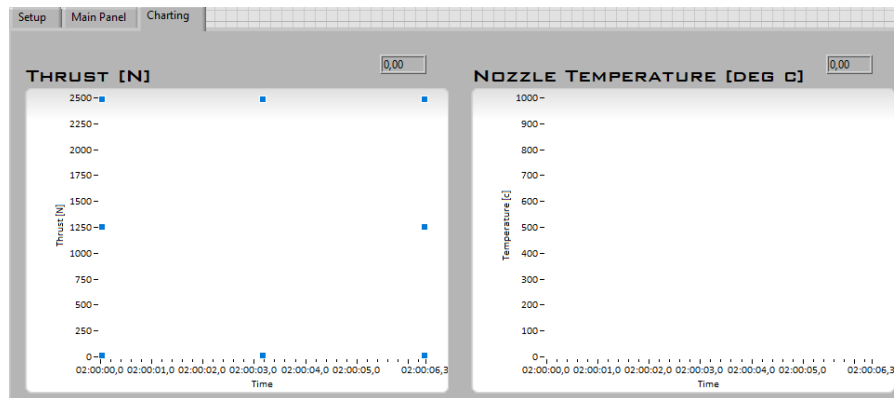


Figure 4.21: Real time charting

If required, the parameters of a given test can be monitored in real time with history rather than viewing the instantaneous values on the virtual instrument panel. They can also be toggled while a test is running.

5. Theoretical motor performance

In the literature review, three additives that are used in the propulsion industry were discussed. They are: aluminium, magnesium, and lithium aluminium hydride. For the purposes of this project, only aluminium was tested as a metal additive. As seen in Table 1.1, aluminium offers the highest enthalpy of formation based on its oxidation. Compared to other additives such as magnesium and lithium aluminium hydride, aluminium is non-volatile and relatively easy to handle. Due to the volatility of LiAlH_4 in the presence of moisture, it was eliminated as an option as no special equipment to store and utilise the chemical was available for use.

As a cost comparison, aluminium powder can be purchased in South Africa for R26.00 per kilogram while magnesium powder (only available as an analytical reagent) is R904.00 per kilogram. The difference is largely due to the fact that the aluminium powder that is available is mass produced for the use in metallic paints, whereas the magnesium is produced in smaller quantities for laboratory use.

The aluminium powder used for this study was not held in an inert environment, resulting in particles that have already developed a layer of aluminium oxide. The aluminium powder was put under a microscope to determine the average particle size and shape.

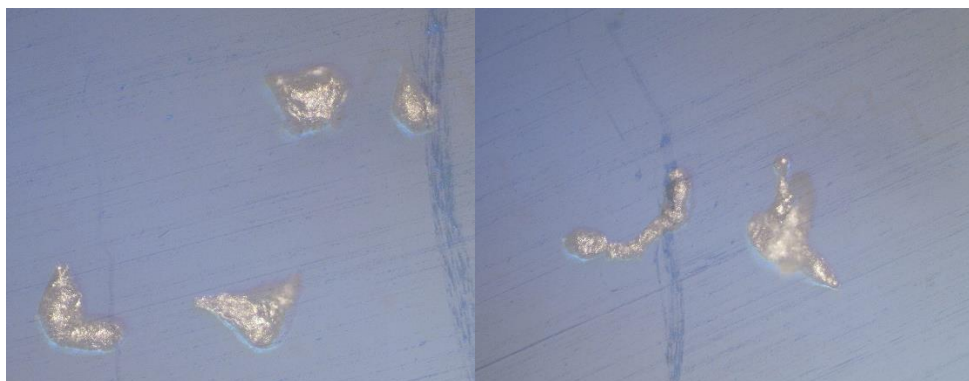


Figure 5.1: Aluminium powder under magnification

As can be seen, both particle size and shape are erratic, with some of the particles elongated and others closer to a spherical shape. The average particle size was calculated to be in the order of 75 μm .

Once the decision to use only aluminium powder was made, the theoretical performance of the additive in varying mass percentages was investigated. NASA CEA used to examine thermochemical and rocket performance parameters.

There are various performance metrics that are used to characterise the performance of rocket engines. Specific impulse for example, is a measure of propellant efficiency in terms of the thrust that can be obtained per unit of oxidiser flow. Since it is dependent on the thrust, it is then dependent on the nozzle geometry. This project aimed to solely characterise the performance of the propellants that are being used, more specifically, the additive added to the solid propellant. Rather than specific impulse, a more appropriate measure of performance will be the characteristic velocity which is a measure of the thermochemical merits of the combustion process. It is referred to as “c-star” (c^*).

A theoretical analysis was performed with NASA CEA in order to investigate the performance of aluminium powder in paraffin wax at mass percentages of 10%, 20% and 40%. The analysis was done by assuming a frozen analysis which treats the composition of the combustion products as constant while moving through the nozzle. The alternative is an equilibrium analysis which recalculates the composition at the combustor end, throat and exit. While the latter may be more accurate, the results did not converge for aluminium percentages exceeding 20% using an equilibrium analysis.

A sample of the CEA script that was used as an input is shown in Appendix B. For the analysis, a chamber pressure of 40 bar and a total temperature of 2000 K were assumed. The output of CEA was then plotted against various oxidiser to fuel ratios (O/F). The following graph shows the characteristic velocity plotted against different O/F ratios for both pure and aluminised paraffin wax.

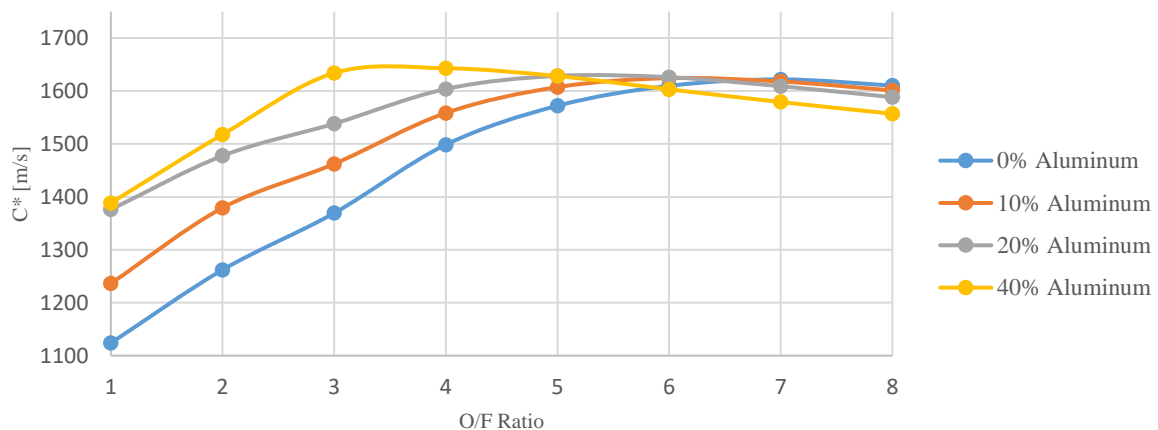


Figure 5.2: Characteristic velocity vs. O/F ratio

A fuel grain with 40% aluminium powder by mass shows a theoretical, optimal O/F ratio of approximately 3.4. A grain with 0% aluminium powder (pure paraffin wax) has an optimal ratio O/F ratio of approximately 7. Other than the slight increase in the characteristic velocity, the largest advantage is the approximate halving of the optimal O/F ratio for a 40% aluminised fuel grain. Figure

5.2 also shows that the curve flattens out as the percentage aluminium loading is increased implying that a flatter thrust curve can be achieved. Practically, in terms of thrust, this means that there is less dependence on the O/F ratio that the propellants are burning at. Theoretically, a 40% aluminised fuel grain could produce a more constant thrust curve while firing.

The input to NASA CEA in the aluminium cases assumes that there is no aluminium oxide in the fuel grain. This is not the case in reality and is an assumption that will greatly affect real performance data. The aluminium oxide layer is impervious to oxygen and must be melted off or damaged for the oxidiser in the combustion chamber to oxidise the particles. The heat absorbed by the particles and transit time required to do this was not calculated in the above analysis.

Using the regression rate data in Section 1.6.1, a regression simulator was developed using the LABView development environment. The simulator plots charts of regression rate and oxidiser mass flux. It also calculated the time averaged regression rate. Since the laboratory set-up has no regression rate sensors to measure real time regression rate, the time-averaged regression rate is the best metric that is available to experimentally compare the regression of an aluminised grain to a non-aluminised grain. The data in Figure 5.3 were produced by LABView and plotted in Excel.

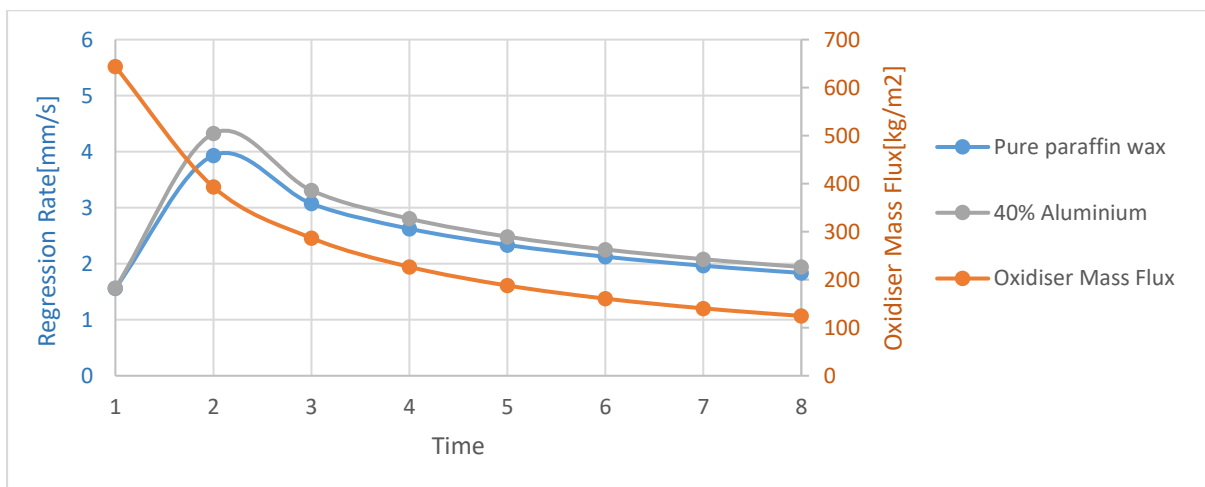


Figure 5.3: Regression rate simulation – Pure and aluminised paraffin wax

For the 40% aluminium and pure paraffin wax grains, the oxidiser mass flux is the same in each case as it is dependent on the oxidiser mass flow rate and port geometry. Over an eight second burn duration, the time-averaged regression rate for the pure wax case was calculated to be 2.28 mm/s, and 2.51 mm/s for an aluminised fuel grain.

6. Igniter development

Hybrid rocket motors are typically ignited by a small pyrotechnic charge that is placed within the pre-combustion chamber with the flame end facing the solid fuel. The purpose of this charge is to vaporise a small amount of the solid propellant before the oxidiser flow is opened. In this way, at the time of oxidiser flow, a small amount of fuel and a flame are available to start the combustion process.

In South Africa, the manufacture and storage of pyrotechnic devices is governed by the South African Explosives Act, 1995 (Government of the Republic of South Africa, 2003). At the start of the project, a pyrotechnic licence had not been obtained warranting the experimentation with other non-pyrotechnic methods such as steel wool (discussed in section 6.1). After several failed attempts with these methods, a licence was obtained by the department and this is discussed in section 6.2 and 6.3.

In all cases, the electric circuit that drives the igniter was powered by a 12V battery and is described in section 4.1.1.

6.1. Steel wool – Iron combustion

Since the use of pyrotechnic devices was prohibited at the early stages of the project, the use of combusting steel wool as an igniter was investigated. Fine steel wool was pasted into the pre-combustion chamber which was connected to two copper wires wrapped around the steel wool at either end. In the LabVIEW program that was developed in section 4.4, the igniter was started by pressing the ignition button in the user interface and powered for several seconds. The custom-developed valve was then opened to an intermediate position that allowed a small amount of nitrous oxide into the chamber to rapidly oxidise the steel wool. Thereafter, the custom valve was fully opened.

To evaluate the characteristics of such an igniter, an initial test was done outside the combustion chamber to investigate the burning of steel wool when exposed to high electrical current. An image from the test is shown in Figure 6.1.

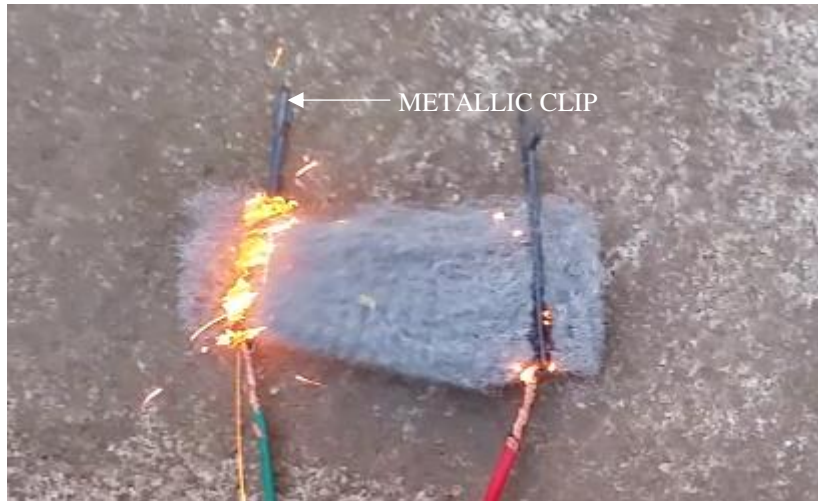


Figure 6.1: Steel wool test 1

The two metal clips were used to increase the electrical contact area with the steel wool. The steel wool was inserted into the metal clips and the battery leads were then connected to the clips. Figure 6.1 shows that the steel wool only burns in the region of the clips as the metal that has been oxidised acts as an electrical insulator, breaking the circuit.

In order to distribute the contact area, the copper strands of the battery leads were then randomly pushed into the steel wool in various directions. A picture from the second test is shown in Figure 6.2.

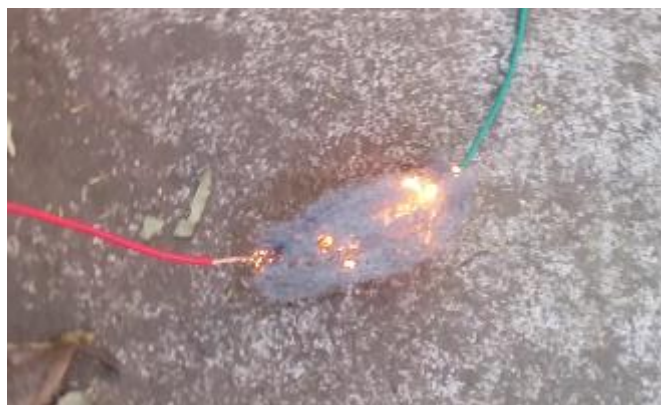


Figure 6.2: Steel wool test 2

In this case the contact area was more distributed compared to the previous test. However, the same problem was encountered where the steel wool only burned where it was in contact with the copper and quickly extinguished itself as the available conduction paths diminished.

An attempt was made to perform a hot fire test using steel wool as an igniter. Figure 6.3 shows the steel wool pasted into the pre-combustion chamber before a hot fire test.



Figure 6.3: Steel wool test 3

A small igniter delay was set in the Waterfall program, this was to ensure that the steel wool did not self-extinguish before the flow of nitrous oxide. The custom-developed valve was set to move to an intermediate position of 30° to allow for the throttled down flow of nitrous oxide to combust the steel wool before the valve was moved to the full flow position of 90° . The test that followed was a failed attempt, as the termination button was pressed in the LabVIEW program after the live stream camera feed showed oxidiser flow and no flame. Another attempt was made with steel wool with a smaller delay between the activation of the igniter relay and flow of nitrous oxide. Figure 6.4 shows three camera frames from the test.



Figure 6.4: Steel wool test 4

The burning strands of steel wool are seen being ejected from the combustion chamber when the custom-developed valve was moved to an intermediate position (00m: 00s). Two seconds later, it appears that the motor has not ignited, and nitrous oxide flow was seen as the custom valve moves into the fully opened position. A further two seconds later, the rocket motor ignites. This specific timing creates a dangerous scenario as the nitrous oxide occupying the combustion chamber has the potential to explosively decompose.

During this test, a bug in the LabVIEW program prevented the data from being logged and saved. The pressure at the ignition point was therefore not known.

Due to the unpredictable nature and non-repeatability of this type of igniter, steel wool was not used again, and a pyrotechnic licence was obtained by a staff member of the Aerospace Systems Research Group with the help of the South African Police Service (SAPS).

6.2. Match heads – Phosphorus trisulphide, potassium chlorate

Special safety matches marketed under the name “Strikers” are available in South Africa. These matches are normally used as fire starters for outdoor cooking. The match heads measure 1 cm by 0.5 cm on average, making them significantly larger than standard matches that are normally used. Modern matches use phosphorus trisulphide and potassium chlorate as the fuel and oxidiser respectively (Corbridge, 1990).

With this igniter system, five to six match heads were pasted around the circumference of the pre-combustion chamber. One of the match heads was wrapped in bridge wire that was connected to the igniter leads. In this case, the bridge wire was a strand of copper from 24-gauge copper cable. When 12 V was applied across the bridge wire, it heated up rapidly and lit the match head. The bridge wire and match head are collectively known as an e-match or electric-match. Figure 6.5 shows the electric match starting in a test that was performed outside of the combustion chamber.



Figure 6.5: Match heads proof of concept

Once alight, the e-match then ignites the other match heads due to its proximity, and the overall match head burn lasts for 6 s. Test numbers LH-001 to LH-003 (discussed in Chapter 9) used this type of igniter. LH-002 was a failed attempt with a 40% by mass aluminised fuel grain. Although the system worked for the two other pure paraffin wax tests, the aluminised test did not. Although it has not been verified and was a once off occurrence, it is thought that the increased conductivity of the fuel grain did not allow for a sufficient amount of paraffin wax to be vaporised before the start of the oxidiser flow.

6.3. Pyrotechnic made igniter- Sucrose, potassium nitrate

The last igniter configuration that was explored was the use of a cartridge containing a mixture of sucrose and potassium nitrate.

Within the scope of the pyrotechnic licence that was issued, pyrotechnic mixtures were prepared in a 40%/60% ratio by mass of sucrose and potassium nitrate, respectively. The mixture was then packed into a paper cylinder measuring 15 mm in diameter and 25 mm in length.

The mixture was started by a length of nichrome wire that was soldered to the igniter leads. The nichrome was then placed in the mixture and taped securely. Hot glue kept the leads fixed to the paper cylinder and prevented it from pulling on the nichrome wire. Figure 6.6 shows the igniter burning in a test outside the chamber.



Figure 6.6: Pyrotechnic igniter

These igniters were used for all of the tests that followed LH-003 in section 8.2. The igniters had a 100% success rate and provided a repeatable and reliable way of conducting hot fire tests.

7. Cold flow testing

Before hot fire testing, cold flow testing of the systems feed lines and injector was done in order to check the operation of all the valves in the system, determine pressure drop through the injection line and compare it with theoretical calculations and verify the injector design in terms of mass flow rate. Cold flow testing also provided an opportunity to test the operation of all the systems automation and check for leaks, particularly in the lower temperature ranges that cannot be replicated by the pressure tests that were done during the development of the system.

7.1. Injection line losses

To calculate the theoretical pressure drop through the injection line portion of the feed system, the pressure drop of the individual components was summed. The calculation included all of the instrumentation starting from the run tank (P2) to the pressure transducer for the upstream injector pressure (P4). This is illustrated in Figure 7.1.

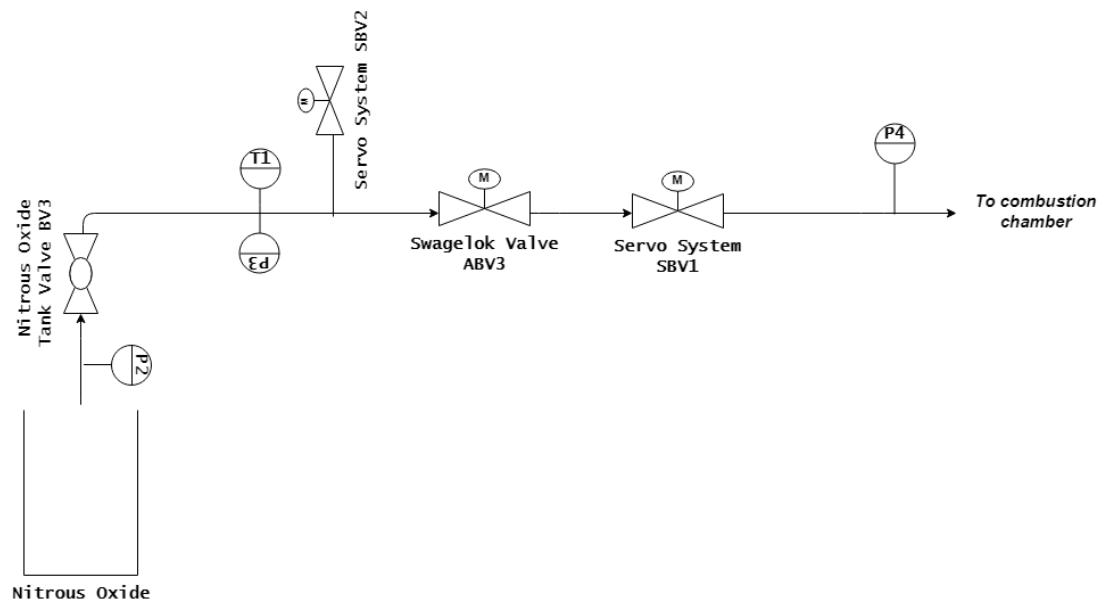


Figure 7.1: Illustration of included instrumentation for pressure drop calculation

The following table shows some of the data that was used in the computation, for a flow rate of 0.5 kg/s.

The flow coefficient used in The constants 5.8 and 500 in equation 2.19 to are enable the use of metric units in the equation. The C_v value that is quoted by manufacturers is in imperial units. In equation 2.19, \dot{m}_{ox} is the mass flow rate of oxidiser in kg/hr, SG is the specific gravity of the working fluid and ΔP is the pressure drop across the valve in kPa.

Table 7.1 is defined in equation 2.19. It is determined experimentally by manufacturers and is a measure of a process valves efficiency in terms of the mass of working fluid that can be transmitted at a given pressure drop (Fisher Controls International, 2001).

$$C_v = \frac{5.8 \dot{m}_{ox}}{500 (SG \cdot \Delta P)^{\frac{1}{2}}} \quad (2.19)$$

The constants 5.8 and 500 in equation 2.19 to are enable the use of metric units in the equation. The C_v value that is quoted by manufacturers is in imperial units. In equation 2.19, \dot{m}_{ox} is the mass flow rate of oxidiser in kg/hr, SG is the specific gravity of the working fluid and ΔP is the pressure drop across the valve in kPa.

Table 7.1: Pressure drop calculation data

Description	Flow coefficient C_v	Darcy friction factor	Pressure drop (bar)
½” SS syphon tube	N/A	0.0289	0.205
½” SS tubing	N/A	0.0289	0.768
½” PTFE braided hose	N/A	0.0114	0.308
½” Swagelok 63 series valve	7.5	N/A	0.104
½” Swagelok 45 series valve	12	N/A	0.041
2x T-piece sections	N/A		0.303

The sum of the pressure drops from P3 to P4 are shown in the greyed cells above and amount to 0.913 bar. This shows the pressure drop through the entire injection line, from the point of nitrous oxide entry (P3) to upstream of the injector (P4).

During cold flow testing, the run tank was blown-down, and data was recorded. The pressure histories from transducers P3 and P4 are shown in Figure 7.1.

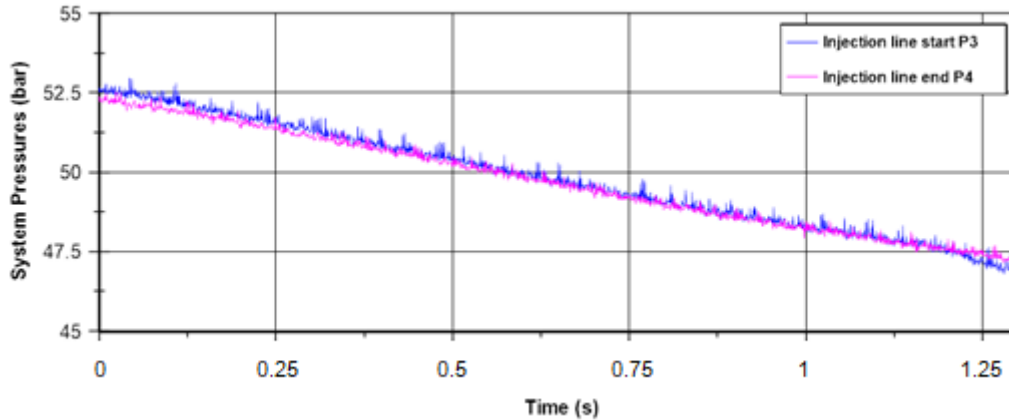


Figure 7.2: Pressures P3 and P4 during cold flow testing

The experimental drop in pressure was 0.25 bar at its maximum corresponding to $t = 1.16$ in Figure 7.2 which is less than the theoretical value 0.913 bar. The eventual cross-over of the two curves as the chart progresses is due to the difference in cooling rates between the two state points P3 and P4. The difference in the experimental and theoretical pressure drop is due to the use of friction factors for PTFE and stainless steel that were taken from literature. While the experimental and theoretical values differ, it is desirable to have minimal loss through the main injection line to limit vapour formation in the line.

If all of the pressure losses in The constants 5.8 and 500 in equation 2.19 to are enable the use of metric units in the equation. The C_v value that is quoted by manufacturers is in imperial units. In equation 2.19, \dot{m}_{ox} is the mass flow rate of oxidiser in kg/hr, SG is the specific gravity of the working fluid and ΔP is the pressure drop across the valve in kPa.

Table 7.1 are summed, the pressure drop amounts to 1.729 bar. From the cold flow testing data, the actual difference between P2 and P4 during the test is indicated in Figure 7.3.

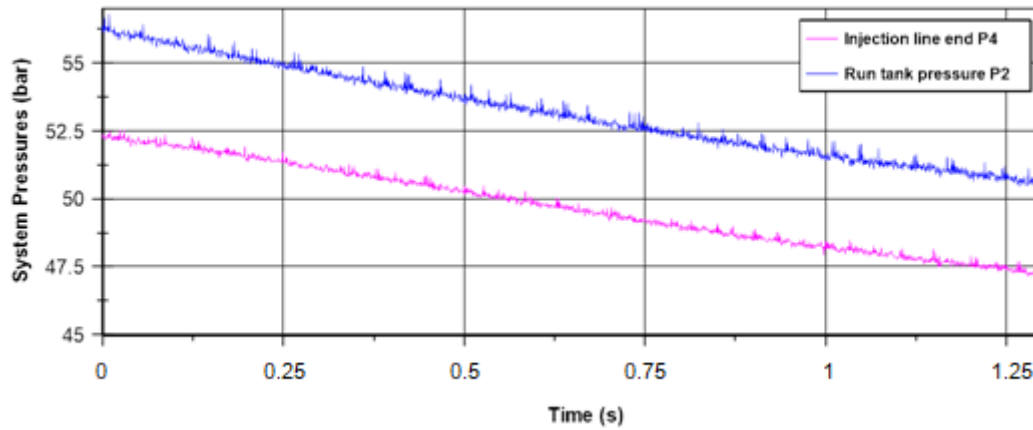


Figure 7.3: Pressures P2 and P4 during cold flow testing

The time plot in Figure 7.3 shows a mean pressure differential of approximately 3.75 bar between P2 and P4. The difference can be accounted for by taking into account the pressure drop across the valve fitted to the nitrous oxide cylinder by the manufacturer of the cylinder. No manufacturer data was provided for this valve and a theoretical pressure drop can therefore not be properly established.

7.2. Injector characterisation

The initial injector that was used was taken from a previous undergraduate project (Theba *et al.*, 2014). The specifications of the injector are in Table 7.2. It was made from an M16 bolt by drilling five holes into the face of the head and boring out the shank. It was designed assuming a single phase homogenous oxidiser. Equation 2.20 shows the relation that was used for the design.

$$C_d A = \frac{\dot{m}_{ox}}{\sqrt{2\rho\Delta P_{inj}}} \quad (2.20)$$

Where, C_d is the coefficient of discharge for the orifice geometry, A is the cross-sectional area of the orifice(s), \dot{m}_{ox} is the mass flow rate of the oxidiser, ρ is the density of the oxidiser, and ΔP_{inj} is the pressure drop across the injector. Using equation 2.20, the resulting pressure drop is calculated at 10.56 bar.

Table 7.2: Initial injector design data

Nitrous oxide density at 25°C	749.3 kg/m ³
Discharge coefficient	0.8
Mass flow rate	0.5 kg/s
Injector orifice diameter	2 mm
Number of orifices	5

The test data showed that the time-averaged mass flow rate for the duration of the blow-down was 392 g/s. In the cold flow test, the injector was discharging to atmosphere. Without a pressurised chamber at the exit of the injector, the pressure differential across the injector cannot be properly established. It was then decided to use the injector in a hot fire test to more accurately characterise its behaviour.

The discharge coefficient of an orifice is related to the geometry of the orifice which is illustrated in Figure 7.4.

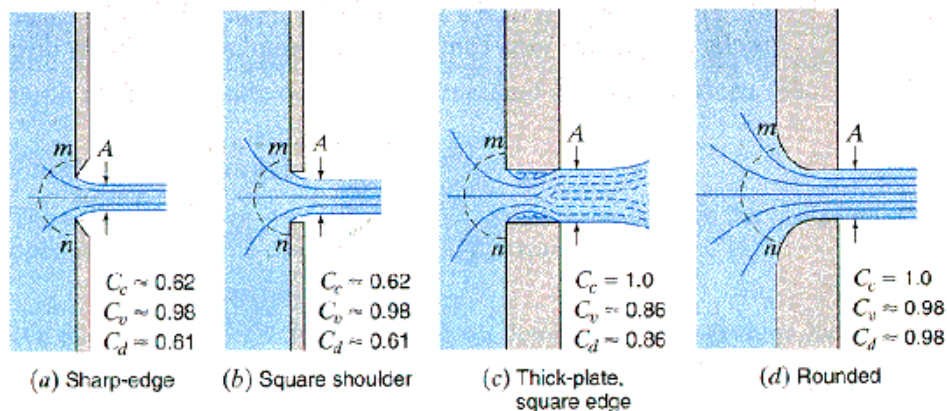


Figure 7.4: Discharge coefficients (numeric-GmbH, 2015)

The comparison in Figure 7.4 shows that the discharge coefficient of 0.8 for the injector discussed above is roughly in line with what was chosen as a fixed design parameter.

During the cold flow testing, the functioning of all of the system's electronics and instrumentation was found to be operating as designed. No leaks were observed in the feed line during the tank blow-down, even as the temperature in the feed line approached -7 °C.

As previously discussed, after the first hot fire test, an instability was observed which was mitigated by reducing the injector orifice diameter and redesigning the injector flange. Due to time constraints, the revised injector design was not subjected to cold flow testing, as the basic design of the injector remained the same and all other systems were already qualified for testing.

8. Hot fire testing

Hot fire testing was done in a dedicated hybrid rocket motor test facility at the University of KwaZulu-Natal's Discipline of Mechanical Engineering building. The area is enclosed by two reinforced soil banks and two exterior walls. A corrugated metal roof provides shelter.

To ensure safety during all hot fire testing, safety marshals were posted along neighbouring walkways and building entrances to prevent access to the area in the vicinity of the facility.

In total, seven hot fire tests were conducted. The first hot fire test was a control test for pure paraffin wax. During the firing of the motor, a malfunction occurred with the LabVIEW program that was discussed in section 4.4, which prevented any data from being recorded during the firing. Thereafter, three pure paraffin wax tests were completed as well as three tests using 40% aluminised fuel grains.

This chapter will document the six tests that successfully captured data. Table 8.1 shows a summary of the testing. Note that the tests are not presented in chronological order. Since both a slab motor and a cylindrical motor (employed for this study) were using the same testing area for hot fire and cold flow testing, a naming nomenclature was implemented. The "L" in Table 8.1 stands for lab-scale and "H" for hot fire. The number that follows is a sequence number. The missing digits between respective tests represent failed attempts at a hot fire test. For ease of reading, the three pure paraffin wax tests are presented first followed by the three 40% aluminium hot fire tests.

Table 8.1 : Hot fire testing summary

Designator	Date	Additive	Burn Time	Igniter
LH-001	2016-06-13	Pure	7,01	Match heads
LH-003	2016-10-21	Pure	13,7	Match heads
LH-007	2017-07-11	Pure	6.43	Pyrotechnic
LH-005	2017-05-29	40% Al	7.94	Pyrotechnic
LH-006	2017-06-15	40% Al	6.79	Pyrotechnic
LH-008	2017-07-12	40% Al	6.71	Pyrotechnic

8.1. LH-001, pure paraffin wax fuel grain

Test LH-001 was the first hot fire test to be documented that produced logged data. This hot fire test used the ignition system that is discussed in section 6.2 and the injector from the undergraduate project with 2 mm orifices. The nozzle was cooled during the burn with a stream of water. A frame of the hot fire test footage is shown in Figure 8.1, while Table 8.2 shows a summary of the data that was produced by the test.



Figure 8.1: LH-001 nozzle plume

Table 8.2: LH-001 data summary

Injector Orifice (mm)	Average Oxidiser Flow (g/s)	Peak Thrust (N)	Average Thrust (N)	Peak Chamber Pressure (bar)	Average Chamber Pressure (bar)	Total Impulse (Ns)	Peak nozzle temperature (°C)
2	255,35	1027,2	569,77	66,86	38	3994,11	263,63

Figure 8.2 shows the time histories of the pre-combustion chamber pressure, propellant tank pressure and the pressure upstream of the injector. The arrows show the two points that were defined as the start and end of the burn so parameters such as average thrust and total impulse could be calculated without ambiguity.

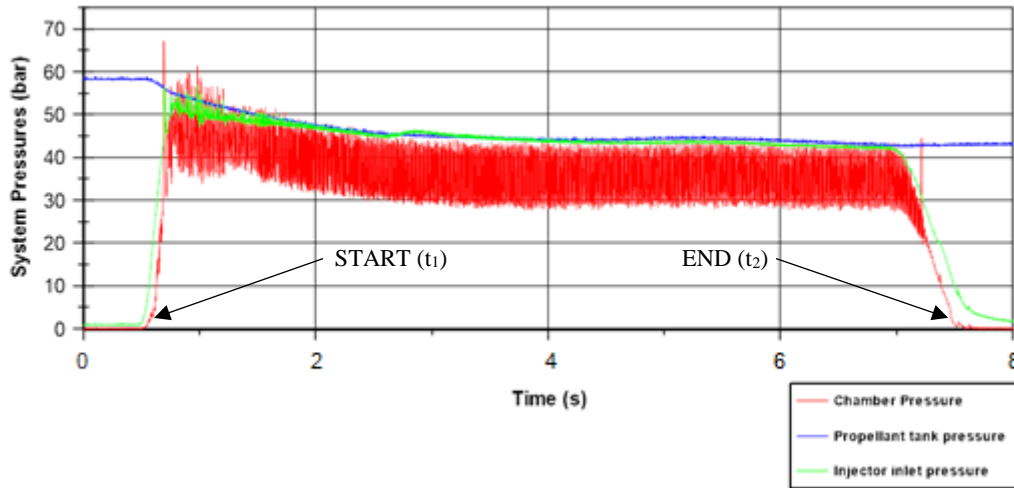


Figure 8.2: Key pressure histories of the LH-001 test

Figure 8.3 shows the thrust produced during the burn.

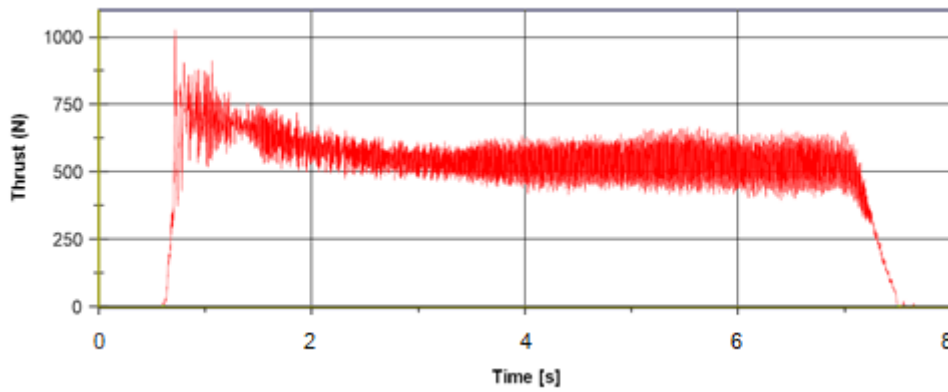


Figure 8.3: Thrust history of the LH-001 test

The average thrust was determined as the integral of the thrust curve divided by the burn time:

$$\bar{F} = \frac{\int_{t_{start}}^{t_{end}} F(t) dt}{t_b} \quad (8.21)$$

The total impulse was calculated integrating the thrust curve over the burn time:

$$I_{total} = \int_{t_1}^{t_2} F(t) dt \quad (8.22)$$

In equation 8.21 and 8.22, \bar{F} is the average thrust over the burn time, $F(t)$ is the time-based thrust signal, and t_b is the burn time. The two calculations were performed in the National Instruments DIAdem package, which was used to analyse the technical data management system (TDMS) data.

As indicated by the chamber pressure history, the burn was highly unstable, with the data showing a peak to peak fluctuation of approximately 15 bar during the course of the burn. Using frequency domain signal analysis tools in LabVIEW, the TDMS chamber pressure data stream was passed through a fast Fourier transform (FFT) to analyse the relative magnitudes of the frequencies making up the signal. Figure 8.4 is an image from the output of the fast Fourier transform.

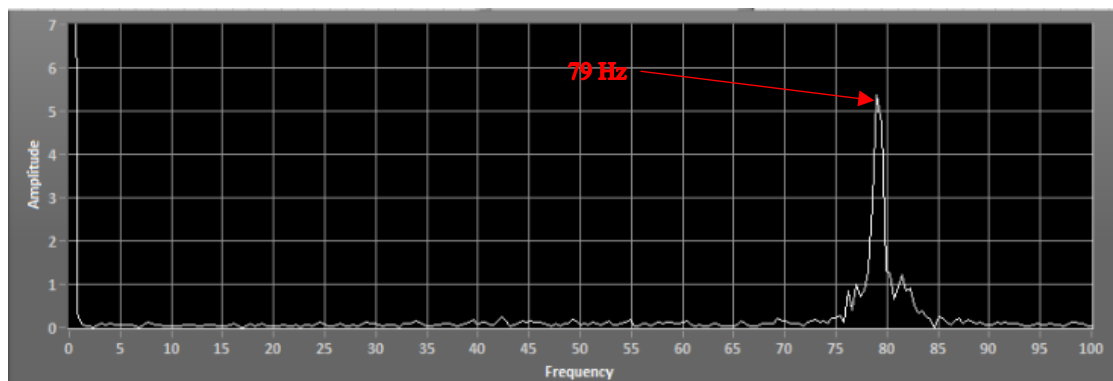


Figure 8.4: Fast Fourier transform of the LH-001 test chamber pressure history

Figure 8.4 shows the FFT of the chamber pressure which displays a peak at 79 Hz. Using the stability data from section 1.8, instabilities such as the dominant hybrid mode and Helmholtz mode could be eliminated. It was consequently proposed that a fundamental fluid mechanic disruption in the pre-combustion chamber area as well as a low injector pressure differential were the cause of the instability.

Hybrid rocket motors rely on a recirculation zone in the pre-combustion chamber that produces good flame holding characteristics and consequently a stable burn. This mechanism is illustrated in Figure 8.5.

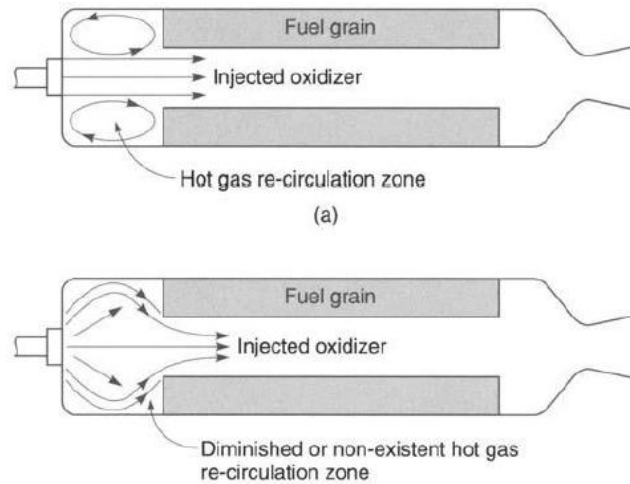


Figure 8.5: Recirculation zone stability (Sutton and Biblarz, 2001a)

The injector bulkhead of the combustion chamber was modified to accommodate the injector from the aforementioned undergraduate project. This resulted in the injector protruding out of the injector bulkhead and reducing the effective length of the pre-combustion chamber, as well as disturbing the fluid mechanics in the vicinity. A magnified cross-sectional view of the injector area is shown in Figure 8.6 to highlight this issue.

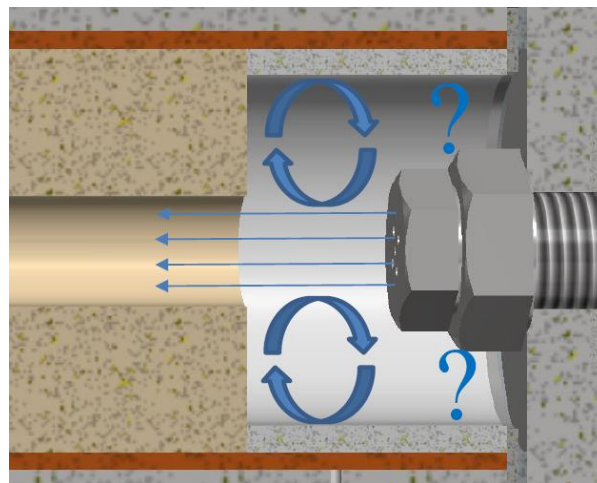


Figure 8.6: Fluid mechanic uncertainty in the pre-combustion chamber

To mitigate the instability, the injector bulkhead was redesigned according to the images in Chapter 2. As part of the modification a new injector with 1.6 mm orifices was also manufactured to increase the injector pressure drop and enable lower chamber pressure operation.

After the chamber was dismantled following the LH-001 test, the fuel grain was removed and sectioned over its length as shown in Figure 9.7. The port diameters at the fore and aft end of the fuel grain were then measured and a time-averaged regression rate was calculated at both ends according to:

$$\bar{r} = \frac{D_{fore} - D_p}{2t_b} \quad (8.23)$$

Where, \bar{r} is the average regression rate over the burn time, D_{fore} is the diameter of the fore-end after the burn, D_{port} is the diameter of the port pre-burn, and t_b is the burn time.

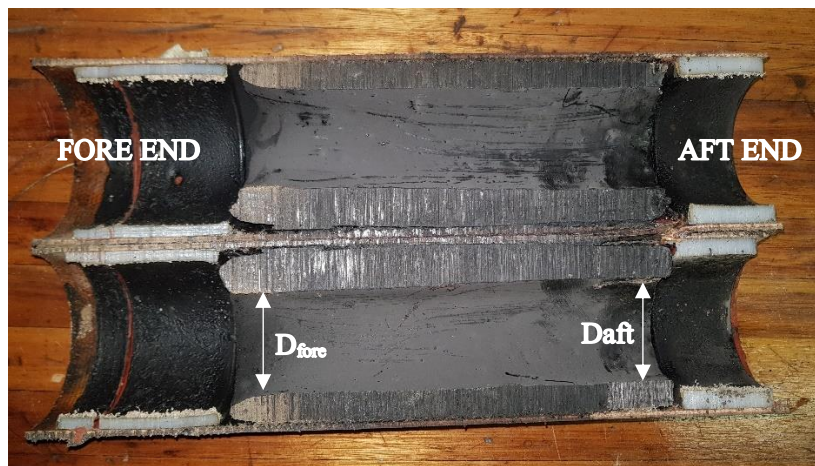


Figure 8.7: LH-001 fuel grain cross-section

Results associated with the fuel grain measurements are shown in Table 8.3.

Table 8.3: Tabulated fuel grain measurements and regression rate

Fore end diameter (mm)	Aft end diameter (mm)	Initial port diameter (mm)
41,5	39,5	19
Regression rate (mm/s)	Regression rate (mm/s)	
1,605	1,462	

The fuel grain regressed in a way that is not typical of hybrid rocket motors. Typically, hybrid rocket motor fuel grains regress conically due to the increase in mass flux along the port which is associated with the addition of fuel. Figure 8.7 also shows that the fuel grain separated from the thermal liner at the fore end of the fuel grain.

8.2. LH-003, pure paraffin wax fuel grain

The test data that is presented is from the next successful hot fire test with the new 1.6 mm injector and the redesigned injector bulkhead. Match heads were again successfully used to ignite the motor. In contrast to the LH-001 test, the nozzle was not cooled during the test. The starting port diameter was changed to 25 mm to reduce the initial oxidiser mass flux. All tests after and including LH-003 used this port diameter. A frame from the test showing the nozzle exhaust plume is shown in Figure 8.8.



Figure 8.8: LH-003 nozzle plume

A summary of the test data is presented in Table 8.4.

Table 8.4: LH-003 data summary

Injector Orifice (mm)	Average Oxidiser Flow (g/s)	Peak Thrust (N)	Average Thrust (N)	Peak Chamber Pressure (bar)	Average Chamber Pressure (bar)	Total Impulse (Ns)	Peak nozzle temperature (°C)
1,6	-	706,63	555*	40,51	35*	7603,5*	514,75

*steady state estimate

During the burn, a malfunction with the host computer resulted in the LabVIEW program freezing. Consequently, the auto-sequence continued to keep the oxidiser valves opened until the computer became responsive again and the burn was terminated.

During this period data could not be recorded. The data that is shown in Table 8.4 was extracted from the 3 seconds of data that was captured after start-up. Since the complete thrust and chamber pressure profiles could not be precisely known, entries in Table 8.4 that are marked with an asterisk are based on a steady-state estimation of the thrust and chamber pressure between $t = 60$ and $t = 61$ in Figure 8.9.

Figure 8.9 and Figure 8.10 show the time histories for the data that were captured during the hot fire test.

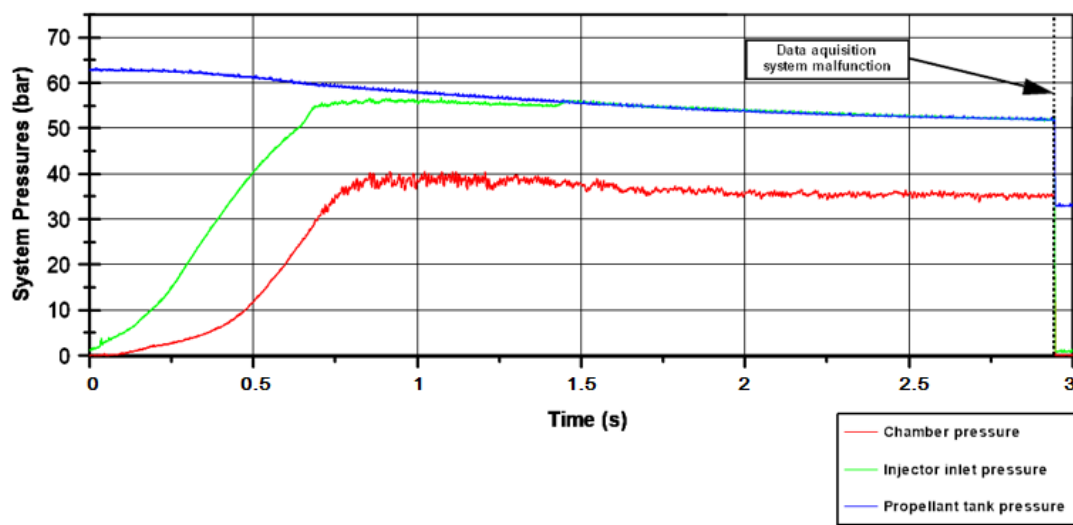


Figure 8.9: Key pressure histories of the LH-003 test

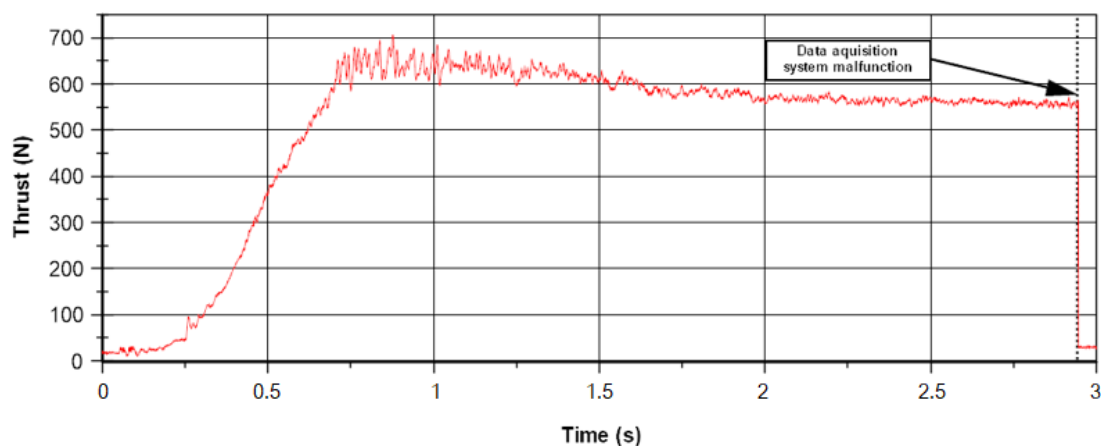


Figure 8.10: Thrust history of the LH-003 test

The data in Figure 8.9 and Figure 8.10 indicate that the injector modifications resolved the instability issue that was present in the LH-001 test. A lower peak chamber pressure and thrust at start-up is also evident.

The fuel grain cross-section and tabulated regression rate measurements are shown in Figure 9.11 and Table 8.5, respectively.



Figure 8.11: LH-003 fuel grain cross-section

Table 8.5: Tabulated fuel grain measurements and regression rate

Fore end diameter (mm)	Aft end diameter (mm)	Initial port diameter (mm)
57,5	69	25
Regression rate (mm/s)	Regression rate (mm/s)	
1,186	1,606	

In this pure paraffin wax case, the fuel grain has burnt with the typical profile. Due to the extended burn time, the fuel has fully regressed in the aft region. While this is not desirable, this test confirmed that the thermal liner performed as it should. The cross-section also shows that the fuel grain did not separate from the thermal liner.

8.3. LH-007, pure paraffin wax fuel grain

Test LH-007 was the third hot fire test of a pure paraffin wax fuel grain and the first test using the new nozzle that had been manufactured. Figure 8.12 shows an image from the test footage.



Figure 8.12: LH-007 nozzle plume

The data summary from this test is shown in Table 8.6.

Table 8.6: LH-007 data summary

Injector Orifice (mm)	Average Oxidiser Flow (g/s)	Peak Thrust (N)	Average Thrust (N)	Peak Chamber Pressure (bar)	Average Chamber Pressure (bar)	Total Impulse (Ns)	Peak nozzle temperature (° C)
1,6	233,28	682,49	495,12	47,93	33,18	3183,61	204,96

The data acquisition system as well as all of the auxiliary instrumentation functioned normally for the duration of the test and all data was captured.

Time histories for key pressures and motor thrust measured during the test are shown in Figure 8.29 and Figure 8.14.

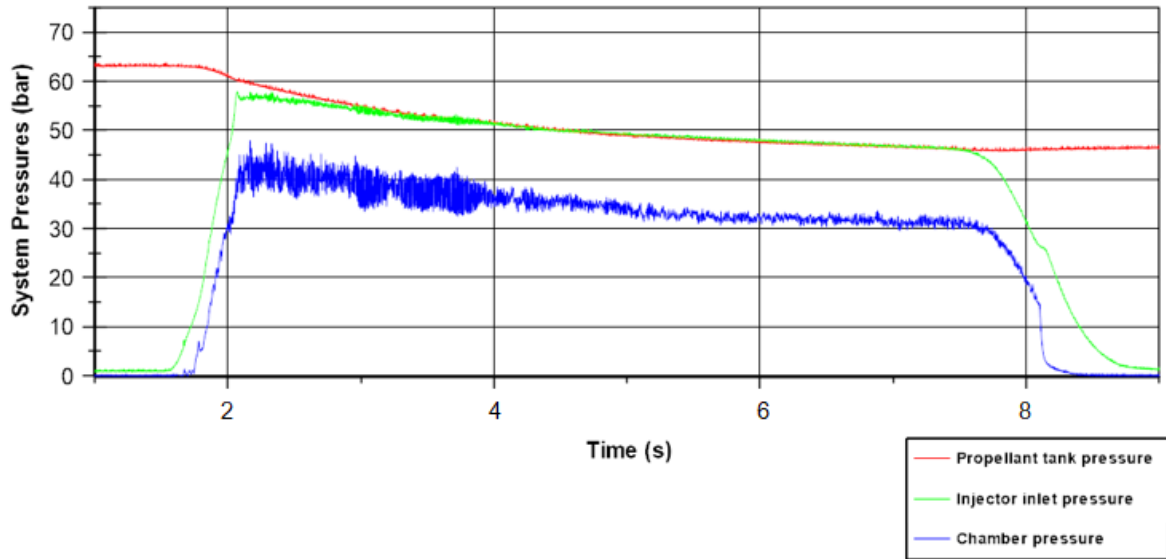


Figure 8.13: LH-007 key system pressures

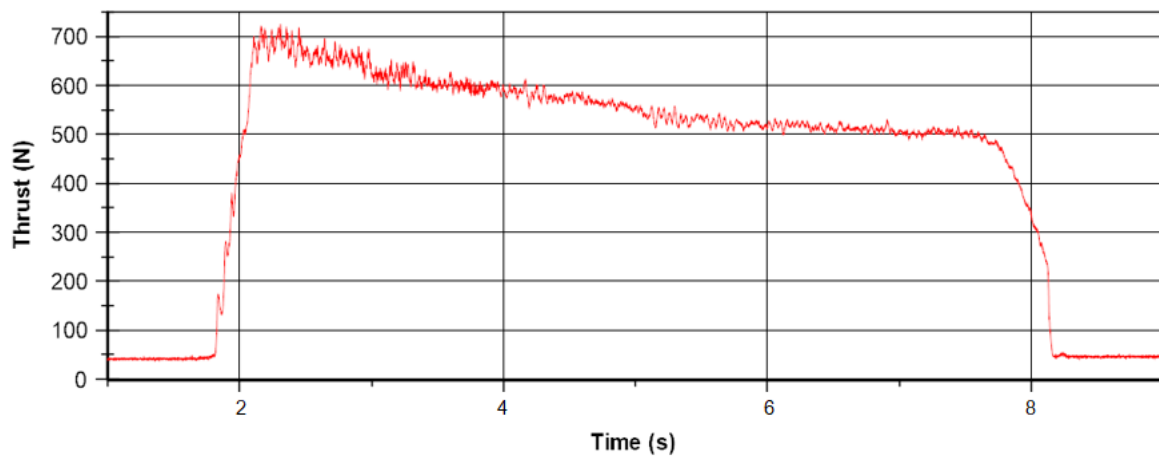


Figure 8.14: LH-007 thrust plot

The test data shows a large oscillation in combustion chamber pressure that ceased after two seconds. By performing a fast Fourier transform of the combustion chamber pressure signal during this time period, the frequency of the oscillation was found to be approximately 97 Hz. A screenshot from the stability analysis program is shown in Figure 9.31.

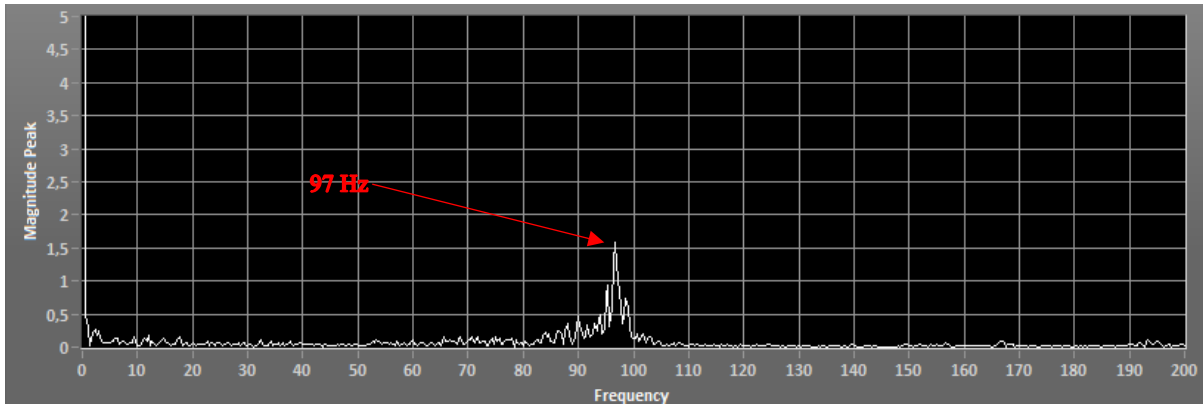


Figure 8.15: Chamber pressure FFT – LH-007

Owing to the brief nature of the instability as well as the literature in section 1.8, the instability can be related to a Helmholtz mode or the result of vortex formation at the leading and trailing edges of the fuel grain in the initial second of the burn.

The thrust history was also consistent with that typically associated with a blow-down oxidiser feed system. This contrasted with previous tests, which produced a flat thrust curve. The difference was attributed to the mass of supercharge gas in the propellant tank at the time of the test.

Each time a hot fire test was undertaken, the propellant tank was not emptied and refilled. This was due to an excess amount being filled each time for safety reasons. The propellant tank was simply filled to a mass of 4 kg of nitrous oxide. There was an amount of nitrogen gas in the tank from the previous test, during the next test, the tank was again supercharged to a pressure of 65 bar resulting in an accumulation of nitrogen gas in the tank that was only vented out once the tank had been emptied. The combustion chamber pressure is fundamentally governed by the oxidiser tank pressure and due to the variance in the amount of supercharge gas in the tank, the blow down dynamics differ from test to test.

While it is known that this will marginally affect the thrust and chamber pressure curves of each test, an increase in performance (if any) due to the aluminised fuel in the following tests should still be clearly evident.

After the test, disassembly of the combustion chamber showed that the nozzle did not deform or change dimensionally in any way. A picture of the nozzle after the hot fire test can be seen in Figure 8.16.



Figure 8.16: Copper nozzle after LH-007

The fuel grain's cross-section and the tabulated regression rate measurements are provided in Figure 8.33 and Table 8.11, respectively.



Figure 8.17: LH-007 fuel grain cross-section

Table 8.7: Tabulated fuel grain measurements and regression data

Fore end diameter (mm)	Aft end diameter (mm)	Initial port diameter (mm)
42,5	53,2	25
Regression rate (mm/s)	Regression rate (mm/s)	
1,361	2,193	

This test shows good adhesion between the fuel, pre and post combustion chambers, and the thermal liner. The fuel was burnt in a characteristic conical profile.

8.4. LH-005, 40% aluminised fuel grain

Test number LH-005 was the first successful attempt of an aluminised fuel grain. A previous attempt using match heads as an igniter failed to ignite the motor (LH-004). The pyrotechnic igniter discussed in Section 6.3 was used successfully. All tests thereafter also made use of the pyrotechnic igniter. The nozzle was cooled with water during this test in order to mitigate possible nozzle erosion and/or melting as a result of the increased temperature generated by the burning aluminium particles.

Figure 8.18, derived from video footage, shows a shower of burning aluminium particles being ejected from the nozzle. A distinctly different exhaust plume shape and luminescence is also exhibited. Data from the test are shown in Table 8.8.



Figure 8.18: LH-005 exhaust plume

Table 8.8: LH-005 data summary

Injector Orifice (mm)	Average Oxidiser Flow (g/s)	Peak Thrust (N)	Average Thrust (N)	Peak Chamber Pressure (bar)	Average Chamber Pressure (bar)	Total Impulse (Ns)	Peak nozzle temperature (° C)
1,6	191,44	653,5	518,52	42,15	28	4117,02	413,24

The data acquisition system performed normally, and all the test data was successfully recorded. Time histories of system pressures and thrust are shown in Figure 8.13 and Figure 8.14.

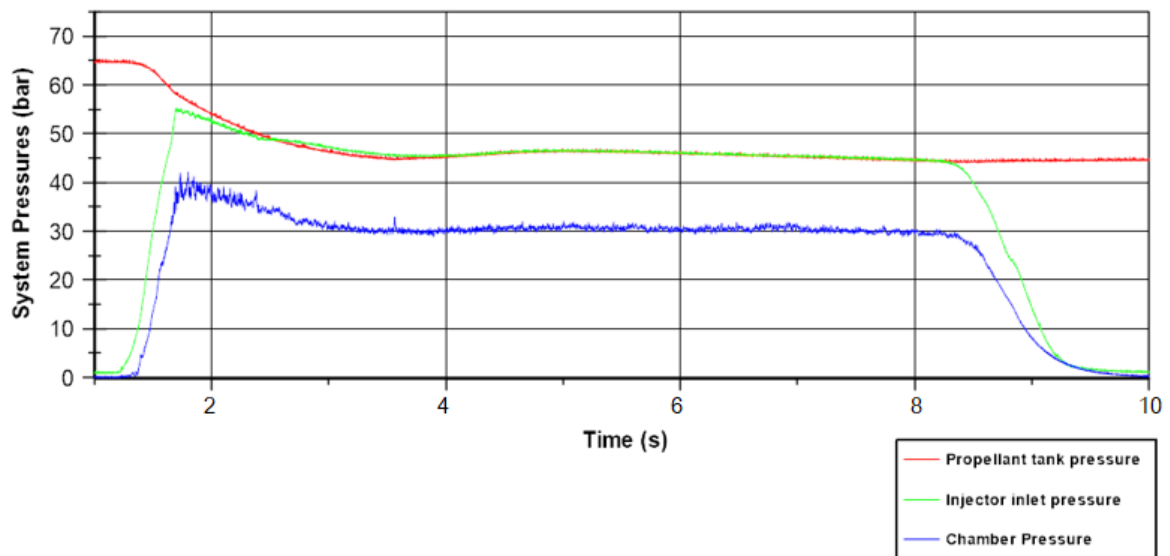


Figure 8.19: LH-005 key system pressures

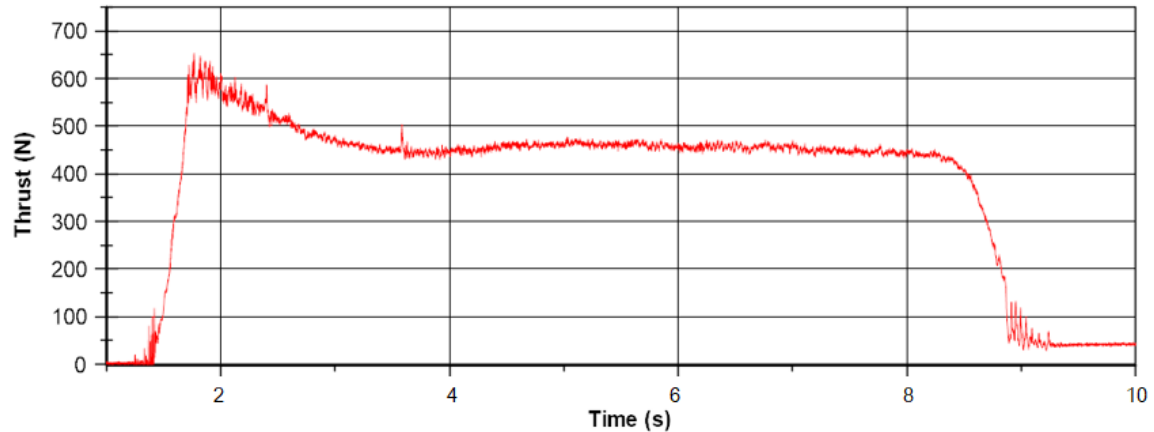


Figure 8.20: LH-005 thrust plot

The burn proceeded normally with no anomalies seen in the test data. The data shows no instability in the combustion process but does show a flat thrust curve, which is inconsistent with a blow-down hybrid rocket motor but is consistent with the data in Figure 5.2 showing that a 40% aluminised fuel grain has a lower performance dependence on the O/F ratio.

During the first second of the hot fire test, the footage shows a large amount of burning aluminium being ejected from the nozzle. This is shown as a frame from the test footage, in Figure 8.21.



Figure 8.21: Burning aluminium ejected during hot fire testing

The morning following the test, the wire mesh fence that was seen being struck with burning aluminium was examined. Portions of the fence were covered with thin pieces of aluminium, as shown in Figure 8.22. This is evidence of a substantial amount of unburnt aluminium being ejected during the combustion process, an indication that the specific type of aluminium powder that is being used does not burn completely under these conditions. This may be due to the particle size, thickness of the oxide layer, quantity of aluminium in the fuel grain or the geometry of the fuel grain not allowing sufficient residence time for the particles to combust.



Figure 8.22: Aluminium collected from fencing

Disassembly of the combustion chamber after the hot fire test showed a large amount of slag, soot, and unburnt aluminium on the converging face of the nozzle. This is shown in Figure 8.23.



Figure 8.23: Slag formation on the nozzle during test LH-005

Once the slag was carefully removed from the nozzle, it was revealed to be a mixture of soot and aluminium powder that had melted and pooled against the nozzle.

The nozzle showed no deformation or dimensional changes. A small amount of melted aluminium was found at the interface of the converging section and throat. This accumulation could not be removed without damaging the nozzle and seemed to be melted into the copper itself. A picture of the nozzle in this state is shown in Figure 8.24, with the removed slag shown on the left.



Figure 8.24: Nozzle with removed accumulation

A cross-section of the fuel grain is shown in Figure 8.25, while regression rate data is presented in Table 8.7.



Figure 8.25: LH-005 fuel cross-section

Table 8.9: Tabulated fuel grain measurements and regression rate

Fore end diameter (mm)	Aft end diameter (mm)	Initial port diameter (mm)
46,4	55,5	25
Regression rate (mm/s)	Regression rate (mm/s)	
1,348	1,921	

The cross-sectional view of the combustion chamber shows good adhesion between the thermal liner and fuel grain. A homogeneous distribution of the aluminium particles was also seen. At the aft end of the fuel grain, there was an accumulation of aluminium suspended in paraffin wax.

8.5. LH-006, 40% aluminised fuel grain

The following is from the second test of an aluminised fuel grain. All parameters of the test were the same as those associated with test LH-005. These include the injector type and mass flow rate of oxidiser as well as the geometry of the fuel grain and additive mass percentage. A frame from the footage showing the nozzle plume is shown in Figure 8.26.



Figure 8.26: LH-006 nozzle plume

Table 8.10 shows the test data summarised.

Table 8.10: LH-006 data summary

Injector Orifice (mm)	Average Oxidiser Flow (g/s)	Peak Thrust (N)	Average Thrust (N)	Peak Chamber Pressure (bar)	Average Chamber Pressure (bar)	Total Impulse (Ns)	Peak nozzle temperature (° C)
1,6	N/A	604,39	464,86	37,47	29,53	3156,43	NC*

* not connected

Although the data acquisition and control systems functioned normally, the load cell that measures the propellant tank mass was not connected to the cDAQ system due to a faulty cable connection that was only found after the test. In addition, data from the nozzle thermocouple suggested that it was not connected, although the preparation checklist shows that the thermocouple was indeed connected. It likely became loose at some time before the hot fire test.

Pressures and thrust histories are shown in Figure 8.27 and Figure 8.28.

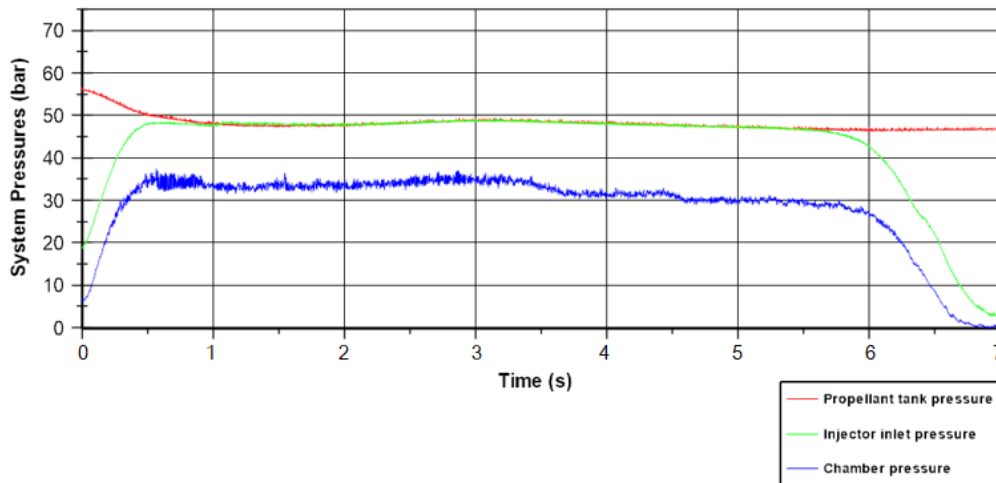


Figure 8.27: LH-006 key system pressures

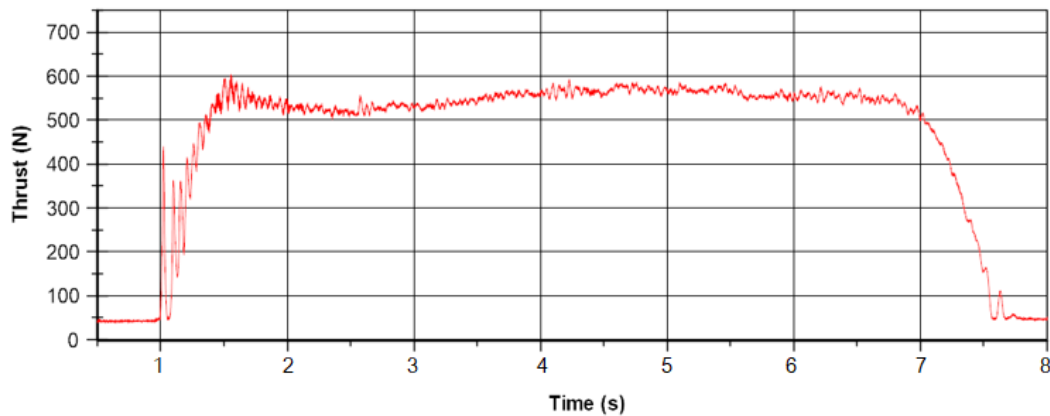


Figure 8.28: LH-006 thrust plot

With reference to the system pressures, the chamber pressure shows a fluctuation during the first second of the burn that then stabilises. Half way through the burn, the chamber pressure reduces from 35 bar to 30 bar. During this exact time, the thrust does not appear to change. This could be attributed to changes in the geometry of the nozzle due to erosion/melting or changes in the dynamics of the

aluminium particle combustion. An alternate reason for this observed phenomenon may be an increase in the mass flow rate through the nozzle driven by a period of increased combustion temperature and therefore increased regression rate. As instantaneous regression rate data is not available, it is difficult to arrive at a conclusion regarding this phenomenon.

Removal of the nozzle after the test showed larger amounts of aluminium/slag accumulation compared to the previous aluminised test. The deposits were loosely attached to the nozzles converging face resulting in the accumulation being retained by the post combustion chamber insert upon removal of the nozzle.

A picture of the deposits on the nozzle is shown in Figure 8.29. Note that the combustion chamber view is from the aft/nozzle end looking towards the injector end.

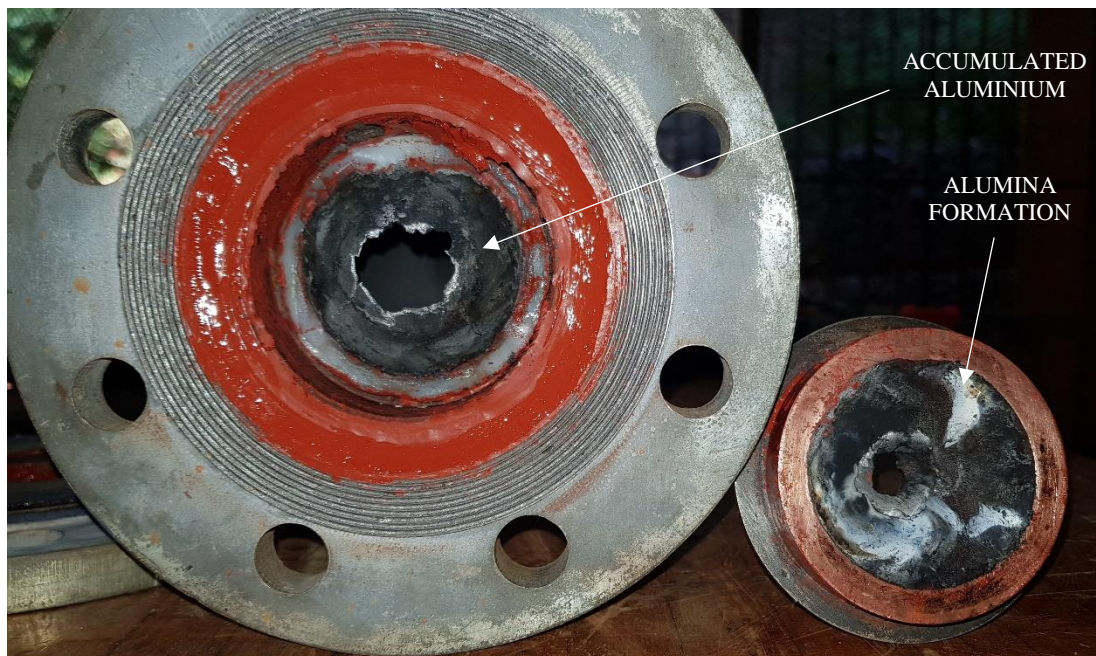


Figure 8.29: Aft end molten aluminium

The converging face of the nozzle shows a white formation consistent with the colour of aluminium oxide or alumina. This was an indication of aluminium oxidation that was not seen to the same extent in the previous aluminised test.

The nozzle showed localised melting in the throat area, towards the converging face. The problem would have been exacerbated by the aluminium deposit from the previous test that could not be removed. A magnified image of the nozzle can be seen in Figure 8.30, with the melted area circled in red.



Figure 8.30: Damaged nozzle

The damaged throat region can also be seen from the diverging side, with small amounts of aluminium/alumina evident.

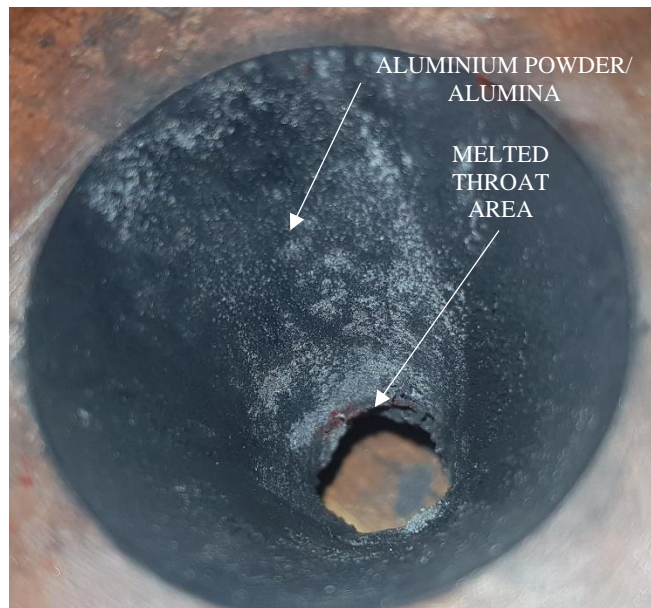


Figure 8.31: Nozzle diverging end

Figure 8.31 shows the nozzle as seen from the divergent portion. The melted throat section of the nozzle can be seen in this view. There is also a layer of unburnt aluminium powder on the surface of the diverging section

The injector flange was seen with a layer of solidified paraffin wax coated in alumina which was characterised by a light white coating and hard surface. This can be seen in Figure 8.32.



Figure 8.32: Injector flange after LH-006

The fuel grain cross-section and the regression rate data associated with the test are shown in Figure 8.33 and Table 8.11 .

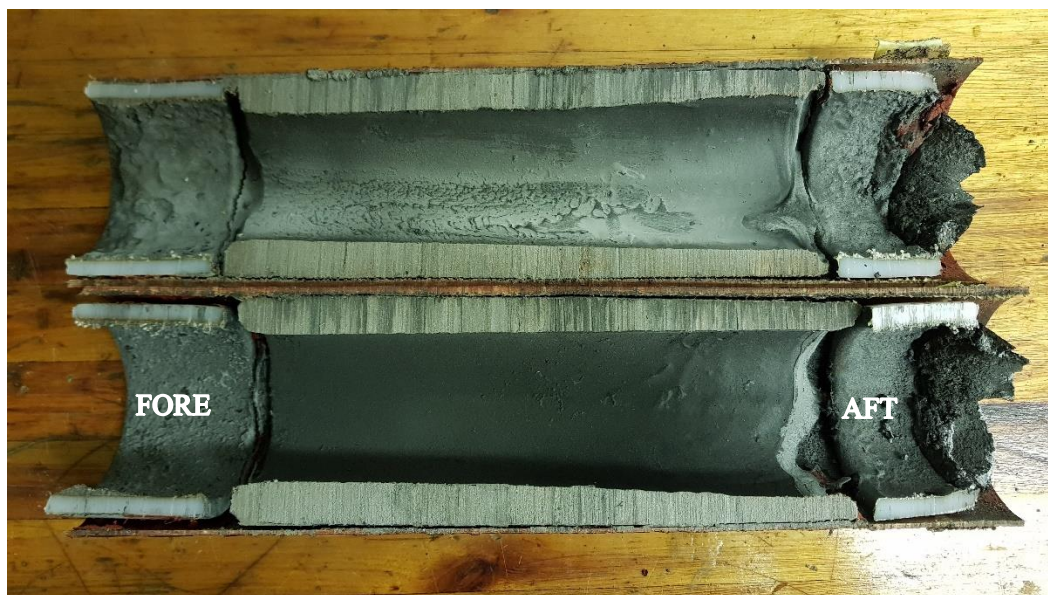


Figure 8.33: LH-006 fuel cross-section

Table 8.11: Tabulated fuel grain measurements and regression data

Fore end diameter (mm)	Aft end diameter (mm)	Initial port diameter (mm)
47,8	54,6	25
Regression rate (mm/s)	Regression rate (mm/s)	
1,679	2,180	

The separation of the fuel grain against the thermal liner was a result of the cross-sectioning process. Both the pre and post combustion chamber inserts have been separated from the thermal liner. In the top half of the picture in Figure 8.33, a light coating of alumina can be seen.

Since the nozzle could not be used for a further test, a new nozzle was manufactured to the same dimensions to produce one additional set of test data for both paraffin wax and 40% aluminium (LH-007 and LH-008).

8.6. LH-008, 40% aluminised fuel grain

This test was the final hot fire test of the study, and the last aluminised hot fire test. A frame from the test footage is shown in Figure 8.34.



Figure 8.34: LH-008 nozzle plume

The frame was taken at a point in the burn where a large amount of burning aluminium was seen being ejected from the nozzle.

The data from the test is presented in Table 8.12.

Table 8.12: LH-008 data summary

Injector Orifice (mm)	Average Oxidiser Flow (g/s)	Peak Thrust (N)	Average Thrust (N)	Peak Chamber Pressure (bar)	Average Chamber Pressure (bar)	Total Impulse (Ns)	Peak nozzle temperature (° C)
1,6	202,68	686	453,93	44,11	28,95	3045,86	449,51

Once again, the data acquisition and control system performed nominally for the duration of the test and all data was captured. The system pressures and thrust profile are plotted in Figure 8.35 and Figure 8.36, respectively.

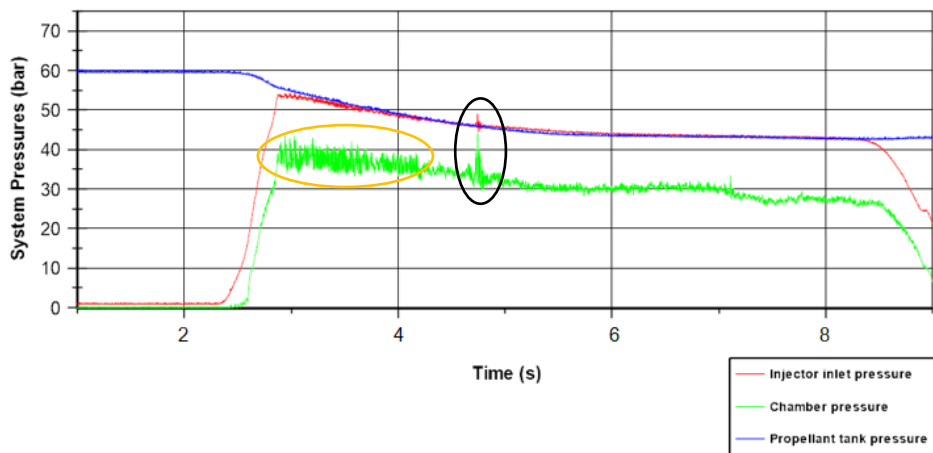


Figure 8.35: LH-008 key system pressures

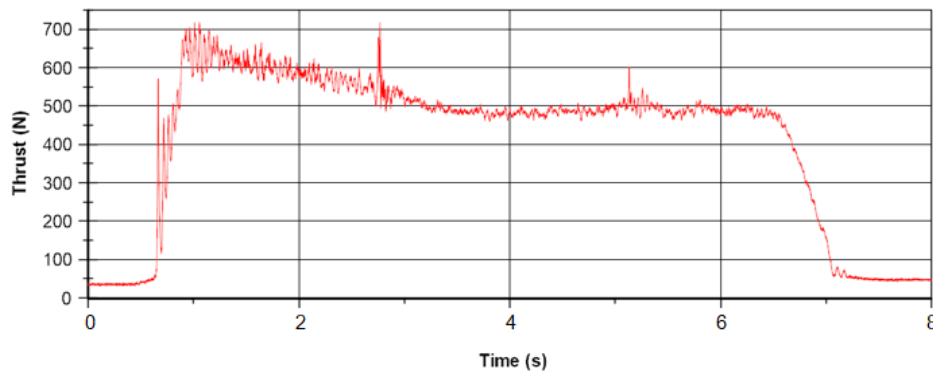


Figure 8.36: LH-008 thrust plot

The burn once again produced a thrust curve that was flat and not indicative of blow-down oxidiser delivery. The reason for this difference is discussed in section 8.3. The ejection of aluminium in Figure 8.34 corresponds to the data that is circled in Figure 8.35. The spike in the chamber pressure and thrust are related to the ejection of material from the nozzle.

An FFT of the chamber pressure signal during the time interval circled in black yielded the result in Figure 8.37 from the stability analysis program that was written in LABView.



Figure 8.37: Chamber pressure FFT – LH-008

While the result is consistent with the literature review data of chuffing, describing it as a low frequency process, it is thought that the pressure and thrust spike are not related to chuffing due to the short duration of the material ejection. Chuffing has previously been described as a continuous process. This was not evident in the other aluminised test.

In Figure 8.35, circled in orange is an instability in the combustion very similar in nature to the previous tests involving pure paraffin wax, but lasting for a shorter duration.

Stability analysis showed that the frequency of the pressure oscillation was 90 Hz.

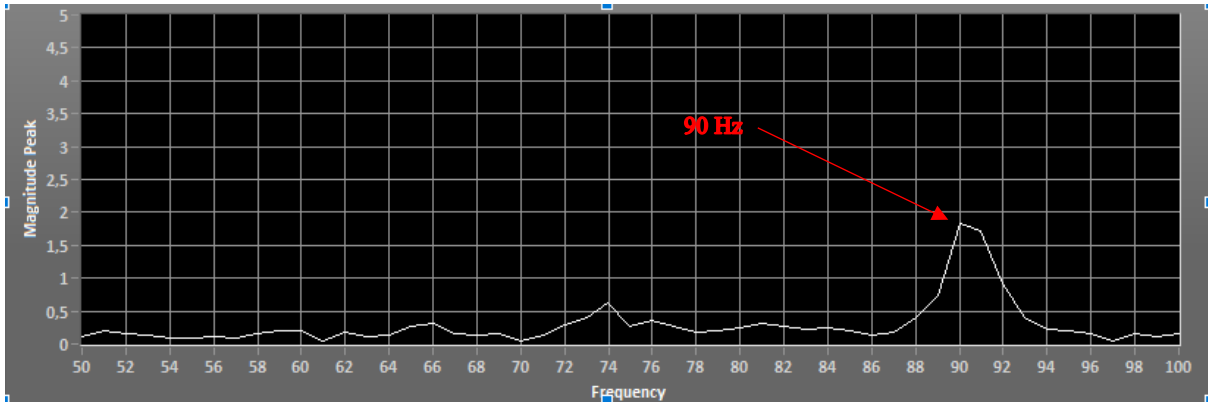


Figure 8.38: Chamber pressure FFT

The pressure fluctuations are in line with what was observed in a previous test with pure paraffin wax (LH-007). Although there is a difference in the frequency of 9 Hz, the frequencies are in the same neighbourhood that suggest that the oscillations are not attributable to the solid propellants chemical makeup but rather to fluid dynamic phenomena inside the combustion chamber that was previously discussed in the stability analysis in section 8.1. Comparing tests LH-007 and LH-008, the solid propellant differs as LH-007 is pure paraffin wax and LH-008 contains 40% aluminium. The geometry of the combustion chamber and injector are however, constant.

After the hot fire test, the chamber was once again dismantled, and the nozzle removed. Again, the nozzle showed a large amount of accumulation on the converging face and damage in the throat region owing to localised melting of the copper. The area circled in red in Figure 8.39 shows spots of alumina formation on the inlet of the nozzle.



Figure 8.39: Nozzle accumulation

The throat region is seen in Figure 8.40 in a magnified view to highlight damage to the throat region. The region in which the throat has melted away is shown in a red circle.



Figure 8.40 : Melted throat area

The fuel grain cross-section and tabulated data for the regression measurements are shown below in Figure 8.41 and Table 8.13.

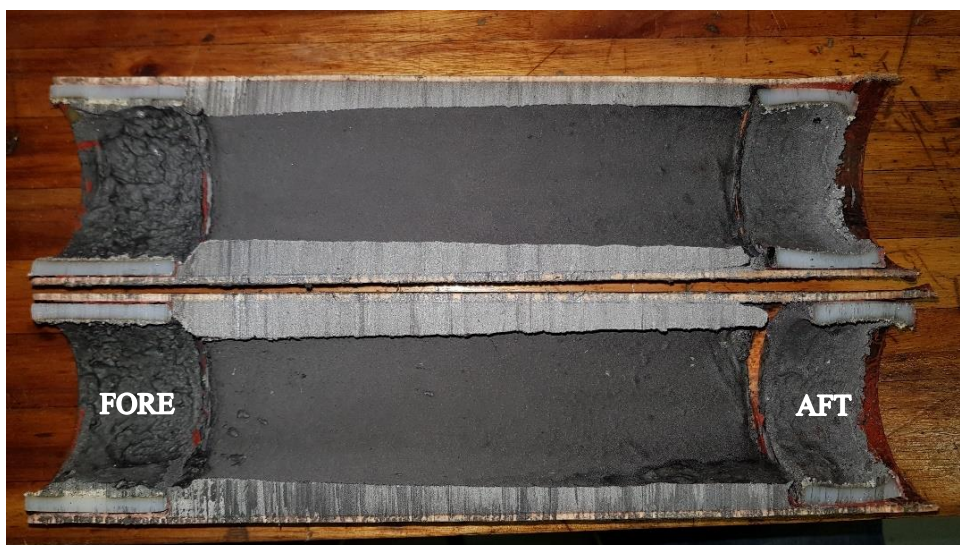


Figure 8.41: LH-008 fuel cross-section

Table 8.13: Tabulated fuel grain measurements and regression data

Fore end diameter (mm)	Aft end diameter (mm)	Initial port diameter (mm)
45	51	25
Regression rate (mm/s)	Regression rate (mm/s)	
1,490	1,937	

8.7. Summary of hot fire testing

Before progressing to a discussion of the hot fire testing, a summary of the hot fire tests is shown in tabulated form with the parameters of interest, in Table 8.14.

Table 8.14: Summary of key parameters from hot fire testing

Test Designator	Average Oxidiser Flow (g/s)	Peak Thrust (N)	Average Thrust (N)	Peak Chamber Pressure (bar)	Average Chamber Pressure (bar)	Total Impulse (Ns)
LH-001 Pure wax	255,35	1027,2	569,77	66,86	38	3994,11
LH-003 Pure wax	N/A	706,63	555*	40,51	35*	7603,5*
LH-007 Pure wax	233,28	682,49	495,12	47,93	33,18	3183,61
LH-005 Aluminised	191,44	653,5	518,52	42,15	28	4117,02
LH-006 Aluminised	Error	604,39	464,86	37,47	29,53	3156,43
LH-006 Aluminised	202,68	686	453,93	44,11	28,95	3045,86

8.8. Discussion of hot fire testing

The central aim to this study was to characterise the performance of metal additives, in particular, aluminium, from both a performance and practical perspective. With substantial differences in the burn time for some of the tests and a lack of real time regression rate data, performance was deduced using parameters such as time-averaged regression rate, density specific impulse, characteristic velocity and, combustion efficiency.

Figure 8.42 shows the time-averaged regression rate data from the fore-end of the fuel grain. The time-averaged result was obtained by measuring the port diameter pre and post firing and dividing the radial change by the burn time.

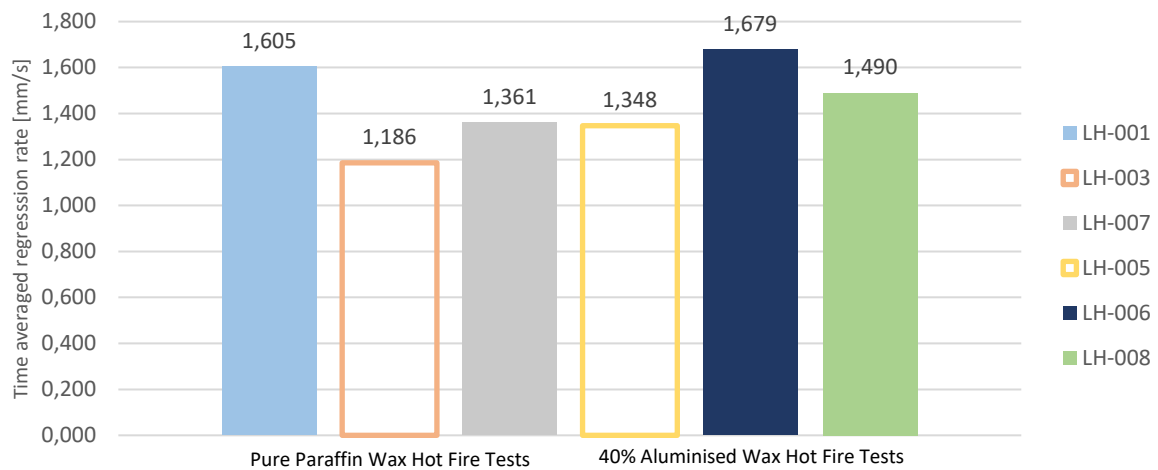


Figure 8.42: Fore-end regression rate data

Since the time-averaged regression rate depends on the burn time and there were differences between each test, time-averaged regression rate data cannot be used alone to make any deductions. In Figure 8.42, test LH-003 and LH-005 had burn times that were substantially different from the other tests. For this reason, their bars are outlines and not filled. All of the other tests had a burn time of 6.75 s on average, ± 0.3 s. Comparing test LH-007 (pure) directly with tests LH-006 and LH-008 (aluminised), an enhancement in the regression rate of 23 % and 9.5 % respectively, is observed. The former is in line with the reported enhancement seen in section 1.61, while the latter is substantially below the reported 25 % enhancement. When the other tests are considered, variations in the aluminium powder batches and the burn times result in a data set with no clear conclusion. The aluminised fuel grains were cast from two different batches of aluminium powder purchased one year apart.

Since this project aimed to determine the performance characteristics of the solid propellant, using specific impulse as a metric of performance does not, in this case, offer a true representation of the

rocket motor's performance since differences between the solid fuel density are not taken into account. Further, literature and theoretical predictions show that the increase in peak specific impulse is marginal comparing a pure paraffin wax grain with an aluminised grain. A more useful representation is density specific impulse, which is simply the product of specific impulse and the density of the propellants. The data are shown in Figure 8.43.

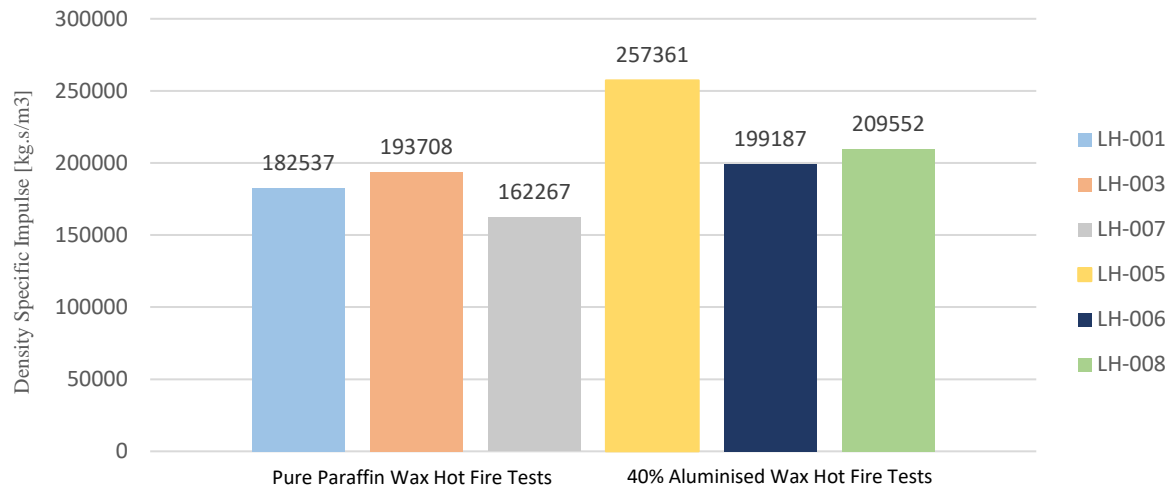


Figure 8.43: Density specific impulse data

Due to the difference in the density between the pure paraffin wax and aluminised paraffin wax fuel grains, the data in Figure 8.43 shows that in the case of the aluminised fuel grains, the density specific impulse is higher. When designing a rocket motor for a launch vehicle, it is desirable to increase the density specific impulse of the propulsion system to yield a design that is more volumetrically efficient. An increase in the density specific impulse means that as more compact rocket can be designed as the thrust obtained per unit of propellant volume is maximised.

As mentioned previously, a measure of the thermochemical merits for a given propellant is characteristic velocity, defined as:

$$c^* = \frac{P_c A_t}{\dot{m}_{total}} \quad (8.24)$$

The characteristic velocities for the 40 % aluminised paraffin wax set of tests is shown in Figure 8.44. In each case, the calculation was done by measuring the mass of the fuel grain before and after the burn, adding the mass to the total mass of oxidiser consumed, and then averaging over the burn time to give the average overall propellant mass flow rate. The average chamber pressure and throat diameter of 12 mm was then used to complete the calculation.

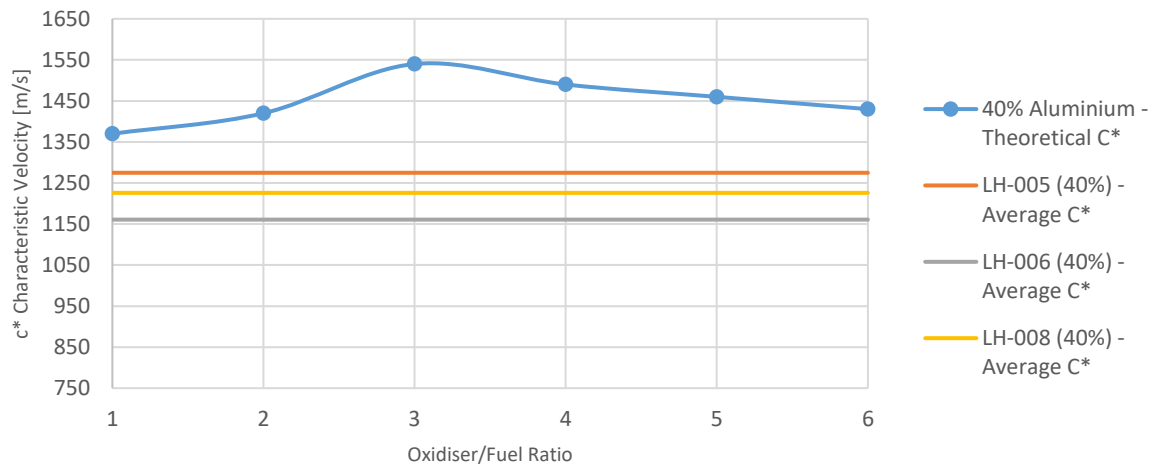


Figure 8.44: Comparison of experimental and theoretical characteristic velocities for a 40% aluminised fuel grain

The blue curve in Figure 8.44 was calculated in NASA CEA for a 40 % by mass aluminised fuel grain. Each of the three lines below the theoretical curve are the average characteristic velocities for each test. They are represented as horizontal lines as the exact O/F ratio at every point in the burn cannot be known.

For each of the three paraffin wax hot fire tests that were undertaken, the same calculation was done. The data are shown in Figure 8.45.

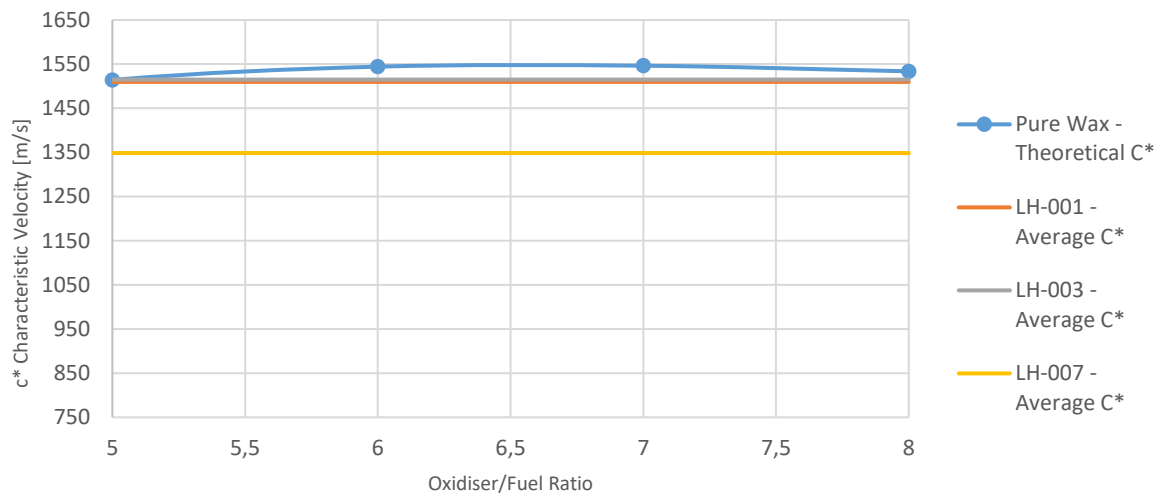


Figure 8.45: Comparison of experimental and theoretical characteristic velocities for pure paraffin wax hot fire testing

In this case (pure paraffin wax), it can be seen that the average data values from the hot fire tests are closer to the theoretical curve in blue. The data in Figure 8.44 and Figure 8.45 then be summarised by calculating the combustion efficiency. Combustion efficiency is a comparison between the theoretical and experimental characteristic velocity. The data are shown in Figure 8.46.

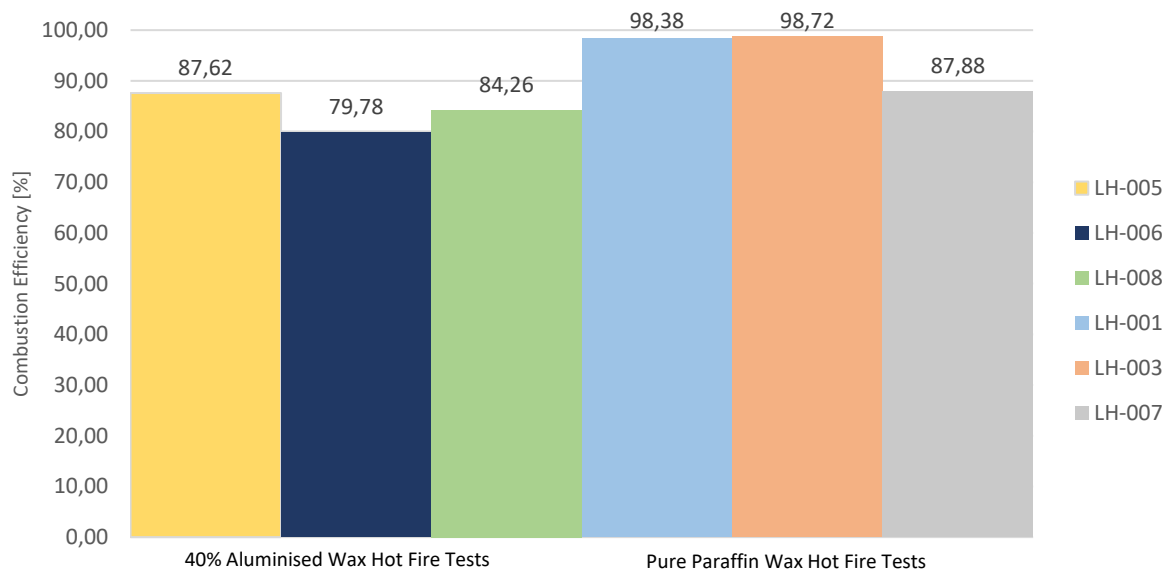


Figure 8.46: Combustion efficiencies for pure and aluminised fuel grains

It can be seen that the pure paraffin wax tests achieved a higher combustion efficiency during the hot fire testing. The reason for the high combustion efficiencies for the pure paraffin wax test is unknown. The injector that was designed for all of the hot fire testing was based on a mass flow rate of oxidiser that is in line with what would be demanded by a pure paraffin wax fuel grain. This means that in the case of the aluminised tests, the oxidiser that was provided to the combustion chamber was in excess of what was demanded by the fuel as a 40 % aluminised fuel grain burns at a lower O/F ratio compared to pure paraffin wax (approximately half that of pure wax). In terms of the data in Figure 8.46, this means that the aluminised tests had an overall mass flow rate higher than what would normally be designed for.

An additional and more important factor for the low combustion efficiency is the poor combustion of the aluminium particles. During the testing, all of the aluminised tests showed burning aluminium being ejected from the nozzle at one or multiple points in the burn. Aluminium particles that burn outside of the combustion chamber do not make any positive contributions from a performance perspective but reduce combustion efficiency as the energy resulting from the burning particles can no longer be transferred to the solid fuel grain as they are now burning outside of the combustion chamber once they are ejected.

After each hot fire test, accumulations of slag, aluminium powder/wax, and alumina could be seen inside the fuel grain cartridge after the fuel grains were cut in half. This provides visual evidence that the combustion of the specific type of aluminium powder used in these tests is poor owing to the particle size and/or oxide layer.

In the context of a launch vehicle, a parameter of interest is the total impulse. In orbital mechanics, the “delta-V” or change in velocity of the vehicle is derived from the total impulse produced by the propulsion system of the rocket. A certain delta-V is required for a design apogee to be obtained or to perform an orbital manoeuvre. The total impulse for all of the hot fire tests are shown in Figure 8.47.

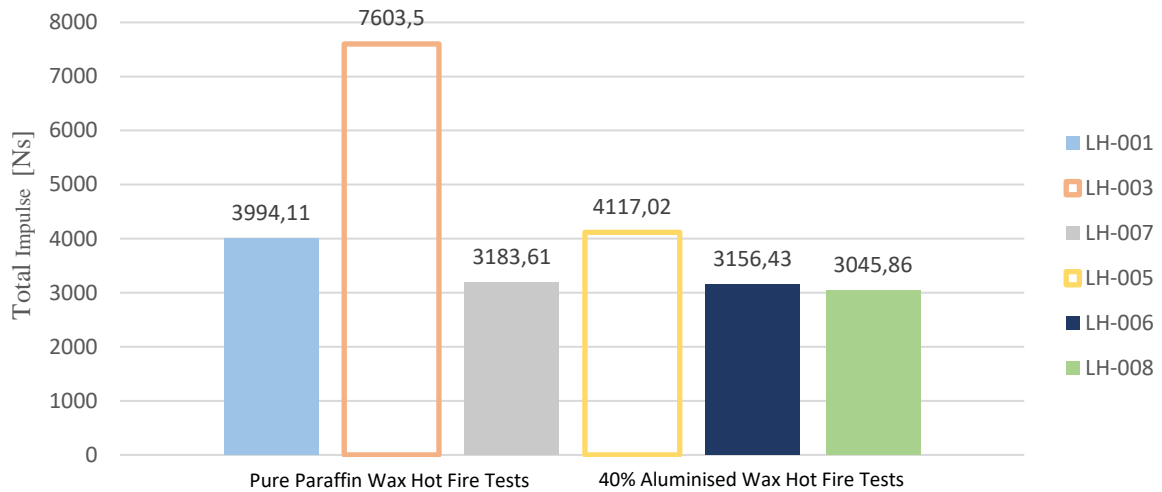


Figure 8.47: Total impulse data - comparison

In Figure 8.47, the bars for test LH-003 and LH-005 are not filled as the burn times were dissimilar. The data above shows no clear evidence that the aluminisation of the paraffin wax increases the total impulse derived from the motor, an expected result taking into consideration similarity in the average and steady-state thrust values as well as the average oxidiser mass flow rates.

An important factor in terms of combustion dynamics was the type of aluminium powder that was used. Substantial amounts of aluminium powder was seen being ejected from the nozzle while still burning. In this case, aluminium powder with an oxide layer and large particle size was used (75 micron). If the aluminium powder was stripped of its oxide layer chemically or produced in an inert environment, the residence time required for the particles to fully combust within the chamber will be lower resulting in a larger portion of the aluminium particles being burnt within the combustion chamber.

9. Conclusion

At the outset, the aim of this project was to characterise the performance of metal additives in paraffin wax fuel grains. After a review of literature, aluminium was chosen as an additive to test due to its low cost, availability, inertness in ambient conditions, and ultimately, its potential to increase the effective propellant density in hybrid rocket motors that utilise paraffin wax and nitrous oxide.

To perform necessary experimentation on aluminium as a fuel additive, a suitable testing platform was developed, which used the combustion chamber from a previous undergraduate project. The combustion chamber was used successfully for all of the hot fire testing and has not been damaged in any way by the series of hot fire tests. The copper nozzle that was used was damaged during testing of the aluminised grains, prompting the manufacture of a new nozzle made to the same dimensions.

As part of the testing platform that was commissioned, a propellant distribution system was developed. In terms of mechanical criteria, such as strength and longevity of components, the feed system instrumentation performed satisfactorily and, at the time of writing this document, is being used for hot fire testing by other postgraduate students in the ASReG research group. As part of the feed system, the custom-developed valve allowed for safe and reliable hot fire testing in its second design iteration. Regarding its reliability, recommendations will be made in section 9.1.

In terms of the LabVIEW program that was developed for this project, Waterfall, many of the bugs that were evident in the early testing phase of the project were rectified. With regard to the current electronic set-up, there is little room for the program to evolve in terms of the core algorithms. Improvements can however be made to the user interface.

In developing a suitable igniter for the experimentation, it was evident that the non-pyrotechnic solutions were not suitable for the purpose of propellant ignition. The steel wool method that was explored proved to be unsuitable, as it did not burn for a period long enough to vaporise and then ignite the paraffin wax in the oxidiser-rich environment within the combustion chamber. Low energy ignition systems such as steel wool can allow for a dangerous set of circumstances to occur. As nitrous oxide fills the combustion chamber once the oxidiser valve is opened, if an ignition source such as a glowing filament of steel wool is present, an explosive decomposition can then, in theory, be initiated. The resulting pressure spike could then lead to potential damage of the combustion chamber and oxidiser feed line. The pyrotechnic igniter that was discussed in section 6.3 was used in four hot fire tests and provided a means of safe and repeatable ignition of the rocket motor.

The hot fire testing aimed to explore the performance gain that can be achieved for a 40% by-mass aluminised fuel gain, if any. The average regression rate of the two pure paraffin wax tests that had a similar burn time was 1.483 mm/s, using LH-001 and LH-007. For the two aluminised tests, LH-006

and LH-008, an average regression rate of 1.584 mm/s was calculated. This results in a 6% enhancement that is lower than the reported 25% in section 1.6.1. One factor that could account for this difference is the type of aluminium powder that was used. The average particle size of the aluminium powder that was used in the study reported in 1.6.1 is unknown (McCormick, et al., 2005).

It should be noted that the oxidiser mass flow rate was higher than required for the aluminised tests in this project. The same injector was used for both sets of tests and, since a 40 % aluminised fuel grain has a lower stoichiometric O/F ratio than pure paraffin wax, the aluminised tests were oxidiser-rich compared to the pure paraffin wax tests. During the combustion process, nitrous oxide decomposes into oxygen and nitrogen. A proposed problem when hot fire testing an oxidiser-rich aluminised fuel grain is the cooling effect produced by the nitrogen and excess oxygen that is present in the port, not allowing the fuel grain's burning layer to reach a suitable temperature required for complete combustion of the aluminium. This could also account for the difference in the observed enhancement in regression rate compared to the enhancement seen in literature where the oxidiser mass flow rate was appropriate to the solid fuel grain.

In terms of the combustion efficiency of the hot fire tests, Figure 8.46 shows that the pure paraffin wax tests achieved a higher combustion efficiency compared to the aluminised tests. This could be accounted for by the ejection of material during the testing that was observed, the oxidiser-rich conditions, and the substantial portion of the aluminium powder that did not combust. This was evident by the molten aluminium seen on the fencing in Figure 8.22, and the solidified accumulation seen in on the nozzle's converging face and on the post-combustion chamber insert.

In terms of the aluminium powder used in this project, it can be concluded that its use does not produce any notable performance enhancement. For the average 6 % enhancement in regression rate that was seen, the practical implications in terms of nozzle damage, slag formation, increased rocket motor mass, and chuffing outweigh the slight enhancement in performance.

9.1. Future recommendations

For future testing of metal additives, it is recommended that a new combustion chamber be commissioned; perhaps one which uses O-ring sealing to allow for faster turnaround times. Such a combustion chamber should also be made from stainless-steel to ensure longevity of the assembly.

In terms of the electronic configuration of the system, it is suggested that the Arduino board that controls the servo motors be removed and replaced with a more robust and reliable system such as a digital output module compatible with the C-DAQ system that is currently used.

For the feed system, a stainless-steel, three-piece, 1/2" instrumentation valve provided by Swagelok should replace the single-piece valve that is currently used on the injection line. A three-piece valve has a lower torque requirement and will therefore allow for faster actuation of the valve and reduced wear and tear on the servo motors.

In terms of the recommendations for the testing of metal additives, aluminium should be studied further as an additive in paraffin wax hybrid rocket motors, according to the following recommendations. Aluminium powder should be tested as an additive in different mass percentages such as 10% and 20% to mitigate any potential effects of the high heat of vaporisation per unit mass of the solid propellant. Second, aluminium powder comprising smaller particles should be tested as a means of accelerating the rate of particle combustion.

Third, chemical stripping of the aluminium oxide layer before addition to the fuel grain should be investigated. For example, this could be accomplished in the following manner: in an inert environment, the aluminium powder can be chemically stripped of its oxide layer via a rinse in a sodium hydroxide solution, before being washed off with de-ionised water and added into a container of liquid wax. Once the container of the wax/aluminium powder slurry is removed from the inert environment, the aluminium particles are isolated from atmospheric oxygen by the wax surrounding the particles.

In a general sense, these recommendations are intended to enable more complete combustion of aluminium particles during their short residence time within the combustion chamber, thereby permitting the efficient combustion of high density propellants and the development of more compact hybrid rocket propulsion systems.

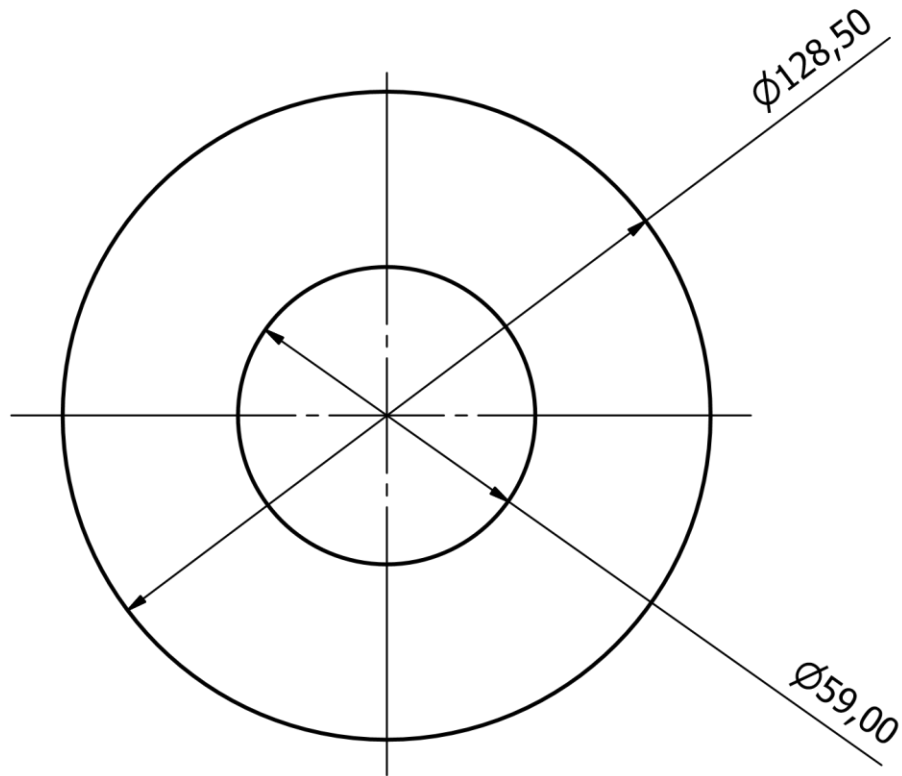
References

- Boronowsky, K. (2011) *Non-Homogenous Hybrid Rocket Fuel for Enhanced Regression Rates Utilizing Partial Entrainment*, MSc thesis. San Jose State University.
- Cantwell, B. J. (2014) ‘*Similarity Solution of Fuel Mass Transfer, Port Mass Flux Coupling in Hybrid Propulsion*’, *Journal of Engineering Mathematics*, 84(1), pp. 19–40.
- Cantwell, B., Karabeyoglu, A. and Altman, D. (2009) ‘*Recent Advances in Hybrid Propulsion*’, *Journal of Energetic Materials and Chemical Propulsion*, 9(4), pp. 305–326.
- Chiaverini, M. J. and Kuo, K. K. (2006) ‘*Metals, Energetic Additives*’, in Lu, F. K. (ed.) *Fundamentals of Hybrid Rocket Combustion and Propulsion*. Reston, Virginia: American Institute of Aeronautics and Astronautics, pp. 417–427.
- Corbridge, D. E. C. (1990) ‘*Phosphorus: An Outline of its Chemistry, Biochemistry, and Technology*’, in. Amsterdam: Elsevier, pp. 115–116.
- Desain, J. D., Curtiss, T. J., Cohen, R. B. and Brady, B. B. (2008) *Testing of LiAlH₄ as a Potential Additive to Paraffin Wax Hybrid Rocket Fuel*, The Aerospace Corporation.
- Farbar, E., Louwers, J. and Kaya, T. (2007) ‘*Investigation of Metallized and Nonmetallized Hydroxyl Terminated Polybutadiene/Hydrogen Peroxide Hybrid Rockets*’, *Journal of Propulsion and Power*, 23(2), pp. 476–486. Available at: <http://arc.aiaa.org/doi/10.2514/1.22091>.
- Fisher Controls International (2001) *Control Valve Handbook*. Third Edit. Marshalltown, Iowa, United State of America: Fisher Controls International Inc. Available at: http://www.chemicalprocessing.com/assets/Media/MediaManager/control_valves.pdf.
- Government of the Republic of South Africa (2003) *Explosives Act, No. 15 of 2003*. South Africa: Juta Law.
- Karabeyoglu, A. M. and Arkun, U. (2014) ‘*Evaluation of Fuel Additives for Hybrid Rockets and SFRJ Systems*’, in 50th AIAA/ASME/SAE/ASEE Joint Propulsion Conference and Exhibit. Cleveland, Ohio, United States of America: American Institute of Aeronautics and Astronautics, pp. 1–41. Available at: <http://arc.aiaa.org/doi/10.2514/6.2014-3647>.
- Karabeyoglu, A., Zilwa, S. De, Cantwell, B. and Zilliac, G. (2005) ‘*Modeling of Hybrid Rocket Low Frequency Instabilities*’, *Journal of Propulsion and Power*. American Institute of Aeronautics and Astronautics, 21(6), pp. 1107–1116. Available at: <http://arc.aiaa.org/doi/10.2514/1.7792>.

- Karabeyoglu, M., Cantwell, B. and Altman, D. (2001) '*Development and Testing of Paraffin-Based Hybrid Rocket Fuels*', in 37th AIAA/ASME/SAE/ASEE Joint Propulsion Conference & Exhibit. Salt Lake City, Utah, United States of America: American Institute of Aeronautics and Astronautics. Available at: <http://arc.aiaa.org/doi/10.2514/6.2001-4503>.
- Larson, D. B. et al. (2015) '*Formulation, Casting, and Evaluation of Paraffin-Based Solid Fuels Containing Energetic and Novel Additives for Hybrid Rockets*', International Journal of Energetic Materials and Chemical Propulsion, 14(6), pp. 453–478.
- Lohner, K., Dyer, J., Doran, E., Dunn, Z. and Zilliac, G. (2006) '*Fuel Regression Rate Characterization Using a Laboratory Scale Nitrous Oxide Hybrid Propulsion System*', in 42nd AIAA/ASME/SAE/ASEE Joint Propulsion Conference and Exhibit. Sacramento, California, United States of America: American Institute of Aeronautics and Astronautics. Available at: <http://arc.aiaa.org/doi/abs/10.2514/6.2006-4671> (Accessed: 25 June 2018).
- Maharaj, C. S. and Chetty, C. (2014) *Metallized Hybrid Rocket Propulsion System*. Durban, KwaZulu-Natal.
- Marxman, G. and Gilbert, M. (1963) '*Turbulent Boundary Layer Combustion in the Hybrid Rocket*', in Symposium (International) on Combustion, pp. 371–383. Available at: <https://www.sciencedirect.com/science/article/pii/S0082078463800466>.
- McCormick, A., Hultgren, E., Lichtman, M., Smith, J., Sneed, R. and Azimi, S. (2005) '*Design, Optimization, and Launch of a 3" Diameter N₂O/Aluminized Paraffin Rocket*', in 41st AIAA/ASME/SAE/ASEE Joint Propulsion Conference and Exhibit. Tucson, Arizona, United States of America: American Institute of Aeronautics and Astronautics. Available at: <http://arc.aiaa.org/doi/abs/10.2514/6.2005-4095> (Accessed: 11 February 2015).
- Nakagawa, I. and Nikone, S. (2011) '*Study on the Regression Rate of Paraffin-Based Hybrid Rocket Fuels*', in 45th AIAA/ASME/SAE/ASEE Joint Propulsion Conference and Exhibit. Denver, Colorado, United States of America: American Institute of Aeronautics and Astronautics, pp. 1276–1279. Available at: <http://arc.aiaa.org/doi/10.2514/1.B34206>.
- Nayyar, M., King, R. and Crocker, S. (2000) *Piping handbook. 7th edn*, Slurry and Sludge Piping. 7th edn. New York: McGraw-Hill. Available at: http://tuboserw.agilityhoster.com/pages/pdf/Piping_Handbook.pdf.
- numeric-GmbH (2015) *Discharge Coefficients in Aircraft Decompression Simulations*. Available at: <http://www.numeric-gmbh.ch/posts/discharge-coefficients-in-aircraft-decompression-simulations.html> (Accessed: 13 December 2017).

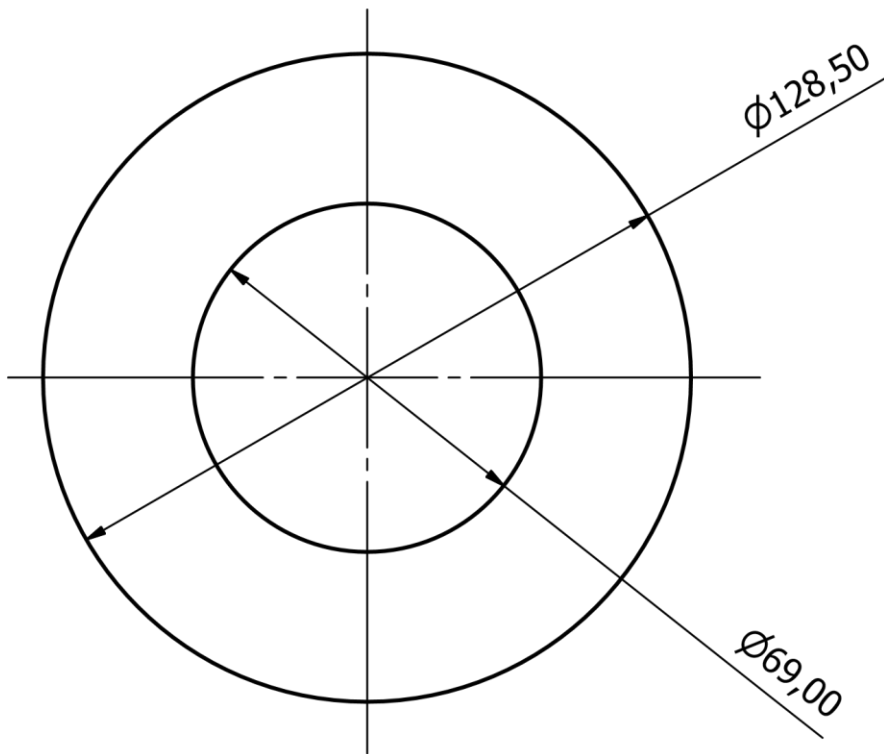
- Rai, A., Park, K., Zhou, L. and Zachariah, M. R. (2006) '*Understanding the Mechanism of Aluminium Nanoparticle Oxidation*', *Combustion Theory and Modelling*. Taylor and Francis Group, 10(5), pp. 843–859.
- Sasol GmbH (2013) *Microcrystalline Wax*. Hamburg, Germany.
- Shafirovich, E. and Varma, A. (2008) '*Metal-CO₂ Propulsion for Mars Missions: Current Status and Opportunities*', *Journal of Propulsion and Power*, 24(3), pp. 385–394. Available at: <http://arc.aiaa.org/doi/10.2514/1.32635> (Accessed: 25 June 2018).
- Space Propulsion Group (no date) *Advanced Hybrid Rocket Fuels*. Available at: <http://www.spg-corp.com/advanced-hybrid-rocket-fuels.html> (Accessed: 10 February 2015).
- Sutton, G. and Biblarz, O. (2001a) '*Combustion Instability*', in *Rocket Propulsion Elements*. 7th edn. John Wiley & Sons, Inc., p. 603.
- Sutton, G. and Biblarz, O. (2001b) '*Multiphase Flow*', in *Rocket Propulsion Elements*. 7th edn. John Wiley & Sons, Inc., pp. 88–89.
- Theba, R., Ramruthan, N. and Dlamini, M. (2014) *Hybrid Slab Motor Visualisation Test Stand*. Durban, KwaZulu-Natal.
- Waxman, B. S., Zimmerman, J. E. and Cantwell, B. J. (2013) '*Mass Flow Rate and Isolation Characteristics of Injectors for Use with Self-Pressurizing Oxidizers in Hybrid Rockets*', in 49th AIAA/ASME/SAE/ASEE Joint Propulsion Conference and Exhibit. San Jose, California, United States of America: American Institute of Aeronautics and Astronautics, pp. 1–32.
- De Zilwa, S., Karabeyoglu, A., Zilliac, G., King, L. and Reinath, M. (2003) '*Combustion Oscillations in High-Regression-Rate Hybrid Rockets*', in 39th AIAA/ASME/SAE/ASEE Joint Propulsion Conference and Exhibit. Huntsville, Alabama, United States of America: American Institute of Aeronautics and Astronautics. Available at: <http://arc.aiaa.org/doi/10.2514/6.2003-4465> (Accessed: 25 June 2018).

Appendix A: Manufacturing drawings



UNLESS OTHERWISE
STATED GENERAL
TOLERANCES: \pm mm
ANGLES: \pm °

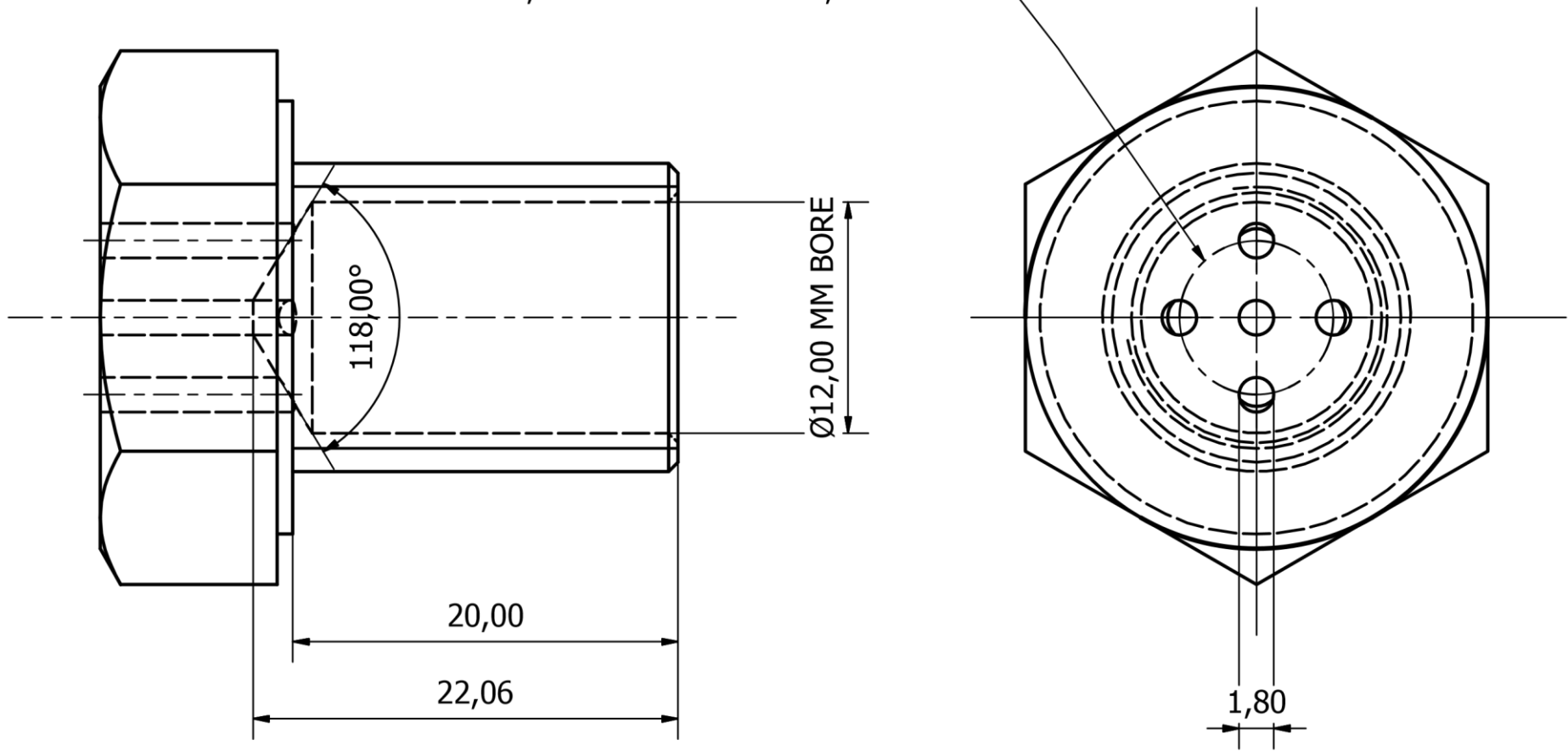
UNIVERSITY OF KWAZULU-NATAL SCHOOL OF ENGINEERING MECHANICAL ENGINEERING	MAT.: TG	No. REQ.: 5	SCALE:	UNITS: mm	PROJECT: HYBRID ROCKET	No.:
	DATE	CHECKED	STUDENT NAME: CHIKHAR MAHARAJ			
	PROJECT SUPERVISOR		STUDENT No.: 210501203		TITLE: AFT GASKET	
	WORKSHOP TECHNICIAN		E-MAIL: chikhar@live.com			
TECHNICAL OFFICER			TEL. No.: 0829750330			



UNLESS OTHERWISE
STATED GENERAL
TOLERANCES: \pm mm
ANGLES: \pm °

UNIVERSITY OF KWAZULU-NATAL SCHOOL OF ENGINEERING MECHANICAL ENGINEERING	MAT.: TG	No. REQ.: 5	SCALE:	UNITS: mm	PROJECT: HYBRID ROCKET	No.:
	DATE	CHECKED	STUDENT NAME: CHIKHAR MAHARAJ			
	PROJECT SUPERVISOR		STUDENT No.: 210501203		TITLE: FORE GASKET	
	WORKSHOP TECHNICIAN		E-MAIL: chikhar@live.com			
TECHNICAL OFFICER			TEL. No.: 0829750330			

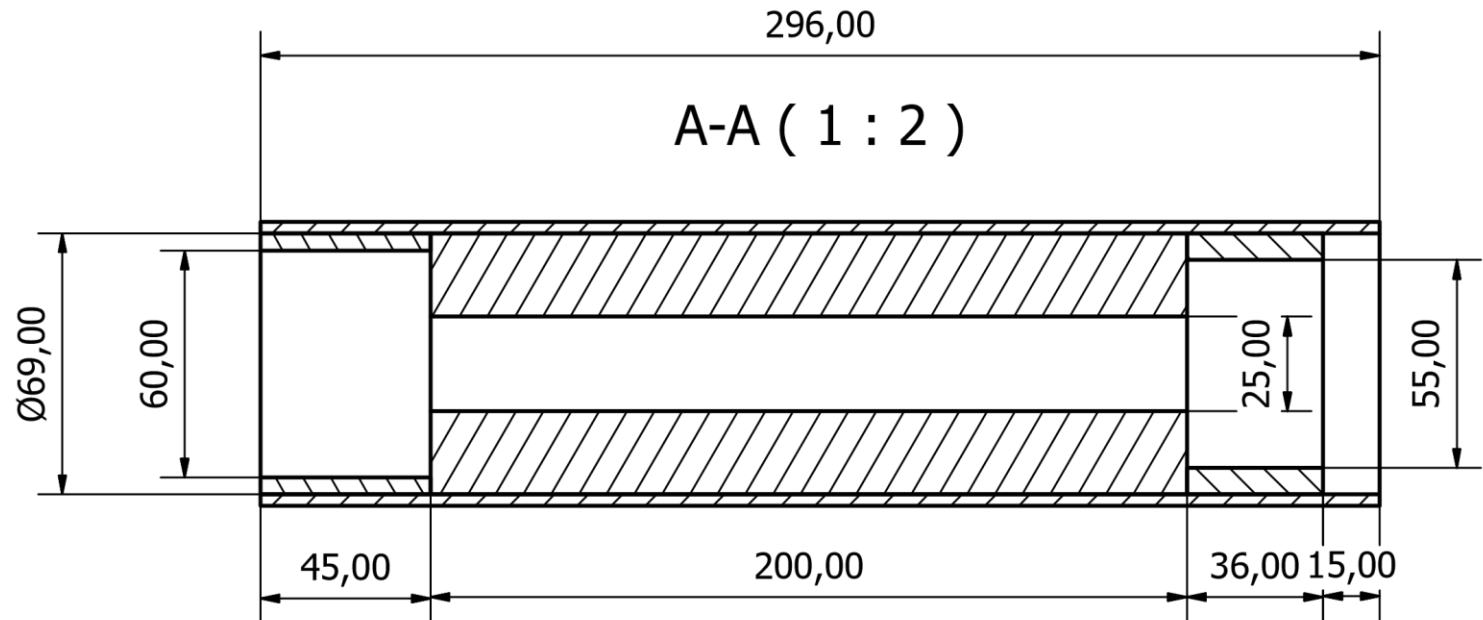
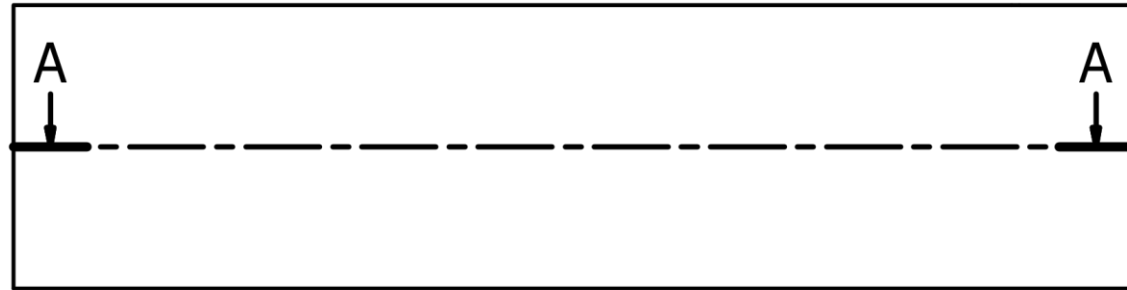
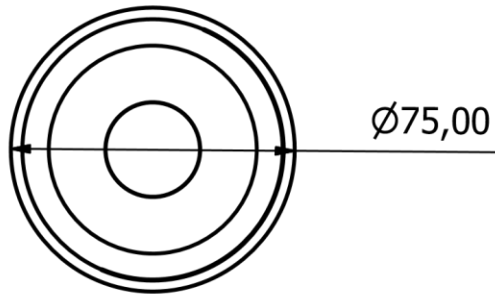
ALL HOLES 1.8 MM, ALL THROUGH ON 8,00 MM PCD



1,8 MM HOLES CANNOT HAVE A DEPTH OF LESS THAN 7,2MM - VENA CONTRACTA RECOVERY

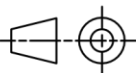
UNLESS OTHERWISE STATED GENERAL TOLERANCES: ± 0.1 mm ANGLES: \pm °

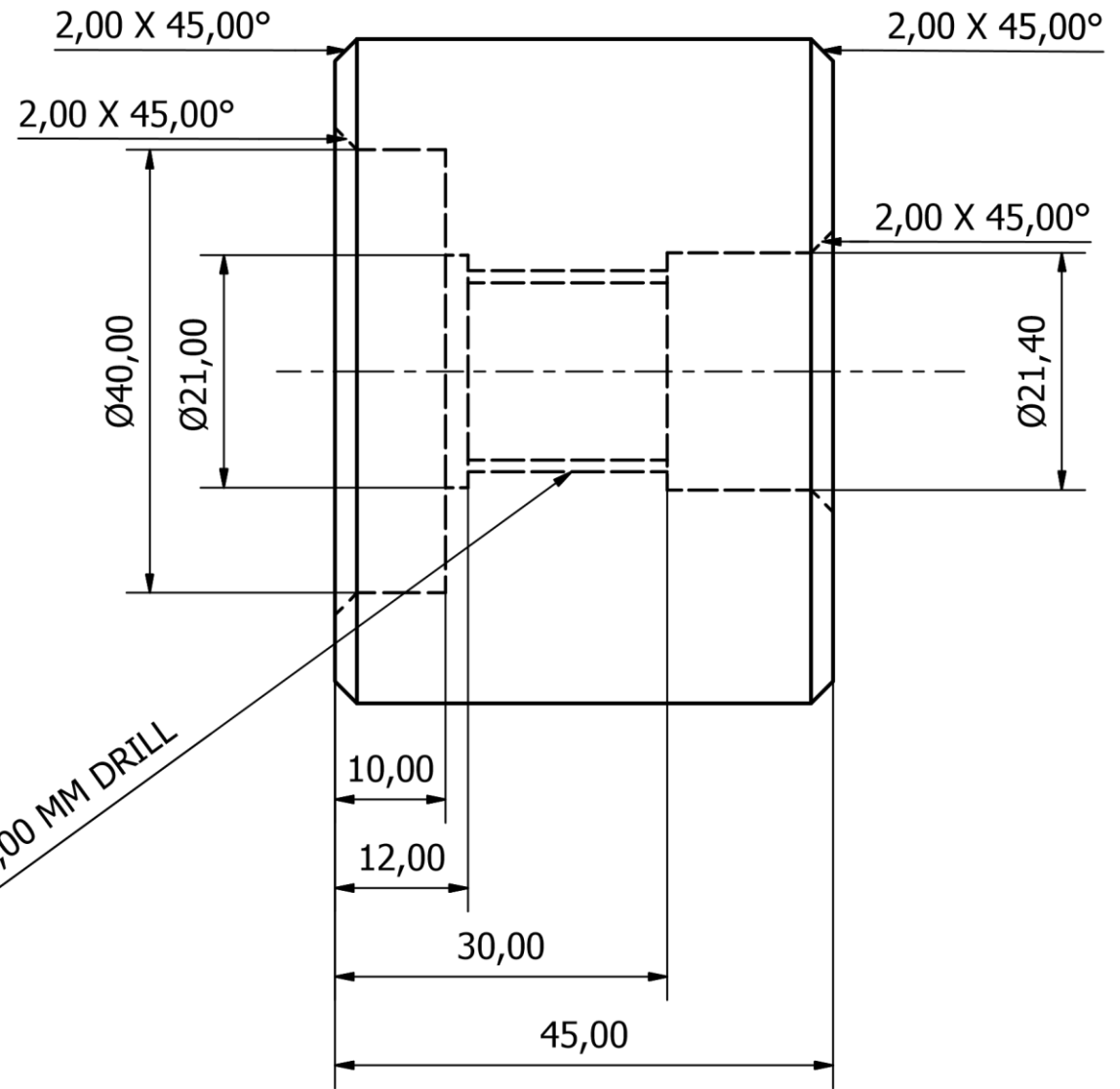
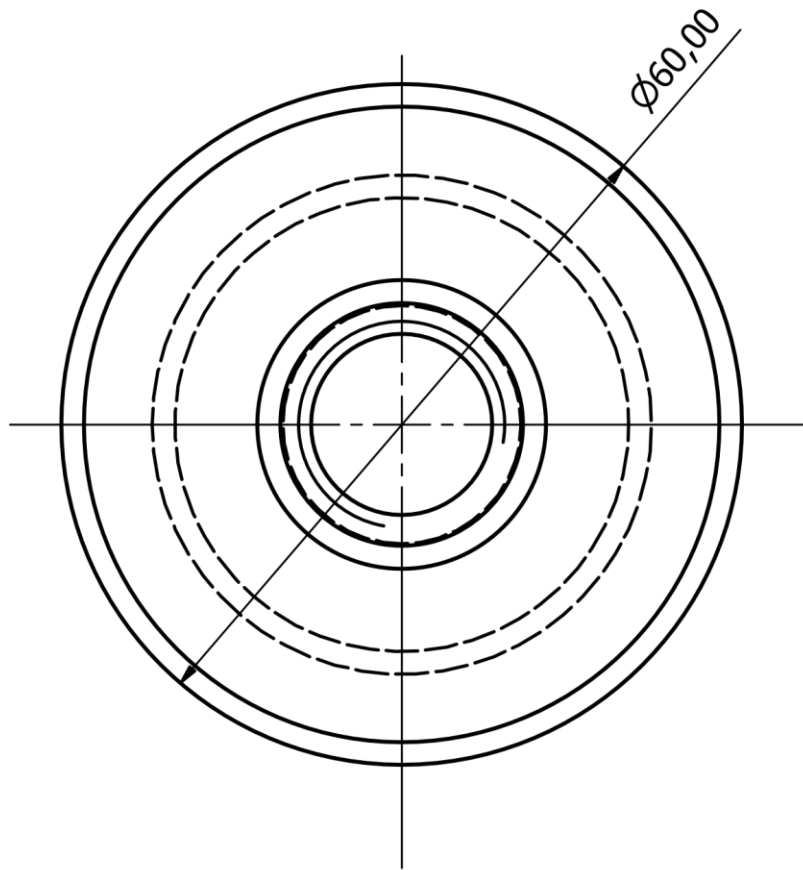
UNIVERSITY OF KWAZULU-NATAL SCHOOL OF ENGINEERING MECHANICAL ENGINEERING	MAT.: BRASS	No. REQ.: 1	SCALE: 3:1	UNITS: mm	PROJECT: HYBRID ROCKET	No.: AI01
	DATE	CHECKED	STUDENT NAME: CHIKHAR MAHARAJ		TITLE: AXIAL INJECTOR	
	PROJECT SUPERVISOR		STUDENT No.: 210501203			
	WORKSHOP TECHNICIAN		E-MAIL: chikhar@live.com			
TECHNICAL OFFICER			TEL. No.: 0829750330			



UNLESS OTHERWISE
STATED GENERAL
TOLERANCES: ± 0.1 mm
ANGLES: \pm °

UNIVERSITY OF KWAZULU-NATAL SCHOOL OF ENGINEERING MECHANICAL ENGINEERING	MAT.: VARIOUS	No. REQ.: 1	SCALE: 1:2	UNITS: mm	PROJECT: HYBRID ROCKET	No.: NUL
	DATE	CHECKED	STUDENT NAME: CHIKHAR MAHARAJ			
	PROJECT SUPERVISOR		STUDENT No.: 210501203		TITLE: NUL	
	WORKSHOP TECHNICIAN		E-MAIL: chikhar@live.com			
TECHNICAL OFFICER			TEL. No.: 0829750330			

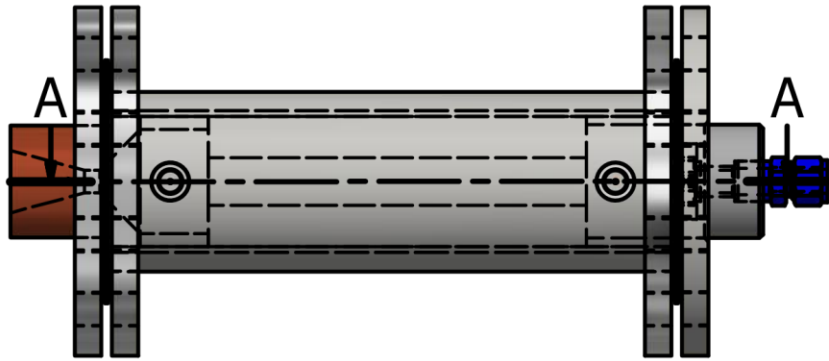




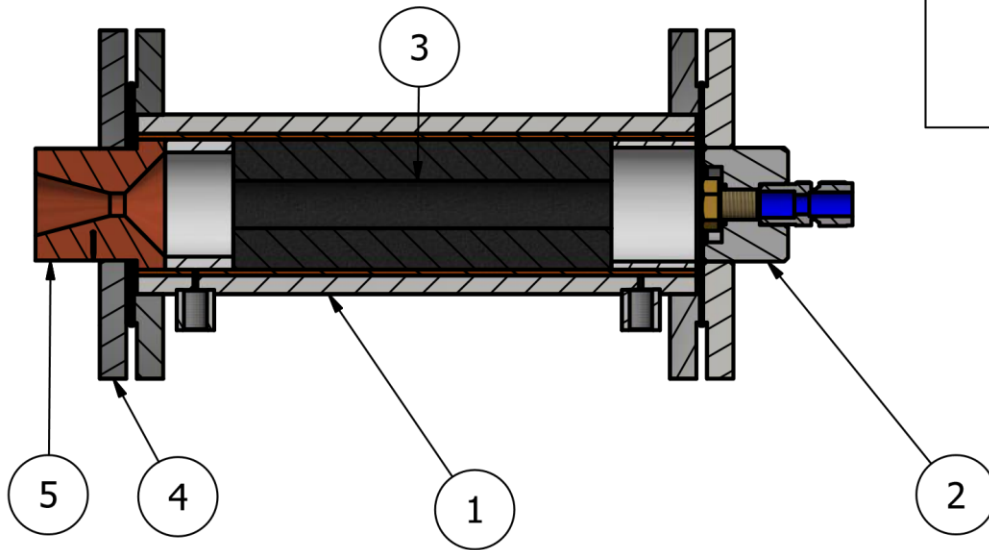
M16x2 - 6H 14,00 MM DRILL

UNLESS OTHERWISE
STATED GENERAL
TOLERANCES: ± mm
ANGLES: ± °

UNIVERSITY OF KWAZULU-NATAL SCHOOL OF ENGINEERING MECHANICAL ENGINEERING	MAT.: 316 SS	No. REQ.: 1	SCALE: 1.5:1	UNITS: mm	PROJECT: HYBRID ROCKET	No.: IMN01
	DATE	CHECKED	STUDENT NAME: CHIKHAR MAHARAJ		TITLE: INJECTOR MANIFOLD	
	PROJECT SUPERVISOR		STUDENT No.: 210501203			
	WORKSHOP TECHNICIAN		E-MAIL: chikhar@live.com			
TECHNICAL OFFICER			TEL. No.: 0829750330			



A-A (1 : 4)

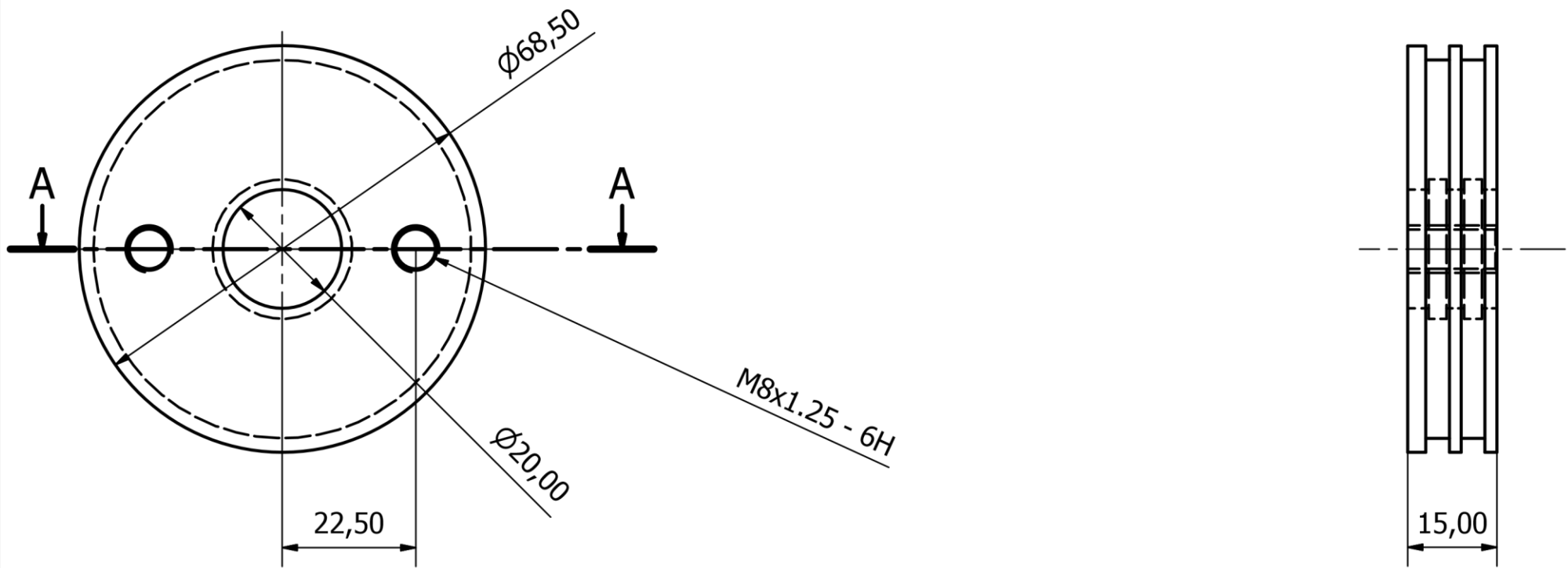


PARTS LIST		
ITEM	DESCRIPTION	MATERIAL
1	Combustion chamber assembly	Steel, Mild
2	Injector flange assembly	Steel, Mild, 316 SS
3	Fuel grain cartridge assembly	Paraffin wax, HDPE, phenolic
4	Nozzle Flange	Steel, Mild
5	Nozzle	Copper 6000 alloy

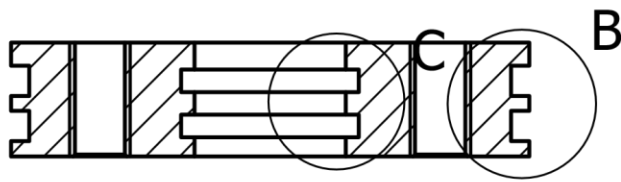
UNLESS OTHERWISE STATED GENERAL TOLERANCES: ± 0.1 mm ANGLES: \pm °

UNIVERSITY OF KWAZULU-NATAL SCHOOL OF ENGINEERING MECHANICAL ENGINEERING	MAT.:	No. REQ.: 1	SCALE: 1:4	UNITS: mm	PROJECT: HYBRID ROCKET	No.: MA1
		DATE	CHECKED	STUDENT NAME: CHIKHAR MAHARAJ		
	PROJECT SUPERVISOR			STUDENT No.: 210501203	TITLE: MOTOR ASSEMBLY	
	WORKSHOP TECHNICIAN			E-MAIL: chikhar@live.com		
	TECHNICAL OFFICER			TEL. No.: 0829750330		

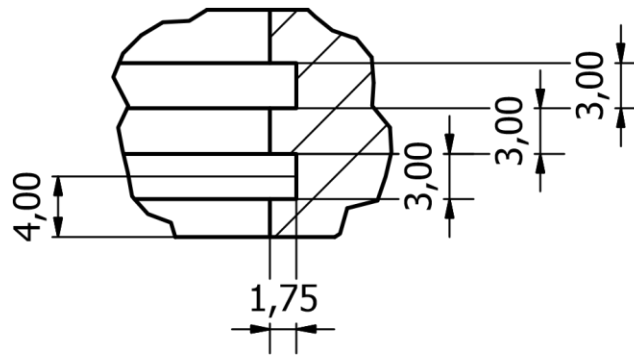




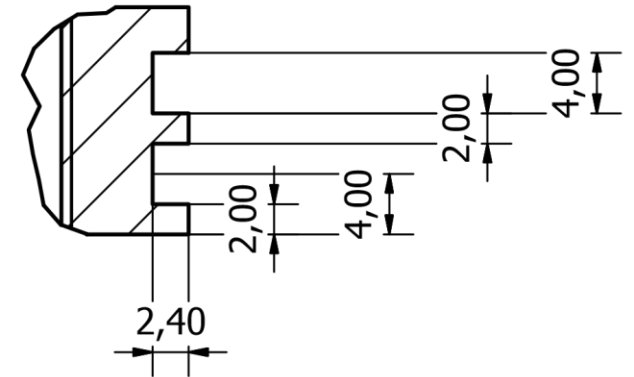
A-A (1 : 1)



C (2 : 1)



B (2 : 1)

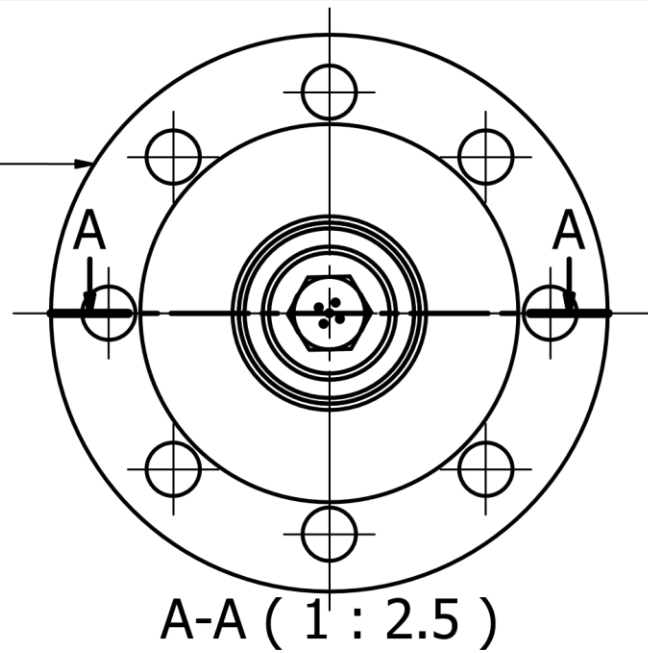


UNLESS OTHERWISE
STATED GENERAL
TOLERANCES: ± mm
ANGLES: ± °

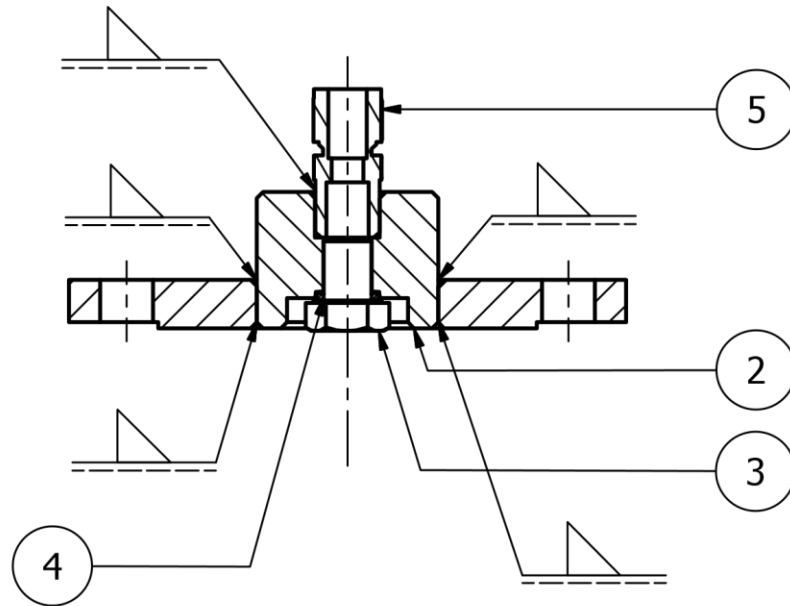
UNIVERSITY OF KWAZULU-NATAL SCHOOL OF ENGINEERING MECHANICAL ENGINEERING	MAT.: ALUMINIUM	No. REQ.: 1	SCALE: 1:1	UNITS: mm	PROJECT: HYBRID ROCKET	No.: MP1
	DATE	CHECKED	STUDENT NAME: CHIKHAR MAHARAJ			
	PROJECT SUPERVISOR		/STUDENT No.: 210501203		TITLE: MOULD PISTON	
	WORKSHOP TECHNICIAN		E-MAIL: chikhar@live.com			
TECHNICAL OFFICER			TEL. No.: 0829750330			

1

MILD STEEL MATERIAL TO BE REMOVED FROM INJECTOR FLANGE BEFORE COMMENCEMENT WITH MODIFICATION



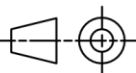
A-A (1 : 2.5)

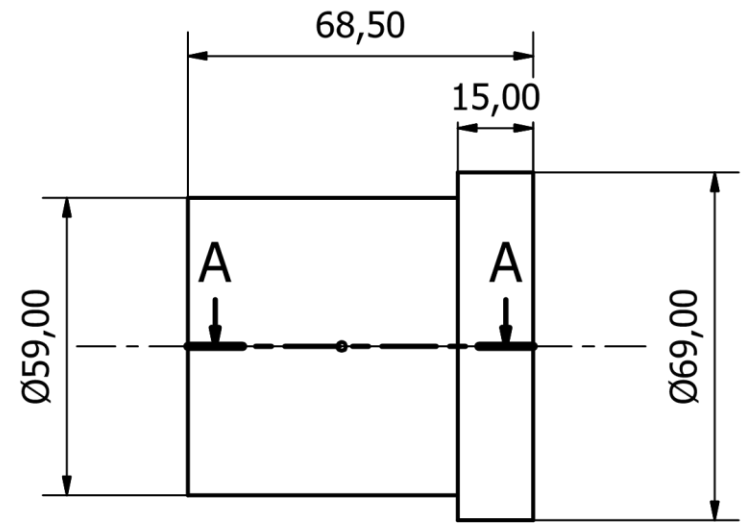
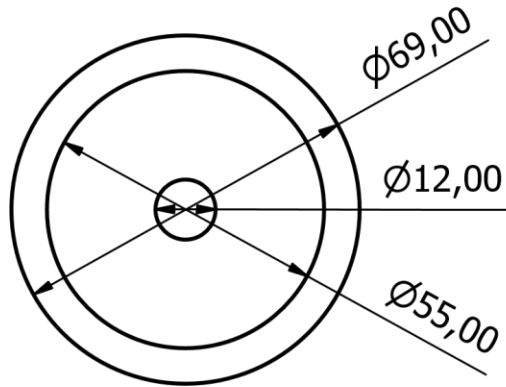


PARTS LIST			
ITEM	QTY	PART NUMBER	DESCRIPTION
1	1	Injector Flange	
2	1	Injector Manifold	316SS 60 dia
3	1	Showerhead Injector	Hexagon head screws
4	1	Injector O ring	Nitrile Rubber 15.54 mm ID, 2.62CS
5	1	Swagelok 1/2" fitting	ACIS data in IGES format

UNLESS OTHERWISE STATED GENERAL TOLERANCES: ± 0.1 mm ANGLES: \pm °

UNIVERSITY OF KWAZULU-NATAL SCHOOL OF ENGINEERING MECHANICAL ENGINEERING	MAT.: SEE PARTS LIST	No. REQ.: 1	SCALE: 1:2.5	UNITS: mm	PROJECT: HYBRID ROCKET	No.: IA01
		DATE	CHECKED	STUDENT NAME: CHIKHAR MAHARAJ		
	PROJECT SUPERVISOR			STUDENT No.: 210501203	TITLE: INJECTOR ASSEMBLY	
	WORKSHOP TECHNICIAN			E-MAIL: chikhar@live.com		
	TECHNICAL OFFICER			TEL. No.: 0829750330		

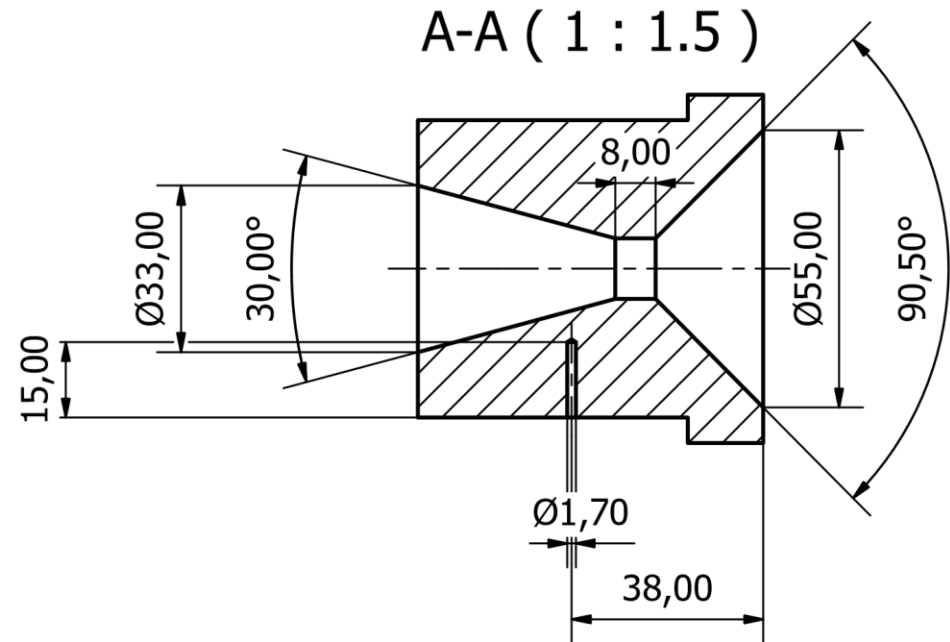




SUPERSONIC AREA RATIO (A_e/A_t) = 7.56
 SUBSONIC CONTRACTION RATIO (A_c/A_t) = 21

DESIGN REFERENCE: NASA CEA
 BASIC CONICAL DESIGN

THIS DESIGN SHALL NOT BE USED FOR GRAPHITE



UNLESS OTHERWISE
 STATED GENERAL
 TOLERANCES: ± 0.05 mm
 ANGLES: \pm °

UNIVERSITY OF KWAZULU-NATAL SCHOOL OF ENGINEERING MECHANICAL ENGINEERING	MAT.: COPPER	No. REQ.: 1	SCALE: 1:1.5	UNITS: mm	PROJECT: HYBRID ROCKET	No.: CN001
	DATE	CHECKED	STUDENT NAME: CHIKHAR MAHARAJ		TITLE: ROCKET NOZZLE	
	PROJECT SUPERVISOR		STUDENT No.: 210501203			
	WORKSHOP TECHNICIAN		E-MAIL: chikhar@live.com			
TECHNICAL OFFICER			TEL. No.: 0829750330			

Appendix B: NASA CEA input script

problem o/f=1,2,3,4,5,6,7,8,

rocket equilibrium

p,bar=40,

react

oxid=N2O wt=100 t,k=298

fuel=Wax wt=100 t,k=298

h,kj/mol=-1438.2 C 50 H 102

output short

plot isp

end

Appendix C: Termination system C code

```
// All comments are in this colour

#include <Servo.h> //include library for servo handling

Servo inject; // name servo

Servo dump; // name servo

int button = 8; //define pin for physical termination button

int button_pos = 0; // initialise button state

int dump_relay = 11; // define relay pin

int inject_relay = 12; // define relay pin

int SwagelokOpen = 6; // define relay pin

int SwagelokClose = 7; // define relay pin

void setup() {

    inject.attach(9); // connect "inject" servo to PWM pin 9

    dump.attach(10); // connect "dump" servo to PWM pin 10

    pinMode(button, INPUT); // define termination button as an input

    // define all relays as outputs

    pinMode(dump_relay, OUTPUT);

    pinMode(inject_relay, OUTPUT);

    pinMode(SwagelokOpen, OUTPUT);

    pinMode(SwagelokClose, OUTPUT);

    Serial.begin(9600); // initialise serial communication for troubleshooting

}
```

```

void loop() {

  // read and report on button position

  button_pos = digitalRead(button);

  Serial.println(button_pos);

  // main algorithm – poll termination button and take action if pressed

  if (button_pos == LOW){

    inject.writeMicroseconds(800);

    dump.writeMicroseconds(1400);

    digitalWrite(dump_relay, HIGH);

    digitalWrite(inject_relay, HIGH);

    digitalWrite(SwagelokOpen, LOW);

    digitalWrite(SwagelokClose, LOW);

  }

  else if (button_pos == HIGH) {

    digitalWrite(dump_relay, LOW);

    digitalWrite(inject_relay, LOW);

    digitalWrite(SwagelokOpen, HIGH);

    digitalWrite(SwagelokClose, HIGH);

  }

  delay(50); // define delay for controller stability

}

```

Appendix D: Hot fire testing videos

Designator	Date	Additive	Burn Time
LH-001	2016-06-13	Pure	7,01
LH-003	2016-10-21	Pure	13,7
LH-005	2017-05-29	40% Al	7,94
LH-006	2017-06-15	40% Al	6,79
LH-007	2017-07-11	Pure	6,43
LH-008	2017-07-12	40% Al	6,71

SEE ATTACHED DIGITAL MEDIA FOR FOOTAGE AND TEST DATA IN TDMS FORMAT

PASTE DIGITAL MEDIA HERE